DISS. ETH NO. 26451

A 50 kW SOLAR THERMOCHEMICAL REACTOR FOR SYNGAS PRODUCTION UTILIZING POROUS CERIA STRUCTURES

A thesis submitted to attain the degree of

DOCTOR OF SCIENCES of ETH ZURICH
(Dr. sc. ETH Zurich)

presented by

STEFAN BEAT ZOLLER
MSc ETH ME
born on 27.10.1990
citizen of Au (SG)

accepted on the recommendation of

Prof. Dr. Aldo Steinfeld, examiner
Prof. Dr. Martin Kaltschmitt, co-examiner

2020

Abstract

This thesis reports on the development, optimization and experimental testing of a solar receiver-reactor for the thermochemical splitting of H_2O and CO_2 to produce H_2 and CO (syngas). The solar reactor allows to apply a temperature and pressure swing redox cycle to pure ceria in the form of a reticulated porous ceramic (RPC). In the first, endothermic step, the ceria RPC is directly heated with concentrated solar radiation to around 1500 °C while under vacuum pressure of less than 100 mbar, thereby releasing oxygen from its crystal lattice. In the subsequent, exothermic step, the reactor is repressurized with H_2O and/or CO_2 as it cools, and at temperatures typically below 1000 °C, the partially reduced ceria is re-oxidized with a flow of H_2O and/or CO_2 at atmospheric pressure. The produced syngas can be catalytically processed to conventional liquid hydrocarbon fuels.

A reactor prototype at the 4 kW scale has been previously designed and tested using a high-flux solar simulator. In this work, the same reactor technology is realized and optimized at the 50 kW scale and tested under realistic conditions using a solar concentrating facility located in Móstoles, Spain.

Initial experiments focused on comparing the cycling performance and the mechanical stability of three different ceria cavities made of an interlocking structure of RPC bricks with different porosities, thicknesses and geometries. The performance of the solar reactor for CO_2 splitting was experimentally assessed in a high-flux solar simulator. The mechanical strength and stability of the RPCs was assessed with three-point bend testing after fabrication and visually after testing in the solar reactor. The results indicate that lower porosity and higher thickness, both resulting in a higher ceria mass loading, are generally beneficial for the mechanical integrity of the RPC cavity, but the addition of mass without ensuring effective volumetric absorption of the solar radiation and

uniform heating of the ceria does not increase the reactor performance. The maximum power of the solar simulator was limited to 32.2 kW delivered at the 16 cm diameter aperture of the solar reactor, which corresponds to a solar concentration ratio of 1602 suns. As a result of the limited power input, a relatively low maximum solar-to-fuel conversion efficiency, defined as the ratio of the heating value of the fuel produced to the input of solar radiative energy and the energy penalties associated with inert gas separation and vacuum pumping, of 3.48±0.08% was measured. Stable operation over multiple cycles without observable degradation was shown with an extended experiment of five consecutive CO_2 splitting cycles.

To further analyse the performance of the solar reactor and to gain insight into improved design and operation conditions, a transient heat transfer model of the solar reactor was developed. The numerical model couples the incoming concentrated solar radiation using Monte Carlo ray tracing, incorporates the reduction chemistry by assuming thermodynamic equilibrium, and accounts for internal radiation heat transfer inside the porous ceria by applying effective heat transfer properties. The model was experimentally validated using the data acquired in the high-flux solar simulator. The numerical results highlight the potential of the solar reactor to reach high solar-to-fuel energy conversion efficiencies when operated at high power levels. At a solar radiative power input of 50 kW, an efficiency exceeding 6% is predicted. If the RPC macroporosity could be substantially increased to achieve better volumetric absorption of radiation and uniform heating of the ceria, the model predicts efficiencies exceeding 10%.

Based on the experimental results acquired in the high-flux solar simulator and the numerical results of the heat transfer model, a new ceria RPC cavity was designed for the operation of the solar reactor with the solar concentrating facility located in Móstoles, Spain. The facility consists of 169 heliostats which concentrate sunlight onto a tower with an optical height of 15 m. The solar reactor, situated on top of the tower, is facing downwards onto the heliostats and features a self-supporting design of the ceria RPC cavity that is adapted for the inclination angle of 40 degrees. With this adjusted solar reactor, a maximum

solar-to-fuel energy conversion efficiency of 5.6±1.0% is experimentally demonstrated for CO_2 splitting at a solar radiative power input of 55.8±8.2 kW. Simulating the same experiment using the transient heat transfer model reveals how the performance of the reactor could be further improved. At a power input of 55.8 kW, 21.0% of the total solar energy input is lost by reradiation from the hot cavity, but by far the biggest share of energy is used for sensible heating of the ceria and the bulk reactor components, accounting for 58.4% of the solar energy input in total. This energy is mostly lost when the reactor cools down to the oxidation temperature, which highlights the need for implementing heat recovery in order to increase the efficiency of such reactor technology in the future.

For the co-splitting of H_2O and CO_2 in the solar reactor, different measures to adjust the composition of the produced syngas are discussed. At optimal operating conditions, 62 consecutive redox cycles are performed with the same ceria RPC cavity. The produced syngas is collected and stored in a pressurized gas cylinder. Within the European research consortium SUN-to-LIQUID, the accumulated syngas is further processed via Fischer-Tropsch synthesis to produce liquid hydrocarbon fuels on-site.

This work demonstrates the technical feasibility of solar thermochemical H_2O and CO_2 splitting via ceria redox cycling under real-world conditions and at a relevant scale and as such contributes towards the development of a commercial application for the production of solar hydrocarbon fuels.

Zusammenfassung

Die vorliegende Arbeit berichtet von der Entwicklung, der Optimierung und der experimentellen Untersuchung eines Solarreaktors für die thermochemische Spaltung von H_2O und CO_2 zur Produktion von H_2 und CO (Synthesegas). Der Solarreaktor ermöglicht die Anwendung eines Kreislaufs mit Temperatur- und Druckunterschied auf reines Cerdioxid in der Form einer schaumartigen porösen Keramik (RPC). Im ersten, endothermen Prozessschritt wird das Cerdioxid direkt mit konzentrierter Sonnenenergie bestrahlt und auf etwa 1500 °C erhitzt. Das Cerdioxid ist dabei unter Vakuum bei einem Druck von weniger als 100 mbar und gibt einen Teil des Sauerstoffs aus seinem Kristallgitter frei. Im darauffolgenden exothermen Schritt wird der Reaktor zuerst mit H_2O und/oder CO_2 gefüllt. Bei Temperaturen von üblicherweise weniger als 1000 °C wird das partiell reduzierte Cerdioxid mit durchströmendem H_2O und/oder CO_2 unter Atmosphärendruck wieder oxidiert. Das produzierte Synthesegas kann dann mittels katalytischer Verfahren zu konventionellen flüssigen Kohlenwasserstoff-Treibstoffen weiterverarbeitet werden.

Ein 4 kW Reaktorprototyp wurde im Vorfeld dieser Arbeit entwickelt und mithilfe eines Hochfluss-Sonnensimulators getestet. In dieser Arbeit wird dieselbe Reaktortechnologie für eine Betriebsgrösse von 50 kW umgesetzt und optimiert sowie unter realistischen Betriebsbedingungen mithilfe einer Anlage zur Konzentration von Sonnenlicht in Móstoles, Spanien, getestet.

In ersten Experimenten wurde die Leistungsfähigkeit und die mechanische Stabilität von drei verschiedenen Kavitäten aus Cerdioxid verglichen. Die Kavitäten bestehen aus einer sich verzahnenden Struktur von RPC Teilstücken mit unterschiedlicher Porosität, Dicke und Geometrie. Die Leistungsfähigkeit des Solarreaktors zur Spaltung von CO_2 wurde mithilfe eines Hochfluss-Sonnensimulators experimentell analysiert. Die mechanische Belastbarkeit und

die Stabilität der RPCs wurde nach der Herstellung mithilfe von 3-Punkt-Biegeversuchen und nach der Erprobung im Solarreaktor optisch untersucht. Die Resultate deuten darauf hin, dass eine kleinere Porosität und eine grössere Dicke, was beides zu einer höheren Masse an Cerdioxid im Reaktor führt, grundsätzlich vorteilhaft ist für das mechanische Widerstandsvermögen der Kavität aus RPCs. Jedoch führt eine Erhöhung der Masse ohne die gleichzeitige Sicherstellung von effektiver volumetrischer Absorption der Solarstrahlung und damit zusammenhängendes gleichmässiges Aufheizen des Cerdioxids nicht zu einer Erhöhung der Leistungsfähigkeit des Reaktors. Die maximale Leistung des Solarsimulators war limitiert auf 32.2 kW, integriert über die Apertur des Solarreaktors mit einem Durchmesser von 16 cm. Dies entspricht einer durchschnittlichen thermischen Strahlungsdichte von 1602 $kW\,m^{-2}$ (1602 Sonnen). Als Resultat der limitierten Leistung wurde ein relativ tiefer maximaler energetischer Umwandlungswirkungsgrad von Sonnenenergie zu chemischer Energie von 3.48±0.08% gemessen. Der Wirkungsgrad ist definiert als das Verhältnis vom höheren Brennwert des produzierten Brennstoffs zur benötigten Solarenergie sowie zusätzliche Energieeinträge zur Separierung des Inertgases und zum Betrieb der Vakuumpumpen. Ein stabiler Betrieb über mehrere Zyklen ohne sichtbare Degradierung wird ebenfalls gezeigt mit einem erweiterten Experiment über fünf aufeinanderfolgende Zyklen zur Spaltung von CO_2.

Um die Leistungsfähigkeit des Solarreaktors weiter zu analysieren und um Einblick zu gewinnen in verbesserte Designs und Betriebsbedingungen wurde ein transientes Wärmetransportmodell des Solarreaktors entwickelt. Das numerische Modell koppelt die eingehende, konzentrierte Solarstrahlung mittels Monte Carlo Lichtstrahlverfolgung, berücksichtigt die Reduktionsreaktion unter Annahme des thermodynamischen Gleichgewichts und beinhaltet die interne Wärmeübertragung durch Strahlung mittels Verwendung von effektiven Wärmeübertragungseigenschaften. Das Model wurde experimentell validiert mithilfe der Daten die im Hochfluss-Sonnensimulator gesammelt wurden. Die numerischen Resultate unterlegen das Potential des Solarreaktors zur Erreichung von hohen Wirkungsgraden wenn der Reaktor mit hoher thermischer Leistung betrieben wird. Für eine solare Eingangsleistung von 50 kW wird ein

Wirkungsgrad grösser als 6% vorausgesagt. Falls die Makroporosität der RPC Struktur erheblich erhöht werden könnte um eine volumetrische Absorption der eingehenden Strahlung und ein gleichmässigeres Aufheizen des Cerdioxids zu erreichen, so könnten gemäss Modell Wirkungsgrade erreicht werden die 10% übersteigen.

Basierend auf den experimentellen Resultaten die im Hochfluss-Solarsimulator erlangt wurden und den numerischen Resultaten des Wärmetransportmodells wurde eine neue Kavität aus Cerdioxid RPCs entwickelt. Diese Kavität ist optimiert für den Betrieb des Solarreaktors mit der Anlage zur Konzentration von Sonnenlicht in Móstoles, Spanien. Diese Anlage besteht aus 169 Heliostaten, welche das Sonnenlicht auf einen Turm mit einer optischen Höhe von 15 m konzentrieren. Der Solarreaktor, welcher oben im Turm installiert ist, ist nach unten in Richtung der Heliostaten ausgerichtet. Die sich verzahnende Struktur von RPC Teilstücken ist angepasst an den entsprechenden Neigungswinkel von 40 Grad. Mithilfe dieses adaptierten Solarreaktors wird ein maximaler energetischer Wirkungsgrad zur Spaltung von CO_2 von 5.6±1.0% bei einer solaren Eingangsleistung von 55.8±8.2 kW experimentell demonstriert. Die Simulation desselben Experiments mithilfe des transienten Wärmetransportmodells enthüllt wie die Leistungsfähigkeit des Reaktors weiter gesteigert werden könnte. Bei einer Eingangsleistung von 55.8 kW geht 21.0% der gesamten solaren Energiezufuhr durch Rückstrahlung von der heissen Kavität verloren. Mit Abstand am meisten Energie wird jedoch benötigt um das Cerdioxid und die restlichen Reaktorbestandteile aufzuheizen, nämlich 58.4% der solaren Energiezufuhr. Diese Energie geht grösstenteils verloren wenn der Reaktor auf die Oxidationstemperatur abkühlt. Diese Erkenntnis betont die Notwendigkeit der Implementierung von Wärmerückgewinnung um den Wirkungsgrad solcher Reaktortechnologie in Zukunft noch weiter zu steigern.

Für das gleichzeitige Spalten von H_2O und CO_2 im Solarreaktor werden verschiedene Möglichkeiten aufgezeigt um die Zusammensetzung des produzierten Synthesegases zu regulieren. Unter optimalen Betriebsbedingungen werden ausserdem 62 aufeinanderfolgende Redox-Zyklen mit derselben Kavität aus Cerdioxid RPCs durchgeführt. Das produzierte Synthesegas wird gesammelt

und in einem Druckbehälter gelagert. Das gesammelte Synthesegas wird im Rahmen des europäischen Forschungsprojekts SUN-to-LIQUID mittels Fischer-Tropsch Synthese vor Ort zu flüssigen Kohlenwasserstoff-Treibstoffen weiterverarbeitet.

Diese Arbeit demonstriert die technische Umsetzbarkeit der solaren thermochemischen Spaltung von H_2O und CO_2 mittels Redox-Zyklen basierend auf Cerdioxid unter realistischen Betriebsbedingungen und in einer relevanten Grössenordnung. Als solches trägt die Arbeit zu der Entwicklung einer kommerziellen Anwendung für die Produktion von solaren Kohlenwasserstoff-Treibstoffen bei.

Acknowledgements

I am thankful to a great number of people who contributed to the successful completion of this work. Without them, this would certainly not have been possible.

First, I want to thank Prof. Dr. Aldo Steinfeld for giving me the unique opportunity to conduct my doctoral thesis under his supervision at the Professorship of Renewable Energy Carriers (PREC) at ETH Zurich. I am thankful for his confidence in my work, the autonomy granted especially while not working at ETH Zurich, and the exciting opportunity to conduct a large part of my thesis in Spain.

I thank Prof. Dr. Martin Kaltschmitt from the Technical University of Hamburg for acting as co-examiner of my thesis.

My very special thanks go to Dr. Erik Koepf who directly supervised my work during the first two years and kept on offering his advice when needed even while he did not work for ETH Zurich anymore. I thank him for his guidance and support especially in tougher times, for countless fruitful discussions, and for his friendship.

I would like to thank the members of IMDEA Energy Institute in Móstoles, Spain, for hosting us during more than two years. Thanks go to Dr. Manuel Romero and Dr. José González for making the collaboration possible, and to Dr. Salvador Luque, Alejandro Martínez, Dr. Iván Bravo, David Herrero, Álvaro Hervás, and all the other present and former members of the high-temperature processes unit for their support and the great working atmosphere.

I thank all the members of the SUN-to-LIQUID project that I did not mention yet for the combined efforts to succeed in our very ambitious goals. These are Dr. Andreas Sizmann, Dr. Valentin Batteiger and Dr. Christoph Falter from

Bauhaus Luftfahrt, Dr. Stefan Brendelberger, Martin Thelen, Dr. Patrick Le Clercq and Stylianos Kyrimis from the German Aerospace Center (DLR), Dr. Javier Dufour, Dr. Diego Iribarren and Dr. José Luis Gálvez from the system analysis unit of IMDEA Energy Institute, Dr. Dick Lieftink, Marco Smeltink, Wim van Es and Dr. Ellart de Wit from HyGear Technology & Services B.V., Dr. Martin Dietz, Amrita Choudhary and Justine Curtit from ARTTIC S.A.S, and Dr. Cristina Prieto Rios and Antón López from Abengoa Energía.

I would also like to thank the members of the former Solar Technology Laboratory at Paul Scherrer Institute (PSI) in Villigen, Switzerland, for hosting us during the experiments with the high-flux solar simulator and while preparing the setup for shipping to Spain. Thanks go to Dr. Christian Wieckert for letting us use the laboratories and workspaces, and to Yvonne Bäuerle for technical support.

I thank Martin Keller for the development of the data acquisition and control system that we used during the experiments in Spain and for the numerous things that he taught me about electronics.

I would like to express my gratitude to all my colleagues at the PREC for their support, for creating a great working atmosphere and for good times that we spent together also outside of work. Very special thanks go to Adriano Patané for the unforgettable time spent together in Spain, for his expertise as a mechanic and for many unconventional solutions to problems that might seem easy but can get complicated to solve when you are in Spain. I thank Philipp Haueter for the initial design of the solar reactor and his technical support. Furthermore, I want to thank Dr. Philipp Furler for introducing me to the area of research, Philipp Roos for setting high standards of quality when manufacturing the first ceria structures for the scaled-up solar reactor, Fabian Dähler for providing the template for this thesis, and Remo Schäppi and Mario Zuber for their assistance and flexibility while manufacturing new ceria structures. I also want to acknowledge the administrative support by Leonore Noll and Silvia Christoffel. Sorry for all the unusual requests and the trouble caused by the stay abroad.

It was a great pleasure to serve as a supervisor of several students performing their master theses at the PREC. I want to thank Patrick Davenport, Carlos Larrea, Dustin Nizamian and Marco Stephan not only for their excellent work, but also for the many adventures we experienced together in Spain.

The financial support by the EU's Horizon 2020 research and innovation program (Grant No. 654408) and the Swiss State Secretariat for Education, Research and Innovation (Grant No. 15.0330) is gratefully acknowledged.

Most importantly, I would like to express my deepest gratitude to my amazing friends and family, for making me feel at home in Madrid but also in Switzerland whenever I came for a visit, and for their support when I needed it the most. This thesis is dedicated to them.

Contents

Nomenclature

Latin characters

A_{fs}	fluid-solid area density	m^{-1}
C	solar concentration ratio	suns
c_p	heat capacity	J mol^{-1} K^{-1}
d_m	mean pore diameter	m
E_{inert}	energy required for inert gas separation	J mol^{-1}
h	enthalpy	J
h_{fs}	interfacial heat transfer coefficient	W m^{-2} K^{-1}
ΔH_{CO}	higher heating value of CO	J mol^{-1}
ΔH_{fuel}	higher heating value of the fuel	J mol^{-1}
ΔH_{O_2}	reaction enthalpy	kJ mol^{-1}
ΔH_{H_2}	higher heating value of H_2	J mol^{-1}
I	radiation intensity	W m^{-2}
I_b	blackbody radiation emission intensity	W m^{-2}
k	thermal conductivity	W m^{-1} K^{-1}
k_{eff}	effective thermal conductivity of ceria RPC	W m^{-1} K^{-1}
M	molar mass	kg mol^{-1}
m_{RPC}	ceria RPC cavity mass loading	kg
$\dot{n}$	molar gas flow rate	mol s^{-1}
n_{fuel}	amount of fuel produced	mol
$\dot{n}_{H_2O}$	molar flow rate of H_2O during oxidation	mol s^{-1}
n_{ppi}	number of pores per inch	

P_{solar}	solar radiative power input	kW
p	pressure	Pa
p_{atm}	atmospheric pressure	Pa
p_{O_2}	oxygen partial pressure	Pa
$p_{reactor}$	reactor pressure	Pa
p_{red}	Reactor pressure at end of reduction	Pa
Q_{aux}	auxiliary energy needed in the process	J
Q_{fs}	fluid-solid heat source	W
Q_{fuel}	integrated heating value of the fuel produced	J
Q_{inert}	heat equivalent of work for inert gas separation	J
Q_{pump}	heat equivalent of work for vacuum pumping	J
Q_{sf}	solid-fluid heat source	W
Q_{solar}	solar radiative energy input	J
R	universal gas constant	J K^{-1} mol^{-1}
r	total hemispherical reflectance of ceria	
$\bar{r}$	position vector	
r_{CO}	molar rate of CO produced	mol s^{-1}
r_{fuel}	molar rate of fuel produced	mol s^{-1}
r_{H_2}	molar rate of H_2 produced	mol s^{-1}
r_{inert}	molar rate of inert gas Ar consumed	mol s^{-1}
r_{O_2}	molar rate of O_2 released	mol s^{-1}
s	path length	m
$\bar{s}$	direction vector	
$S_{radiation}$	radiation exchange source	W m^{-3}
$S_{reaction}$	reaction energy source	W m^{-3}
S_{solar}	absorbed solar radiation source	W m^{-2}/W m^{-3}

T	temperature	K
T_f	fluid temperature	K
$T_{ox,end}$	oxidation end temperature	°C
$T_{ox,start}$	oxidation start temperature	°C
T_{pump}	vacuum pump temperature	K
$T_{red,end}$	end temperature of reduction step	°C
$T_{red,start}$	start temperature of reduction step	°C
$T_{RPC,max}$	maximum temperature of RPC	°C
$T_{RPC,nom}$	nominal temperature of RPC (measured at back surface)	°C
T_s	solid temperature	K
t	time	s
t_{ox}	duration of the oxidation step	min
t_{red}	duration of the reduction step	min
t_{RPC}	RPC thickness	mm
$\dot{V}_{Ar}$	volumetric flow rate of Ar during reduction (at 273.15 K and 101'325 Pa)	L min^{-1}
$\dot{V}_{CO2}$	volumetric flow rate of CO_2 during oxidation (at 273.15 K and 101'325 Pa)	L min^{-1}
$\dot{V}_{H2O}$	volumetric flow rate of H_2O during oxidation (at 373.15 K and 101'325 Pa)	L min^{-1}
x	depth within RPC	mm

Greek characters

α	absorption coefficient	m^{-1}
β	extinction coefficient	m^{-1}
δ	nonstoichiometry of ceria	

ε	total hemispherical emittance	
$\eta_{\text{heat-to-work}}$	heat-to-work energy conversion efficiency	
η_{pump}	vacuum pumping efficiency	
$\eta_{\text{solar-to-fuel}}$	solar-to-fuel energy conversion efficiency	
ρ	density	kg m^{-3}
σ	scattering coefficient	m^{-1}
τ	transmissivity of quartz window	
τ_{RPC}	optical thickness of ceria RPC	
ϕ_{dual}	dual-scale porosity of ceria RPC	
ϕ_{single}	single-scale porosity of ceria RPC	
ϕ_{strut}	strut porosity of ceria RPC	
ω	solid angle	deg

Subscripts

Al	aluminum front
B,1−B,3	type-B thermocouple positions
ins	Al_2O_3–SiO_2 insulation
jacket	insulating jacket
K,1−K,5	type-K thermocouple positions
ox	oxidation
red	reduction
shell	stainless steel 316 shell
∞	ambient conditions

Abbreviations

CAD	computer-aided design
CCD	charge-coupled device
CPC	compound parabolic concentrator
CSP	concentrated solar power
DNI	direct normal irradiance
ETH	Swiss Federal Institute of Technology
FMAS	flux measurement acquisition system
HFSS	high-flux solar simulator
IR	infrared
MC	Monte Carlo
ppi	pores per inch
PSI	Paul Scherrer Institute
PU	polyurethane
RPC	reticulated porous ceramic
SLPM	standard liters per minute at 273.15 K and 101’325 Pa

1 Introduction

In 2017, the world's primary energy demand was around 13'972 Mtoe[1], out of which 81% was covered by fossil fuels (26.8% coal, 31.7% oil, 22.2% gas) [1]. By 2040, driven by population growth, urbanization and economic growth, the demand is expected to grow to 13'715–19'328 Mtoe, depending on the scenario chosen for calculation [1]. Meanwhile, due to the extensive use of fossil fuels over the last decades, the atmospheric concentration of CO_2 increased from the preindustrial level in the range of 275–285 ppm [2] to 405.0±0.1 ppm in 2017 [3]. In order to limit corresponding global warming, the total cumulative global anthropogenic emissions of CO_2 since the preindustrial period need to be limited, or in other words, stay within a total carbon budget. The remaining carbon budget to limit global warming to 1.5 °C is estimated to be in the range of 420–770 Gt CO_2 with substantial uncertainties, while current emissions are at 42±3 Gt CO_2 per year [4].

Regarding electricity production, many commercial technologies already exist that use renewable energy sources such as hydropower, wind, and solar. Some technologies though are hard to electrify, and especially for the aviation sector, analyses show that for many years to come, long-range travel is very likely to rely on hydrocarbon fuels because of the limited energy density of batteries [5]. For these industries, synthetic hydrocarbon fuels might be an ideal solution. They offer the added benefit of a drop-in technology, meaning that they are compatible with our existing transportation infrastructure.

Synthetic hydrocarbon fuels can either be produced from biomass, or directly from H_2O and CO_2 [6]. Following the latter approach, H_2O and CO_2 are first split into H_2 and CO, a mixture called synthesis gas or syngas. A range of technologies

[1] 1 Mtoe (million tonnes of oil equivalent) = 11.63 TWh = 41.868 PJ

exist for the highly endothermic dissociation of H_2O and/or CO_2, such as photocatalysis [7-9], electrolysis [10, 11], and thermochemical processes [12, 13]. The syngas is then converted into liquid hydrocarbon fuels such as synthetic kerosene, diesel, gasoline, or methanol via industrially implemented catalytic processes, such as the Fischer-Tropsch process [14, 15]. If the CO_2 needed for the production of the syngas is filtered from ambient air, the carbon loop is closed, as the same amount of CO_2 that is released when burning the fuel is needed for its production, and net CO_2 emissions result only from the construction and operation of the fuel production facility [16]. First commercial technologies for capturing CO_2 from ambient air are available today [17, 18]. The concept of a closed carbon cycle with all the involved process steps is schematically shown in **Figure 1.1** for the case of solar thermochemical H_2O and CO_2 splitting.

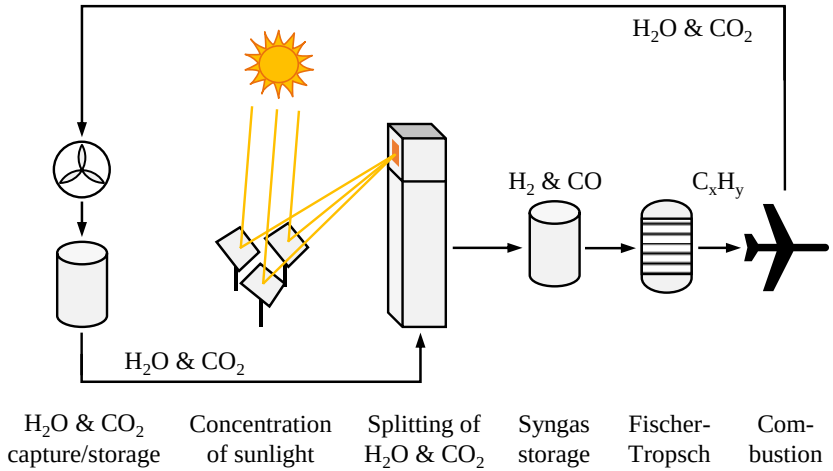

Figure 1.1. Process scheme for the production of liquid hydrocarbon fuels from concentrated sunlight, water and carbon dioxide. H_2O and CO_2 are captured and stored, and split in a solar thermochemical process, driven by concentrated sunlight, into H_2 and CO, which is stored and further processed via Fischer-Tropsch to liquid hydrocarbon fuels. The amount of CO_2 released when burning these fuels corresponds to the amount of CO_2 needed for the fuel production.

1.1 Solar thermochemical H_2O and CO_2 splitting

Using concentrated solar radiation to drive the dissociation of H_2O and CO_2 is of special interest because of the vast abundance of solar energy. The solar radiative power striking the earth's surface is around 94 PW [19], meaning that in less than two hours, the world's primary energy demand of the year 2017 (162 PWh [1]) arrives at the earth's surface by means of solar energy. H_2O and CO_2 can be thermally decomposed directly, but this requires very high temperatures [20, 21]. For H_2O splitting for example, temperatures well above 2000 K are required to obtain significant concentrations of H_2 [22]. In addition, the high temperature separation of the gaseous products or the rapid quenching of the gas mixture in order to avoid recombination is technically very challenging [23].

Two-step solar thermochemical splitting of H_2O and CO_2 offers the advantage that the fuel (H_2 and/or CO) and oxygen are released in separate steps, apart from typically lower temperatures compared to direct thermal decomposition. The two-step solar thermochemical cycle using metal oxides is schematically shown in **Figure 1.2**. In the first, endothermic reduction step, a generic metal oxide is reduced from the oxidized state (MO_{ox}) to the reduced state (MO_{red}) using concentrated solar radiation to provide the reaction enthalpy. The reduction is thermodynamically favored at high temperatures and low oxygen partial pressure (p_{O_2}). While high temperatures can be reached using concentrated solar radiation, low p_{O_2} is typically reached using an inert gas to sweep the released O_2, by lowering the total pressure, or a combination of both. In the second, exothermic oxidation step, the reduced metal oxide is re-oxidized back to the initial state with H_2O and/or CO_2 to produce H_2 and/or CO. This step is thermodynamically favored at lower temperatures, and no heat input is needed because the reaction is exothermic. The metal oxide is then recycled back to the reduction step. Because the metal oxide is not consumed in the process, the net reactions are

$$H_2O \rightarrow H_2 + \frac{1}{2}O_2 \tag{1.1}$$

$$CO_2 \rightarrow CO + \frac{1}{2}O_2 \tag{1.2}$$

with concentrated solar energy used to provide the process heat.

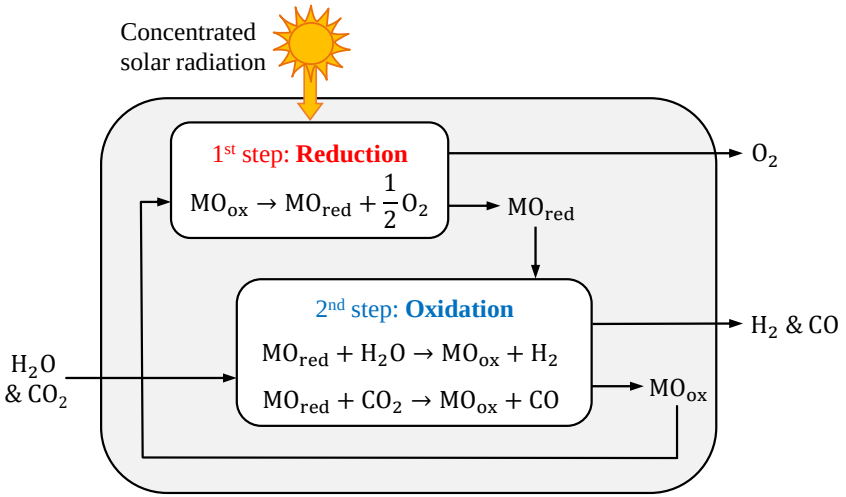

Figure 1.2. Schematic of the two-step solar thermochemical H_2O and CO_2 splitting cycle using metal oxides. In the first, endothermic step, the metal oxide is reduced from the oxidized state (MO_{ox}) to the reduced state (MO_{red}) using concentrated solar radiation to provide the process heat, thereby releasing oxygen. In the second, exothermic step, the reduced metal oxide is re-oxidized with H_2O and/or CO_2 to its initial state, thereby producing H_2 and/or CO. The metal oxide is then recycled to the reduction step.

The performance of a solar thermochemical cycle is typically reported in terms of the solar-to-fuel energy conversion efficiency $\eta_{\text{solar-to-fuel}}$, defined as

$$\eta_{\text{solar-to-fuel}} = \frac{\Delta H_{\text{fuel}} \cdot n_{\text{fuel}}}{Q_{\text{solar}} + Q_{\text{aux}}} \tag{1.3}$$

where ΔH_{fuel} is the higher heating value of the fuel, n_{fuel} is the amount of fuel produced, Q_{solar} is the solar energy input and Q_{aux} summarizes all auxiliary energy needed in the process, for example for inert gas separation or vacuum pumping. The efficiency $\eta_{\text{solar-to-fuel}}$ is a key indicator for solar thermochemical processes that allows comparing the performance of different technologies.

Several metal oxides have been proposed as reactive intermediates for two-step solar thermochemical splitting of H_2O and CO_2 [24-27], such as iron oxide [28-31], ferrites [32-34], zinc oxide [35-40], perovskites [41-46], ceria [47-53], and doped ceria [54-58]. These metal oxides can be categorized as volatile and non-

volatile materials. Volatile metal oxides change from the solid to the gaseous phase during reduction, while non-volatile materials remain in the solid state.

An example for a volatile cycle is the ZnO/Zn cycle. Solid ZnO thermally dissociates to gaseous Zn and O_2 at temperatures around 2000 K. To avoid the recombination of the gaseous mixture of Zn and O_2, high temperature gas separation or rapid quenching to ambient temperature is needed, which is technically challenging and implies a significant energy penalty for the process. Once at ambient temperature, the solid Zn can be stored, and the reduction and oxidation steps can be decoupled in space and in time. ZnO and volatile metal oxides in general typically offer larger oxygen exchange capacities compared to non-volatile metal oxides, meaning that they release more oxygen and as a result can produce more fuel per mass of metal oxide. Therefore, theoretical efficiencies of up to 39% are estimated for CO_2 splitting via the ZnO/Zn cycle when the solar reactor is operated at 2000 K [59]. The experimental implementation though was shown to be very challenging, especially at a relevant scale. For example, with a 100 kW reactor tested in a solar furnace, a maximum solar-to-fuel efficiency of 0.17% was measured, primarily because of low Zn yields associated with the challenging quenching of product gases [60].

Non-volatile metal oxides can be categorized as materials that react stoichiometrically and materials that release only a fraction of the oxygen contained in the lattice, thereby being reduced to a nonstoichiometric state. An example for a non-volatile, stoichiometric redox cycle is the Fe_3O_4/FeO cycle, which was the first two-step thermochemical cycle proposed for hydrogen production in 1977 [31]. For the thermal decomposition of magnetite (Fe_3O_4) to iron oxide (FeO), temperatures of up to 2500 K are necessary, which hinders the technical implementation of the process. The reduction temperature can be lowered by introducing small amounts of other metals such as Co, Ni, Zn or Mn into the iron oxide, a process called doping, to form mixed-metal ferrites, and stabilizing the material with inert supports such as zirconia or yttria-stabilized zirconia [33]. This approach is followed for example within the Hydrosol project, which aims to build a hydrogen production plant with a thermal power input of 750 kW that consists of three identical solar reactors with directly irradiated,

porous monoliths of pure nickel-ferrite, developed by the German Aerospace Center (DLR) [61]. Remaining problems with ferrites are sintering and side reactions with supporting materials that can lead to a rapid degradation of active material over time [29, 62].

Examples for nonstoichiometric, non-volatile metal oxides are doped and undoped ceria and perovskites. A generic representation of perovskites is ABO_3, where A and B denote metal cations that can be doped with many different materials [45]. Some perovskites show relatively high reduction extents at moderate temperature, but good reduction characteristics usually come at the expense of unfavorable oxidation characteristics, such as low oxidation temperatures or the need for a large excess of the oxidant gas [46]. However, due to the huge number of possible perovskites, the screening of potential candidates and testing for cycling performance and stability is ongoing research.

1.2 The ceria cycle

Ceria, or cerium dioxide (CeO_2), has emerged as an attractive redox material and is currently considered the state-of-the-art material for solar thermochemical H_2O and CO_2 splitting. It offers a relatively large oxygen exchange capacity (i.e. high nonstoichiometry) for a non-volatile, nonstoichiometric metal oxide [63-65], rapid redox kinetics [66-68] and is morphologically stable over a large range of temperatures and reduction extents [48, 69]. Cerium is the most abundant and least expensive rare earth metal with similar concentration in the earth's crust to commonplace industrial metals such as nickel or copper [70]. The two-step thermochemical cycle using ceria as reactive intermediate is represented by, first, an endothermic reduction

$$\mathrm{CeO_2} \rightarrow \mathrm{CeO_{2-\delta}} + \frac{\delta}{2}\mathrm{O_2} \tag{1.4}$$

And, second, an exothermic oxidation with H_2O and/or CO_2

$$\mathrm{CeO_{2-\delta}} + \delta\mathrm{H_2O} \rightarrow \mathrm{CeO_2} + \delta\mathrm{H_2} \tag{1.5}$$

$$\mathrm{CeO_{2-\delta}} + \delta\mathrm{CO_2} \rightarrow \mathrm{CeO_2} + \delta\mathrm{CO} \tag{1.6}$$

where δ denotes the nonstoichiometry, which is a measure of the amount of oxygen exchanged during reduction and oxidation. In the first, solar reduction step, ceria is typically reduced at low oxygen partial pressures and elevated temperatures of around 1500 °C, where the process heat is delivered by concentrated solar energy. In the second oxidation step, the reduced ceria is re-oxidized with H_2O and/or CO_2 to produce H_2 and/or CO, typically at ambient pressure and temperatures below 1000 °C. The re-oxidized ceria is then recycled back to the reduction step and because the ceria is not consumed in the process, the net reactions are $H_2O \rightarrow H_2 + 1/2\,O_2$ and/or $CO_2 \rightarrow CO + 1/2\,O_2$. Because the fuel ($H_2$ and/or CO) and O_2 are released in different steps, there is no need for high temperature gas separation or rapid quenching, and because the ceria remains in its solid phase at both the oxidized and the partially reduced state, both reaction steps can take place in the same reactor.

1.2.1 Thermodynamics

Pure stoichiometric CeO_2 has a cubic crystal structure with space group Fm3m over the whole temperature range from room temperature to the melting point of around 2475 °C and has a yellowish color [65]. At elevated temperatures and low p_{O_2}, the oxidation state partially changes from Ce^{4+} to Ce^{3+}. The resulting charge imbalances are compensated by oxygen vacancies and the release of O_2, and the color changes to blue or almost black [65]. The nonstoichiometry δ generally increases with increasing temperature and decreasing oxygen partial pressure p_{O_2}. **Figure 1.3** shows the equilibrium nonstoichiometry δ versus oxygen partial pressure p_{O_2} for different temperatures, determined experimentally using thermogravimetric measurements by Panlener et al [63]. As an example, $\delta \approx 0.05$ at $T = 1600$ °C and $p_{O_2} = 10^{-3}$ bar, whereas $\delta < 10^{-5}$ at $T = 900$ °C and $p_{O_2} = 1$ bar. This means that the oxygen exchange capacity per cycle corresponds to $\delta \approx 0.05$ or 3.3 L $kg_{CeO_2}^{-1}$ if the reduction and oxidation steps take place under the corresponding conditions and thermodynamic equilibrium is assumed in both reaction steps. At temperatures above 2000 °C, the thermal reduction of CeO_2 to Ce_2O_3 has also been demonstrated, but the process was found to be impractical due to sublimation of reactive material [71].

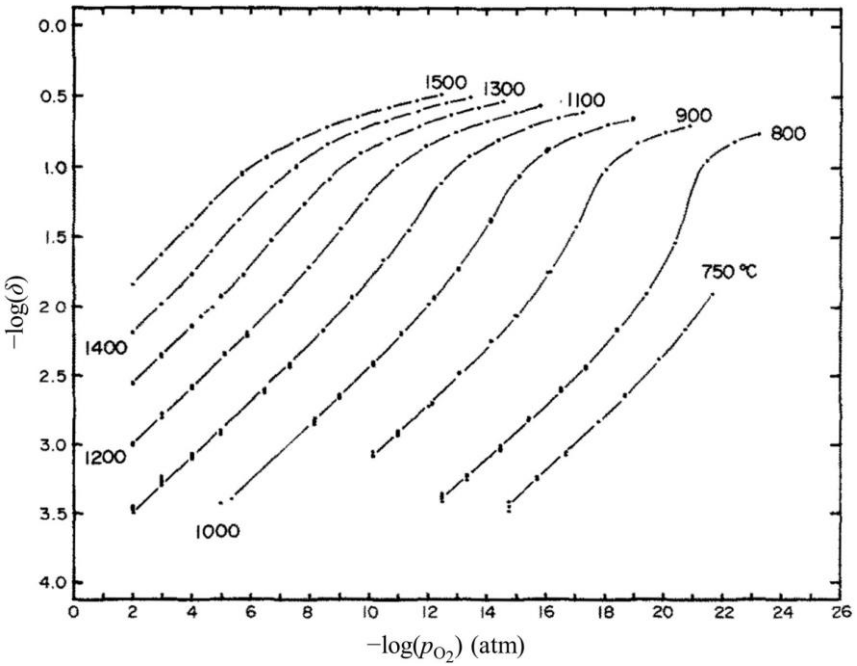

Figure 1.3. Equilibrium oxygen nonstoichiometry δ as a function of the oxygen partial pressure p_{O_2} for various temperatures in the range of 750–1500 °C [63].

Oxidation of partially reduced ceria takes place if the resulting p_{O_2} of the H_2O and/or CO_2 dissociation reaction is higher than the equilibrium p_{O_2} of ceria at the current state of δ and temperature. Therefore, the thermodynamic limit for fuel content in the product gas can be calculated for oxidation with H_2O or CO_2 according to

$$r_{H_2} = \frac{p_{H_2}}{p_{H_2O}} = \frac{K_{H_2O}}{p_{O_2}^{0.5}} \tag{1.7}$$

$$r_{CO} = \frac{p_{CO}}{p_{CO_2}} = \frac{K_{CO_2}}{p_{O_2}^{0.5}} \tag{1.8}$$

where r_{H_2} and r_{CO} are the ratios of fuel to unreacted oxidant in the product gas, K_{H_2O} and K_{CO_2} are the equilibrium constants for the H_2O and CO_2 dissociation reactions, obtained from FactSage Thermochemical Software and Databases [72], and p_{O_2} is the oxygen partial pressure at thermodynamic equilibrium

according to **Figure 1.3**. Assuming a reduction extent of $\delta = 0.05$ and an oxidation temperature of 900 °C, the corresponding p_{O_2} is $6.3 \cdot 10^{-20}$ bar, which results in maximum fuel concentrations in the product gas of around 97% for both H_2 and CO. At $T = 900$ °C but $\delta = 0.005$, the maximum fuel concentrations decrease to 9% for CO and 7% for H_2, meaning that complete re-oxidation can only be achieved if the oxidant is fed in excess. If oxidation is conducted at $T = 1600$ °C for isothermal operation with $\delta = 0.05$, p_{O_2} is $8.6 \cdot 10^{-4}$ bar and the corresponding maximum fuel concentrations are approximately 1.4% for CO and 0.35% for H_2. This means that there is a tradeoff for choosing an optimal oxidation temperature because for high oxidation temperatures, the temperature swing and corresponding heat losses between reduction and oxidation are relatively low, whereas for lower oxidation temperatures the fuel content and thus the quality of the product gas mixture is higher. Correspondingly, complete re-oxidation results in a high fuel yield per cycle but comes at the cost of diluting the product gas with a large amount of unreacted oxidant. It is therefore important to consider the product quality and to account for necessary product gas treatments when comparing different thermochemical processes.

The thermodynamic properties of ceria can be modified by introducing various dopant elements into the ceria lattice. Different dopants such as zirconium and hafnium have been shown to increase the reduction extent δ at the same temperature and p_{O_2} compared to pure ceria [55, 56, 73, 74]. However, while these dopants can help to increase the reduction extent, they usually deteriorate the oxidation properties. To date, no material is known that outperforms ceria in both the reduction and the oxidation step.

1.2.2 Kinetics

During reduction and oxidation, oxygen atoms have to be removed from or introduced into the crystal lattice, and ceria is known for its high oxygen diffusion coefficient [66, 68]. As a result, the ceria reduction reaction in a solar reactor is typically limited by the heating rate or by the oxygen partial pressure in the reactor if the product gas is not efficiently removed. This has been verified experimentally by Furler et al. [50] who showed that the measured

nonstoichiometry δ coincides with the thermal equilibrium at different temperatures in an exemplary solar reactor. During oxidation, the gaseous reactants H_2O and CO_2 adsorb and split into H_2 and CO on the ceria surface. By comparing different porous ceria structures in thermogravimetric analyses and in a solar reactor, it was found that the oxidation rates scale with the specific surface area of these structures [51, 75]. Chueh et al. [48] observed that the oxidation rate of Sm doped ceria strongly increases when depositing Rh to the surface to serve as a catalyst. They concluded that a step involving the surface must be rate-limiting and that bulk oxygen diffusion is much too rapid to have any detrimental impact on fuel production rates. Ackermann et al. [67] analyzed in detail the kinetics of ceria oxidation with CO_2. They observed that oxidation rates increase with increasing temperature up to $T \approx 520$ °C, with increasing CO_2 concentration, and also with increasing reduction extent for $\delta < 0.06$.

1.2.3 Solar reactors

Various solar reactor concepts have been proposed to affect the ceria redox cycle, including cavity receiver-reactors with rotating [76, 77], moving [78] or stationary [49, 53, 79] bulk ceria structures, and particle reactors with a moving bed [80-82] or an aerosol flow [52] of ceria particles. **Figure 1.4** shows a selection of reactor concepts that have been demonstrated experimentally. The concept of an aerosol flow reactor, developed at ETH Zurich, is illustrated in **Figure 1.4 (a)** [52]. Ceria particles continuously fall through an alumina tube positioned inside an insulated cavity-receiver. In counter-flow, an inert gas is injected from the bottom of the tube, ensuring the separation of evolving oxygen and the reduced ceria particles. A maximum efficiency of $\eta_{\text{solar-to-fuel}} = 0.56\%$ was calculated for experiments conducted in a high-flux solar simulator, assuming complete re-oxidation of the reduced particles, which was not demonstrated [52]. The sensible heat of the hot ceria particles and the inert gas stream was not recovered. The authors conclude that the reactor concept requires the selection of appropriate particle sizes that avoid radiative heat transfer limitations and of corresponding gas flow rates that enhance gas advection but avoid particle entrainment.

Figure 1.4 (b) shows an isothermal reactor concept developed at the University of Minnesota [79]. Multiple sets of concentric tubes line the wall of the cavity-receiver, with the gap between the concentric tubes filled with a bed of ceria particles. The solar reactor was built and tested experimentally with a slightly adapted design [83]. The reactor was operated at a steady temperature of 1750 K in a high-flux solar simulator at a power input of 4.4 kW. Reduction was performed by lowering the oxygen partial pressure through flushing with nitrogen, and oxidation was initiated by switching from nitrogen to CO_2. Behind the reaction zone, the concentric tubes acted as counter-flow heat exchangers to recover the sensible heat of the hot gases. Stable operation over 45 cycles was shown, but the performance was relatively poor due to the limitations of isothermal operation. When accounting for the energy needed to produce the inert gas nitrogen, an efficiency of $\eta_{\text{solar-to-fuel}} = 0.72\%$ was measured and CO_2 had to be fed with a large excess during oxidation, which decreases the value of the product gas mixture [83]. The authors therefore conclude that the isothermal approach is not attractive for future developments due to the thermodynamic limitations.

A third reactor concept that addresses solid heat recovery between the high-temperature reduction step and the low-temperature oxidation step is shown in **Figure 1.4 (c)** [84]. The counter-rotating-ring receiver/reactor/recuperator (CR5) was developed at Sandia National Laboratories. A set of rings of reactive material are directly heated by concentrated solar radiation at the top of the reactor and reduced in an inert gas atmosphere. At the bottom of the reactor, oxidation takes place at lower temperatures with H_2O and/or CO_2. Adjacent rings are rotated from the reduction zone to the oxidation zone in opposing directions. Thereby, heat is recuperated from the solid phases, as a hot ring moving out of the reduction zone preheats the adjacent rings moving into the reduction zone. The reactor concept was first proposed for ferrites as reactive material, but later also tested with ceria [84-86]. The heat recuperation concept was demonstrated to work, but difficulties arose during the experiments such as cracking of the rotating structures and mixing of gases between the reduction and oxidation zones, which limited the efficiency $\eta_{\text{solar-to-fuel}}$ to values below 1% [86].

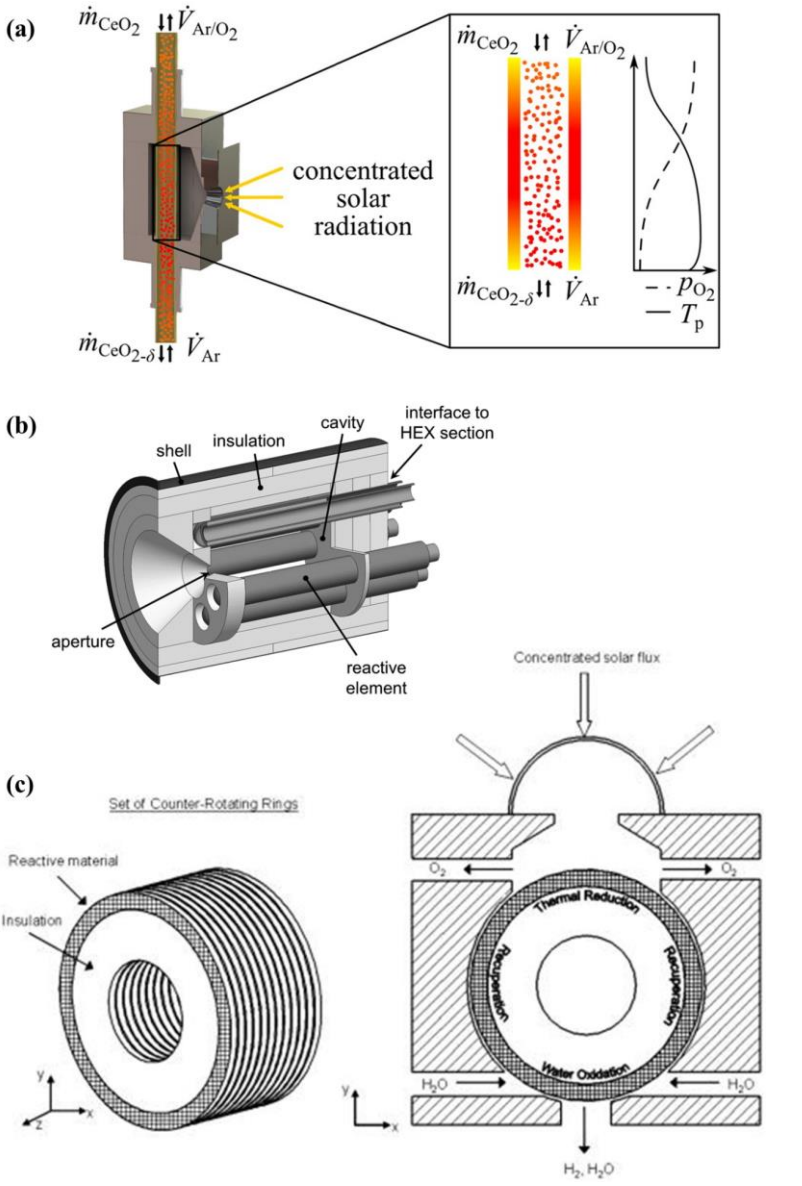

Figure 1.4. Different solar reactor concepts to affect the ceria redox cycle that have been experimentally demonstrated: **(a)** Indirectly irradiated, falling ceria particles [52]. **(b)** Indirectly irradiated, stationary bed of ceria particles cycled isothermally [79]. **(c)** Directly irradiated, rotating reactive rings incorporating heat recovery from solids [84].

This thesis is based on another reactor concept using static, bulk ceria structures that has been pursued and continuously improved at ETH Zurich. A first reactor was developed in a joint collaboration between ETH Zurich, the California Institute of Technology and Paul Scherrer Institute (PSI) [49] and tested with different directly irradiated, porous ceria structures [49-51, 87]. A schematic of the reactor is shown in **Figure 1.5 (a)**. It is a windowed cavity-receiver reactor that was operated with a temperature swing, thereby effecting both steps of the redox cycle in a single and stationary reaction vessel. The reactor was used to perform 243 H_2O/CO_2 co-splitting cycles in a high-flux solar simulator (HFSS), yielding 700 standard liters of syngas (including 30.5% of unreacted CO_2 and 16.5% of the inert gas Ar) with an average efficiency of $\eta_{\text{solar-to-fuel}} = 0.77\%$ [51]. The syngas was collected and processed via Fischer-Tropsch synthesis to a mixture of naphtha, gasoil and kerosene, thereby demonstrating the entire production chain of renewable jet fuel from H_2O and CO_2. The solar reactor was analyzed numerically using a heat and mass transfer model [88], and based on the lessons learnt with the first reactor, ETH Zurich developed a second generation solar reactor that featured superior geometry for a more uniform temperature distribution and an enhanced flow field inside the reactor, as illustrated in **Figure 1.5 (b)** [53]. This cavity-receiver reactor at the 4 kW scale contained a directly irradiated ceria reticulated porous ceramic (RPC) structure. The RPC featured dual-scale porosity, with millimeter-scale pores for efficient radiative heat transfer and micrometer-scale pores to increase the specific surface area for enhanced oxidation kinetics. The solar reactor was operated with a combined temperature and pressure swing. The reactor was tested in a HFSS for CO_2 splitting, and a solar-to-fuel energy conversion efficiency of $\eta_{\text{solar-to-fuel}} = 5.25\%$ was demonstrated as well as, in a separate experiment, a cumulative CO_2-to-CO molar conversion, integrated over oxidation time, that attained a peak value of 65% before oxidation was completed [53]. The combined temperature and pressure swing operation was compared to only a temperature swing operation when conducting the reduction step under atmospheric pressure with a large inert gas flow rate, and it was concluded that the reduction of the oxygen partial pressure by vacuum pumping is more efficient than by the use of an inert gas [53].

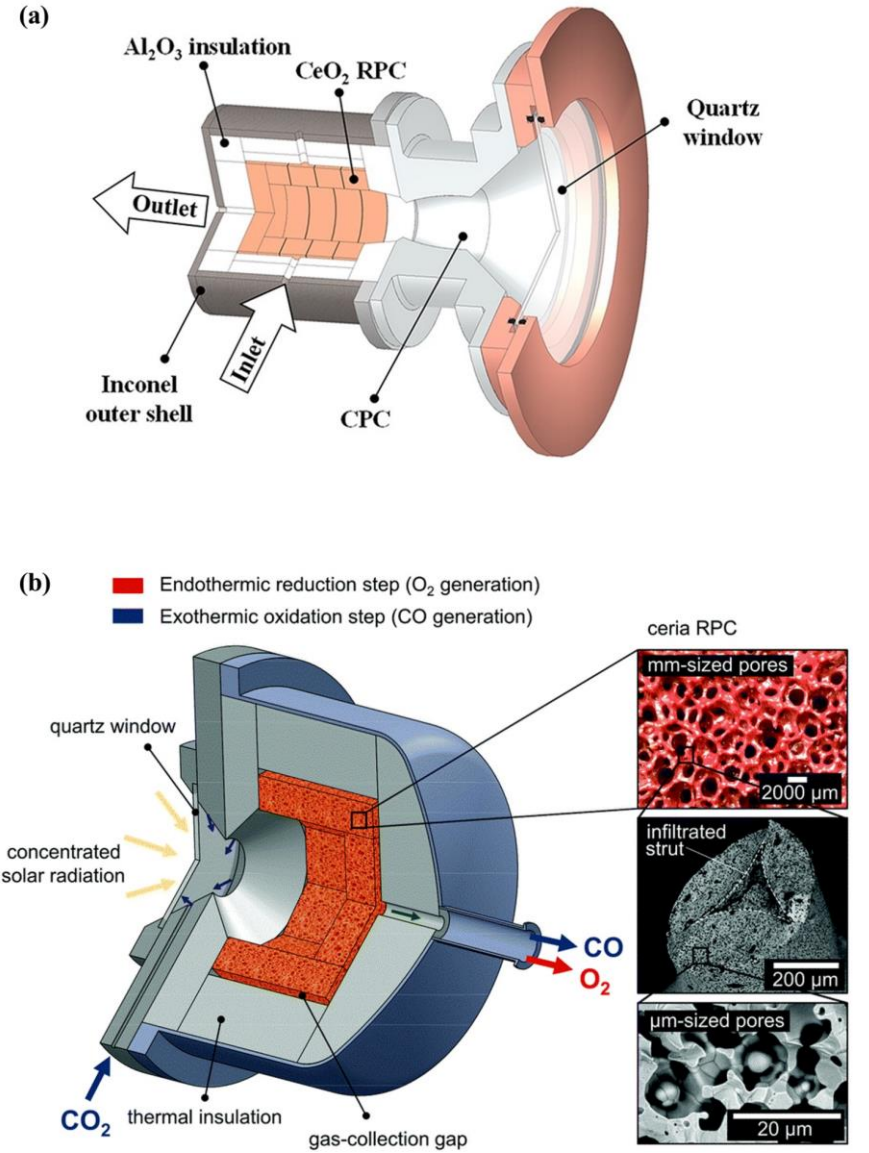

Figure 1.5. Schematics of **(a)** the first generation [50] and **(b)** the second generation [53] of cavity-receiver reactors for the two-step solar thermochemical ceria cycle developed at ETH Zurich. The former was tested with different porous ceria structures, while the latter featured a ceria reticulated porous ceramic (RPC) structure with dual-scale porosity.

In terms of experimentally demonstrated reactor efficiency, this is the most advanced solar reactor concept, even though there is no heat recovery between the high-temperature reduction step and the oxidation step at lower temperature. It was estimated that 62.8% of the energy input during the reduction step is needed for sensible heating of the solid reactor components (including the ceria RPC), and this energy is mostly lost when the reactor naturally cools down to the oxidation temperature [53]. By implementing solid heat recovery, the efficiency could be significantly increased, as confirmed by various theoretical studies [64, 89, 90]. Brendelberger et al. [91] assessed the potential for heat recovery using a thermal storage unit with a gas as heat transfer fluid. Such a separate storage unit could be coupled to the existing solar reactor technology without any major design changes. Only the operation of the solar reactor would have to be adapted, by adding two additional process steps where the reactor is preheated with hot gas coming from the storage unit before the solar reduction step, and cooled while charging the storage unit after the reduction step, respectively. It was estimated that with such a concept, the necessary solar energy input to the reactor could be decreased by up to 40% [91]. However, this does not correspond to an increase in system efficiency by the same amount, as additional energy would be needed for pumping the heat transfer fluid through the circuit. In addition, such a heat recovery system would increase the overall cycle time and the complexity of the overall system. Nonetheless, the proposed system is relatively simple compared to other heat recovery concepts discussed in literature that usually involve moving high-temperature parts, which is technically very challenging to implement [78, 80, 84, 89, 92, 93].

1.2.4 Ceria structures for cavity-receiver reactors

Different bulk ceria structures have been tested, including electrospun fibers [94], porous monoliths [49], porous felts [87], reticulated porous ceramics (RPC) [50, 51, 75], and additive-manufactured ordered porous strucutres [95]. An ideal, static bulk structure for a directly irradiated cavity-receiver reactor combines the following characteristics:

- Large pores that enhance the penetration of incoming and internal radiation, resulting in a uniform temperature distribution across the structure when it is heated during the reduction step.
- A high specific surface area that enables fast reaction rates during the oxidation step.
- A relatively high material density to increase the ceria mass loading in the reactor for a high fuel yield per cycle.

These requirements partly contradict each other, but a good tradeoff was found in the form of RPCs with dual-scale porosity, which are also used in this thesis. Such RPCs feature millimeter-scale pores with struts containing micrometer-scale pores. While the millimeter-scale pores enhance volumetric absorption and uniform heating during the reduction step, the micrometer-scale pores within the struts increase the specific surface area for fast reaction rates during the oxidation step. The morphological stability of such RPCs with dual-scale porosity was demonstrated with 227 consecutive redox cycles in a solar reactor [51] and with 500 consecutive cycles in an IR furnace [53]. Recently, the use of additive manufacturing techniques was proposed for the fabrication of porous ceria structures [96]. This offers the possibility of fabricating ordered porous structures with a tailored porosity gradient, which could help to achieve uniform heating and realize volumetric absorption of concentrated solar radiation. However, in order to outperform RPCs with such ordered porous structures, the exact geometry needs to be well optimized.

1.2.5 Efficiency, fuel prices and competitiveness

Thermodynamic analyses predict that for the two-step temperature and pressure swing cycle with ceria, efficiencies approaching $\eta_{\text{solar-to-fuel}} = 20\%$ could be reached even without heat recovery, and with heat recovery $\eta_{\text{solar-to-fuel}} = 30\%$ could theoretically be exceeded [48, 64, 89, 97]. The exact numbers strongly depend on the assumptions used for the calculations, such as reduction and oxidation temperatures, solar concentration ratio, pumping efficiency if the reduction step takes place under vacuum, energy penalties for the production of inert gases and the separation of product gases, and gas and solid heat recovery

effectiveness. So far, the highest experimentally demonstrated efficiency for the ceria cycle is $\eta_{\text{solar-to-fuel}} = 5.25\%$ for CO_2 splitting [53], but also this number depends on the chosen system boundaries and the assumptions used for the calculation of energy penalties.

Falter et al. [16] conducted a detailed economic analysis to calculate the expected fuel price for jet fuel production from seawater and ambient air via the solar ceria cycle. The outcome of such economic analyses depends even more on the underlying assumptions. Assuming, amongst other things, a solar tower concentration efficiency of 51.7% and an efficiency of the solar reactor of $\eta_{\text{solar-to-fuel}} = 20\%$ (accounting for the energy needed to separate unreacted CO_2 from the product gas mixture), they calculated an overall process efficiency of 5.0% and a price of 2.23 €/L of jet fuel [16]. For more optimistic assumptions (solar reactor efficiency of $\eta_{\text{solar-to-fuel}} = 30\%$, higher annual irradiation at the plant location, lower CO_2 and heliostat costs), the price dropped to 1.28 €/L. In a similar study, Kim et al. [98] calculated a minimum selling price of about 1.50 €/L of gasoline equivalent, assuming a conversion efficiency of 20% from unconcentrated sunlight to syngas. In a different study, Falter et al. [99] analyzed the water footprint and the land requirement for solar thermochemical jet fuel production via the ceria cycle. They concluded that both the water footprint and the land requirement are larger than for the best power-to-liquid pathways (i.e. electrolysis powered with electricity from renewable sources), but an order of magnitude lower than for the best biomass-to-liquid pathways, with the added benefit that arid regions are best-suited for the solar thermochemical pathway, therefore not competing with food production [99]. Siegel et al. [100] assert that any thermochemical fuel process must achieve a solar-to-fuel efficiency of 20%, including the optical efficiency of the solar concentrating facility and energy losses associated with processing of the fuel product such as gas separation, to be superior to solar powered low-temperature electrolysis. Depending on the efficiencies of solar concentration and fuel processing, this easily translates into reactor-only efficiencies of 30% and more.

1.3 Thesis goal and outline

This thesis was performed in the framework of the European Union Horizon 2020 project SUN-to-LIQUID. The goal of the SUN-to-LIQUID project was to demonstrate liquid hydrocarbon fuels production from concentrated sunlight, water and CO_2 under real-world conditions and at a relevant scale, using three different subsystems installed in Móstoles, Spain: a high-flux solar concentrating heliostat field and tower, a solar thermochemical reactor system based on the ceria cycle, and a gas-to-liquid conversion plant working with the Fischer-Tropsch process. This thesis deals with the development, commissioning, experimental assessment, and optimization of the solar reactor system. The solar reactor technology is based on ETH's batch-type cavity-receiver reactor previously introduced (see **Figure 1.5**), but realized at a roughly tenfold bigger scale.

The thesis is structured in three main chapters, describing the path from reactor development to the successful implementation in the fuel production facility in Spain.

In chapter 2, the design of the solar reactor is presented, including three different reactor cavities assembled as an interlocking structure of ceria RPCs. The solar reactor is tested for CO_2 splitting in a high-flux solar simulator, and conclusions are drawn on how to improve the ceria RPC cavities.

In chapter 3, a numerical heat transfer model of the solar reactor is described. The reactor model was experimentally validated with results from chapter 2 that were obtained in the high-flux solar simulator. A parametric study of crucial operational parameters of the reactor and design variables for the ceria RPC cavity is conducted, and potential paths to improve the reactor technology are discussed.

Chapter 4 presents the solar fuels production facility in Móstoles, Spain. The solar reactor is slightly adapted for the operation in the solar tower, and contains an optimized ceria RPC cavity that was designed and built based on the lessons learnt from the initial testing in the solar simulator and the numerical heat transfer model. The performance of the solar reactor is experimentally assessed and

optimized for maximum solar-to-fuel energy conversion efficiency as well as for optimal fuel composition for the downstream Fischer-Tropsch process. Using optimal operational conditions, 62 consecutive redox cycles are performed with the same ceria RPC cavity to assess the cycling stability and to produce a significant amount of syngas that can be processed on-site to liquid hydrocarbon fuels via Fischer-Tropsch synthesis.

Finally, chapter 5 concludes the thesis with an outlook and recommendations for future research.

2 Design and testing of a 50 kW solar reactor[1]

In this chapter, the design of the 50 kW solar reactor for pressure and temperature swing thermochemical redox cycling is presented and the reactor is experimentally tested for CO_2 splitting in a high-flux solar simulator. Three different reactor cavities made of an interlocking structure of ceria reticulated porous ceramic (RPC) bricks are tested. The results indicate the benefit of a big ceria mass loading for the mechanical integrity of the RPC cavity, but also highlight that the reactor performance does not increase by adding mass without ensuring effective volumetric absorption of the solar radiation and uniform heating of the ceria. A maximum solar-to-fuel energy conversion efficiency of $\eta_{\text{solar-to-fuel}} = 3.48 \pm 0.08\%$ is measured, with the relatively low efficiency attributed to the limited power of the high-flux solar simulator that is below the design point of the solar reactor, and an experiment with five consecutive CO_2 splitting cycles shows stable operation without observable degradation.

[1] Material in this chapter has been published in S. Zoller, E. Koepf, P. Roos, and A. Steinfeld, "Heat transfer model of a 50 kW solar receiver-reactor for thermochemical redox cycling using cerium dioxide," *Journal of Solar Energy Engineering*, 2019, 141 (2), 021014-021014-11, and has partially been extracted from P. Davenport, "Fabrication and characterization of large-scale ceria RPC structures for a 50 kW solar reactor cavity," Master Thesis, ETH Zurich, 2017, supervised by S. Zoller.

2.1 Solar reactor design and experimental methods

2.1.1 Solar receiver-reactor

The solar reactor is schematically shown in **Figure 2.1 (a)**. It is a cavity-receiver with a circular aperture of 16 cm diameter through which concentrated solar radiation enters. The aperture is sealed with a 12 mm thick circular quartz window that has a diameter of 300 mm. The window is mounted on a water-cooled aluminum front, which is screwed onto the reactor vessel made out of stainless steel. The quartz window is cooled with a continuous flow of compressed air at the outer surface. The steel shell has four lateral ports to introduce thermocouples for temperature measurements. The reactor is insulated with layers of porous Al_2O_3–SiO_2 insulation (Rath, Inc., type KVS 184/400). A detachable insulating jacket made from woven glass fibers and filled with ceramic mat board that covers the outside of the steel shell provides additional insulation. The walls of the cavity consist of an interlocking structure of ceria RPC bricks, approaching the shape of a cylinder with a base. The inner RPC surface is directly exposed to the concentrated solar radiation. Reaction and inert gases enter the reactor through tangential inlet ports behind the window to form a vortex flow that protects the window from the deposition of particles. Between the RPC and the Al_2O_3–SiO_2 insulation, there is a gap of around 10 mm thickness that facilitates gas flow through the reaction cavity. Product gases leave the reactor through a port at the back of the reactor vessel. **Figure 2.1 (b)** is a photograph of the solar reactor taken from the front. It also shows the copper tubes and nozzles on the bottom right that guide compressed air onto the outer surface of the quartz window to ensure continuous convective cooling.

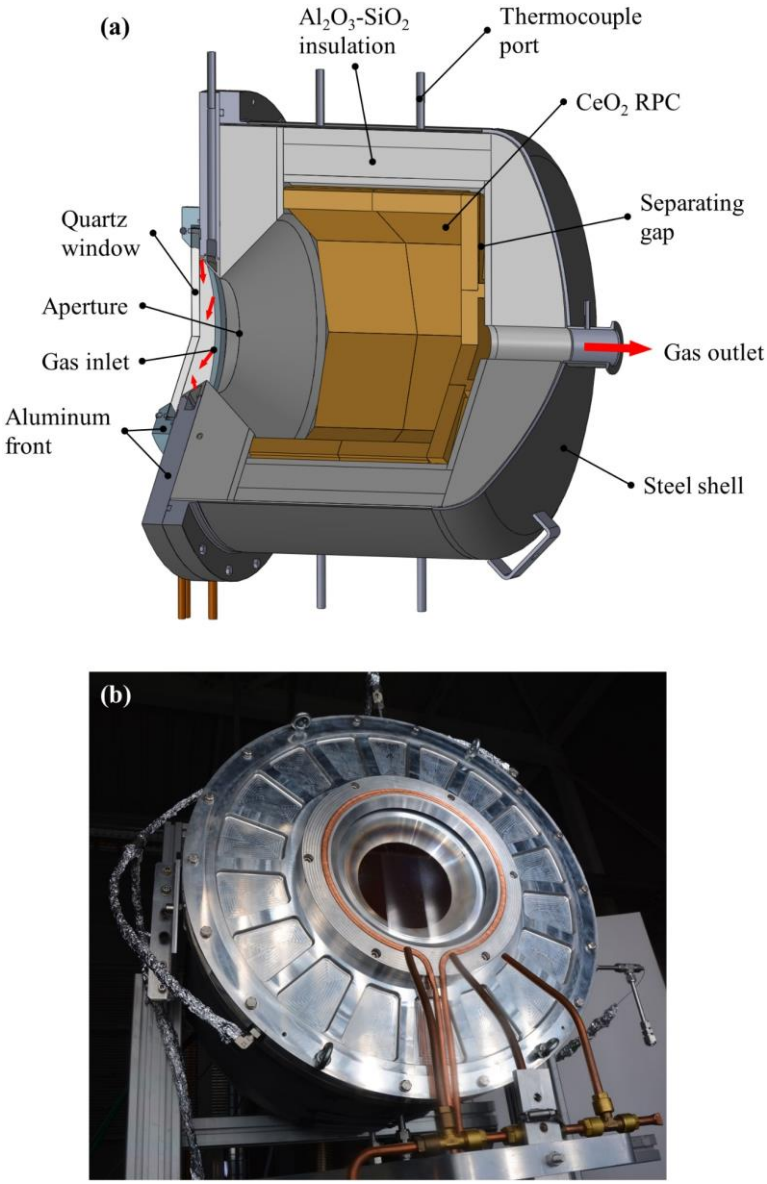

Figure 2.1. (a) Schematic of the solar reactor. It is a directly irradiated cavity receiver-reactor containing a reticulated porous ceramic (RPC) structure made of ceria. Red arrows indicate gas inlet and outlet. The detachable insulating jacket covering the outside of the steel shell is not shown here. **(b)** Photograph of the front of the solar reactor.

2.1.2 Ceria RPC structures

RPC synthesis – The ceria RPC structures were fabricated with an adapted version of the Schwartzwalder replication method [101]. The main steps of the manufacturing process are illustrated in **Figure 2.2**. In the first step, organic polyurethane (PU) foams (Foam Partner, Schaumstoff Härti AG) with a porosity of 10 ppi (pores per inch) were cut to the desired shape. The foams were then coated with a ceria-based slurry. The slurry consisted of cerium(IV) oxide powder (Sigma Aldrich, particle size < 5 μm, purity 99.9%), 30 vol% of carbon fibers (Sigrafil, SGL Group, mean fiber length 150 μm), deflocculating agent (Dolapix CE 64), binder (Optapix PA 4G), and deionized water. The exact mixture of the slurry was developed during different projects and is described elsewhere [102, 103]. After immersing the PU foams into the slurry, they were dried in air and sintered in an electrically heated furnace at 1600 °C.

Figure 2.2. Manufacturing process of ceria RPCs using the Schwartzwald replication method.

The RPC features dual-scale porosity: millimeter-scale pores with struts containing micrometer-scale pores. This is illustrated in **Figure 2.3**. The millimeter-scale pores originate from the structure of the PU foam. The organic foam burns out during sintering, resulting in the hollow inner channel of the struts that can be seen in the first inset. The second inset shows the micrometer-scale pores within the strut resulting from the carbon fibers, which also burn out while sintering. The millimeter-scale pores enhance volumetric absorption of concentrated solar radiation during the reduction step, while the micrometer-scale pores within the struts increase the specific surface area which enhances reaction kinetics during the oxidation step [75].

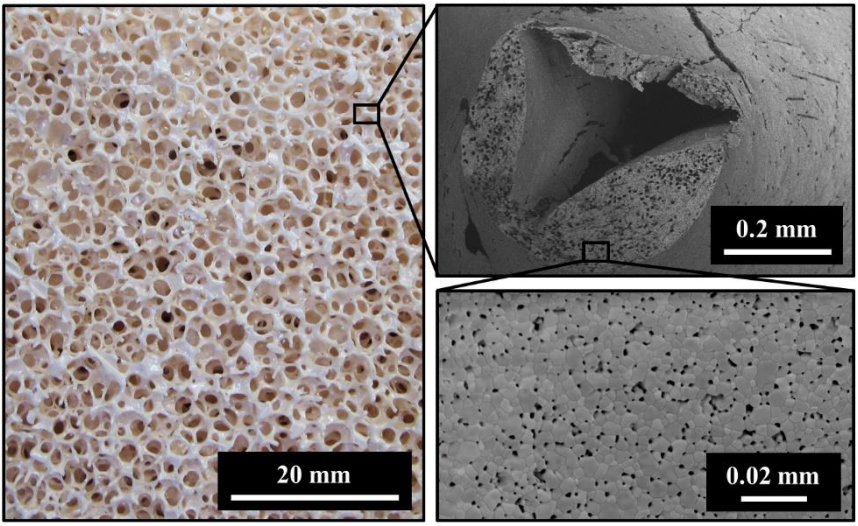

Figure 2.3. Photograph of a ceria RPC sample with visible millimeter-scale pores; the first inset is a SEM micrograph of a strut's cross section, which shows the hollow channel left by the burned polyurethane foam template; the second inset is a SEM micrograph showing the micrometer-scale pores within the strut, originating from the carbon fibers.

Design of ceria RPC cavities **–** Three different sets of ceria RPC bricks were installed and tested in the solar reactor. The key parameters of these RPC cavities are summarized in **Table 2.1**. Cavities #1 and #2 have the same geometric shape, as illustrated in **Figure 2.4**. The side of these cavities is formed by two octagonal rings, each of which consisting of eight RPC bricks with a thickness of 25 mm. The back consists of a circular centerpiece surrounded by eight wedge-shaped bricks with the same thickness. The difference between cavities #1 and #2 is the RPC porosity, resulting in a different ceria mass loading, while the total volume of the RPCs is identical. The dual-scale porosity ϕ_{dual}, defined as the fraction of the volume of all voids over the total volume, is 0.78 for cavity #1, compared to 0.72 for cavity #2. It was calculated by measuring the mass and the total volume of the RPCs. Cavity #3 consists of a larger number of RPC bricks, each having a thickness of 50 mm. The side of the cavity is also formed by two rings, but each ring consisting of thirteen RPC bricks, thereby more closely approximating the shape of a cylinder. The back consists of a circular centerpiece and thirteen wedge-shaped bricks. To manufacture the twice as thick RPC bricks, two PU

foams were stacked on top of each other immediately after coating, because no foams were available at the desired thickness. After drying and sintering, this resulted in single, monolithic RPC bricks. For cavity #3, an additional, third-scale porosity was introduced. The side RPC bricks each featured 28 equally distributed holes with a diameter of 1 cm going halfway through the thickness of the brick. **Figure 2.5 (a)** shows a section view of such an RPC as designed in CAD and **(b)** is a photograph of a fabricated RPC with the additional third-scale pores. In order to manufacture these additional pores, the array of holes was punched into the PU foam forming the top layer of the RPC before coating. However, only half of the side bricks featured this additional porosity, while the other half and the back of the cavity consisted of the standard RPC with dual-scale porosity. The idea behind this new design was to increase the penetration depth of incoming rays to achieve a relatively uniform temperature distribution across the RPC even with the higher thickness. Because of limited resources for manufacturing and testing, only a portion of the cavity was manufactured with this additional porosity, with the main goal of testing the feasibility of manufacturing and the mechanical stability during operation in the solar reactor. Out of the same reason, the size, distribution and quantity of holes was not optimized.

Table 2.1. Specifications of the three different RPC cavities installed in the solar reactor.

Label	**#1**	**#2**	**#3**
Number of RPC bricks per lateral ring	8	8	13
Porosity specification	Dual-scale porosity	Dual-scale porosity	Partial third-scale porosity
RPC thickness t_{RPC} (mm)	25	25	50
Dual-scale porosity ϕ_{dual}	0.78	0.72	0.76
Ceria RPC mass m_{RPC} (kg)	18.3	23.3	42.9

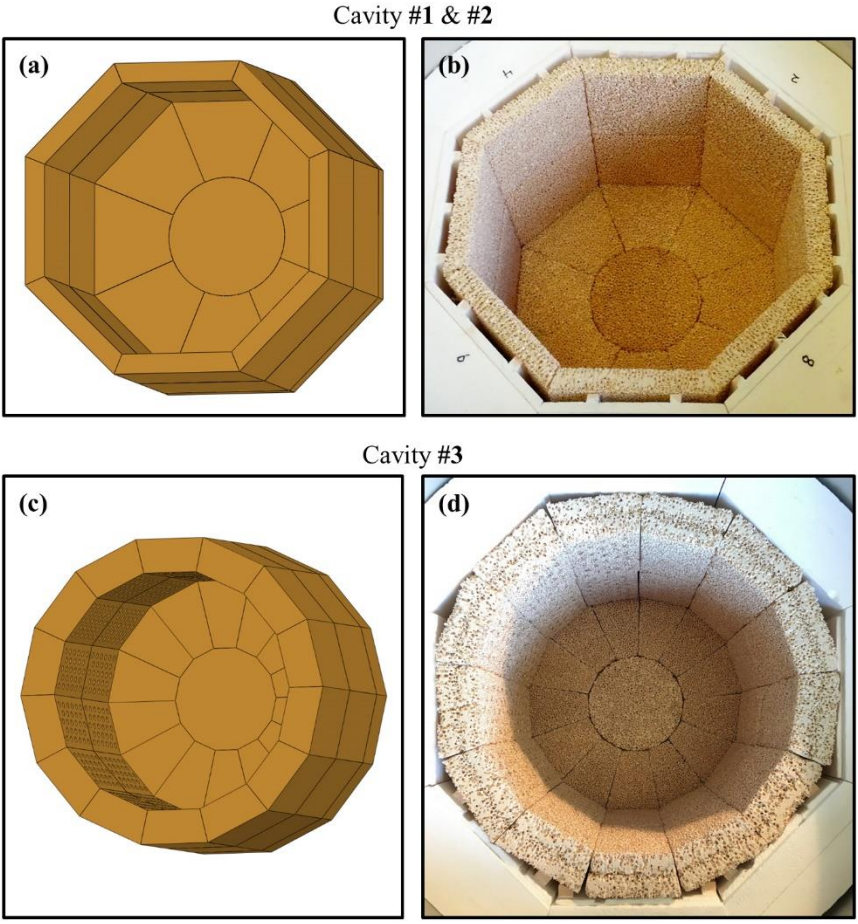

Figure 2.4. Different RPC cavity geometries tested in the solar reactor. **(a)** and **(c)** show the two different geometries as designed with CAD, while **(b)** and **(d)** are photographs of the RPCs installed in the reactor. Cavities #1 and #2 both have the same octagonal shape but differ in RPC porosity, while cavity #3 consists of more and thicker RPC bricks.

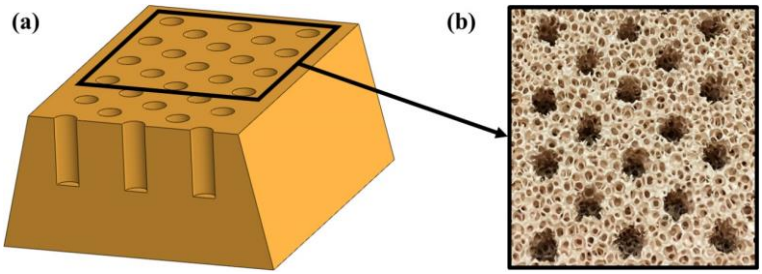

Figure 2.5. Detail view of a RPC brick from cavity #3 showing the partially implemented third-scale porosity. **(a)** is a section view of the brick as designed with CAD, while **(b)** is a photograph showing a section of a newly manufactured brick from the top.

Three-point bend testing **–** Apart from testing the RPCs in the solar reactor, the mechanical strength of these RPCs with different porosities and thicknesses was also analyzed with three-point bend testing using a type BT1 Zwick ultimate testing machine. RPC bricks with similar size as the ones installed in the solar reactor where placed on two 20 mm diameter support rods. A 20 mm diameter stamping rod was displaced at a rate of 1 mm min^{-1} until the RPC failed by cracking into two pieces and the force at failure was recorded.

2.1.3 Experimental setup and procedure

The setup for the solar reactor experiments is schematically illustrated in **Figure 2.6**. Experiments were performed at the high-flux solar simulator (HFSS) of the Paul Scherrer Institute (PSI). An array of ten xenon arc lamps, close-coupled to truncated ellipsoidal reflectors, provides an external source of intense thermal radiation, mostly in the visible and infrared spectra, which closely approximates the radiative properties of highly concentrating solar systems such as towers and dishes [104]. The radiative flux distribution at the aperture plane of the solar reactor was optically measured using a calibrated CCD camera focused onto a water-cooled, Al_2O_3 plasma-coated Lambertian target. The total solar radiative power input P_{solar} was obtained by integration of the measured flux distribution in the aperture plane, including adjusting for the absorption and reflection losses at the quartz window. Although the reactor was designed for higher power input, a maximum of P_{solar} = 32.2 kW was used due to limited power of the solar

simulator, corresponding to a solar concentration ratio of C = 1602 suns[2]. The temperature of the reacting ceria was monitored at four positions distributed over the back surface of the RPC using B-type thermocouples. The average of these temperature measurements was defined as the nominal RPC temperature $T_{RPC,nom}$. The temperature of the lateral Al_2O_3–SiO_2 insulation was measured at three different depths using K-type thermocouples. K-type thermocouples were also used to measure the temperatures of the outer lateral surfaces of the reactor shell and the insulating jacket. Gas flow rates were regulated using electronic mass flow controllers (Bronkhorst, EL-FLOW Select). The pressure inside the reactor was measured at the gas outlet using a Pirani gauge sensor combined with a capacitance diaphragm vacuum gauge (Leybold, THERMOVAC TTR 101). A dry, multi-stage roots vacuum pump (Pfeiffer Vacuum, ACP 40) was attached to the outlet port of the solar reactor via two parallel evacuation valves. A membrane valve was used to slowly evacuate the reactor at the beginning of the reduction step (path shown by the red arrows in **Figure 2.6**), and a gate valve with bigger nominal diameter was opened once the pressure was sufficiently low (< 50 mbar). During the oxidation step (path shown by the blue arrows in **Figure 2.6**), the vacuum pump was bypassed by use of a manual membrane valve. The composition of the product gas was continuously (frequency 1 Hz) analyzed downstream using an electrochemical sensor for O_2, and IR detectors for CO and CO_2 (Siemens, Ultramat 23). The gas composition was verified by gas chromatography (Agilent, 490 Micro GC) with a measurement frequency of 0.005 Hz.

[2] The solar concentration ratio C is defined as $C = P_{solar} / (I \cdot A)$, where P_{solar} is the solar radiative power intercepted by the aperture area A, and I is the direct normal solar irradiation. C is often expressed in units of "suns" when normalized to I = 1 kW m^{-2}.

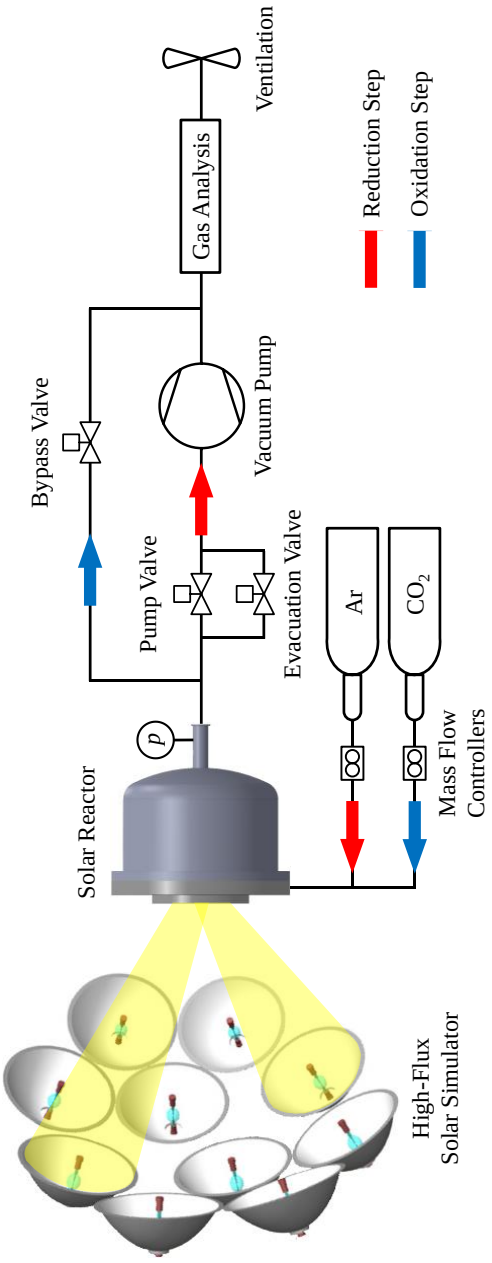

Figure 2.6. Schematic of the experimental setup. During the endothermic reduction step, Ar flow is used to protect the quartz window and is pumped out together with the released O_2, while the reactor is under vacuum and irradiated with concentrated solar radiation. During the exothermic oxidation step, the ceria is re-oxidized with CO_2, therefore producing CO.

In **Figure 2.7**, the solar reactor is shown in operation. During an experimental run, the solar reactor was first slowly preheated with a radiative power input P_{solar} between 5 and 10 kW for approximately 75 minutes, followed by a slow pre-cycle. During a pre-cycle, the reactor was heated with P_{solar} = 10−25 kW ramping up, for approximately 30 minutes until the nominal reduction temperature was reached. The pre-cycle was terminated by closing the shutters of the solar simulator (thereby effecting P_{solar} = 0 kW) and letting the reactor naturally cool down to the nominal oxidation temperature. The ceria was fully re-oxidized using CO_2. Once the nominal RPC temperature reached the defined reduction start temperature, the primary reduction step was initiated with constant P_{solar} in the range of 26.9−32.2 kW, while the reactor was evacuated using the vacuum pump. The total pressure in the reactor during the reduction step was in the range of 3−9 mbar, depending on the current rate of oxygen release. To protect the quartz window from deposition of sublimated ceria [50] and to govern the fluid flow field when operating under vacuum conditions, an argon flow rate of 5.35 L min^{-1} (SLPM; volume flow rate calculated at 273.15 K and 101’325 Pa) was introduced to the reactor directly behind the window. When the variable reduction end temperature was reached, re-oxidation was initiated by removing input power and repressurizing the reactor with CO_2. After the nominal RPC temperature fell to the oxidation start temperature by natural cooling, CO_2 was flown through the reactor at a constant rate in the range of 34−150 L min^{-1} until the ceria was fully re-oxidized, producing a mixed flow in the outlet comprised of CO and unreacted CO_2.

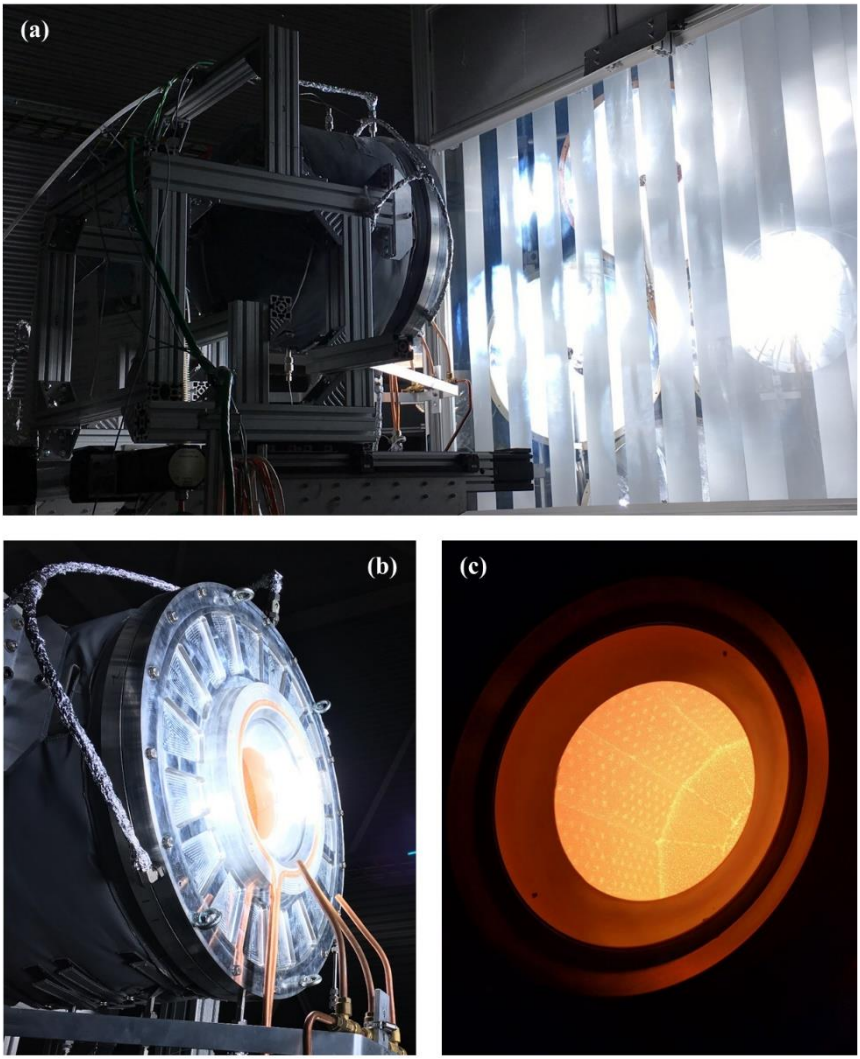

Figure 2.7. Photographs of the solar reactor in operation: **(a)** the high-flux solar simulator heating up the solar reactor during the reduction step; **(b)** the irradiated front of the reactor; **(c)** the glowing ceria RPC bricks seen through the reactor's aperture while cooling down shortly after the end of the reduction step.

2.1.4 Solar-to-fuel energy conversion efficiency

A key performance indicator of the solar reactor is the solar-to-fuel energy conversion efficiency $\eta_{\text{solar-to-fuel}}$, which is defined as

$$\eta_{\text{solar-to-fuel}} = \frac{Q_{\text{fuel}}}{Q_{\text{solar}} + Q_{\text{pump}} + Q_{\text{inert}}} \tag{2.1}$$

The energy content of the fuel produced, Q_{fuel}, is

$$Q_{\text{fuel}} = \Delta H_{\text{fuel}} \cdot \int r_{\text{fuel}} dt \tag{2.2}$$

In the case of CO_2 splitting, ΔH_{fuel} is the heating value of CO ($\Delta H_{\text{CO}} = 283$ kJ mol^{-1}), and r_{fuel} is the molar rate of CO produced. Assuming complete re-oxidation, the energy content of the fuel produced in a cycle can also be calculated as $Q_{\text{fuel}} = \Delta H_{\text{fuel}} \cdot 2\int r_{\text{O}_2} dt$, where $\int r_{\text{O}_2} dt$ is the rate of released oxygen integrated over the reduction step. Q_{solar} is the total solar energy input integrated over the reduction step, as concentrated solar energy is only delivered during the endothermic reduction, and is defined as

$$Q_{\text{solar}} = \int P_{\text{solar}} dt \tag{2.3}$$

where P_{solar} is the solar radiative power input through the reactor's aperture, plus absorption and reflection losses at the quartz window. Q_{pump} and Q_{inert} are the energy penalties associated with vacuum pumping and the consumption of the inert gas Ar during the reduction step, respectively, and are calculated as suggested in reference [53]. The vacuum pumping energy is calculated as the thermodynamic minimum pumping work divided by a heat-to-work energy conversion efficiency, $\eta_{\text{heat-to-work}}$ (assumed 0.4 [80, 105]), and a pressure dependent vacuum pumping efficiency, η_{pump}, according to

$$Q_{\text{pump}} = \frac{1}{\eta_{\text{heat-to-work}}} \cdot \int \frac{R \cdot T_{\text{pump}}}{\eta_{\text{pump}}(p_{\text{reactor}}(t))} \cdot \dot{n}(t) \cdot \ln\left(\frac{p_{\text{atm}}}{p_{\text{reactor}}(t)}\right) dt \tag{2.4}$$

where $\dot{n}(t)$ is the molar flow rate pumped out of the reactor, consisting of the inert gas Ar injected to the reactor, the O_2 released by ceria, and the gas evacuated from the reactor during transient change of pressure, R is the universal gas

constant (R = 8.314 J K^{-1} mol^{-1}), T_{pump} is the pump temperature (assumed 298.15 K), and p_{atm} and $p_{reactor}$ are atmospheric and reactor pressure, respectively. The pumping efficiency, derived by Brendelberger et al. [105], is based on the analysis of a multi-stage industrial vacuum pump arrangement from Pfeiffer vacuum and calculated as

$$\eta_{pump}\left(p_{reactor}(t)\right) = 0.07 \cdot \log\left(\frac{p_{reactor}(t)}{p_{atm}}\right) + 0.4 \tag{2.5}$$

The energy required for the separation of the inert gas Ar is defined as

$$Q_{inert} = \frac{1}{\eta_{heat\text{-}to\text{-}work}} E_{inert} \int r_{inert}\, dt \tag{2.6}$$

where E_{inert} is the work required for inert gas separation (assumed 20 kJ per mole of Ar [106]) and r_{inert} is the flow rate of the inert gas Ar during reduction. Note that $\eta_{solar\text{-}to\text{-}fuel}$ is weakly dependent on the assumptions used for the calculation of the two energy penalties, because Q_{solar} is roughly two orders of magnitude larger than Q_{pump} and Q_{inert}.

2.2 Experimental results and discussion

A typical cycle for CO_2 splitting with the RPC cavity #1 is illustrated in **Figure 2.8**. It shows the nominal RPC temperature, the reactor pressure as well as the O_2 and CO evolution rates as a function of time. The experimental conditions and measured results of the same experiment are summarized in **Table 2.2**. During the reduction step at P_{solar} = 30.5 kW and under vacuum pressure, the RPC temperature rapidly increased from 698 °C to 1504 °C in 12.4 min, corresponding to a mean heating rate of 65 °C min^{-1}. The rate of released O_2 increased with increasing temperature to a maximum of 4.5±0.1 L min^{-1}. Due to limited pumping power, the reactor pressure slightly increased the more O_2 was released, reaching 8.4±1.2 mbar at the end of the reduction step. When P_{solar} was turned off at the end of the reduction step, the O_2 release stopped and the reactor was repressurized with CO_2 while the RPC temperature started decreasing. Within 13.3 min, the reactor naturally cooled down to 1000 °C, which is when the oxidation step was initiated by flowing 68.0 L min^{-1} of CO_2 through the reactor. Shortly afterwards, a peak CO evolution rate of 14.4±0.3 L min^{-1} was

measured. Integrated over the entire oxidation step, a total of 66.4±6.3 L CO was produced. The molar ratio of CO to O_2 was 2.21±0.26, implying complete re-oxidation of the reduced ceria. The solar-to-fuel energy conversion efficiency $\eta_{\text{solar-to-fuel}}$ was 3.26±0.07%. Previous work on a similar, but significantly smaller solar reactor configuration at the 4 kW scale resulted in $\eta_{\text{solar-to-fuel}}$ = 5.25% for CO_2 splitting [53]. The relatively low efficiency is attributed to the limited power of the high-flux solar simulator. Significantly higher efficiencies are expected for the operation of the solar reactor in the solar tower in Spain at P_{solar} = 50 kW.

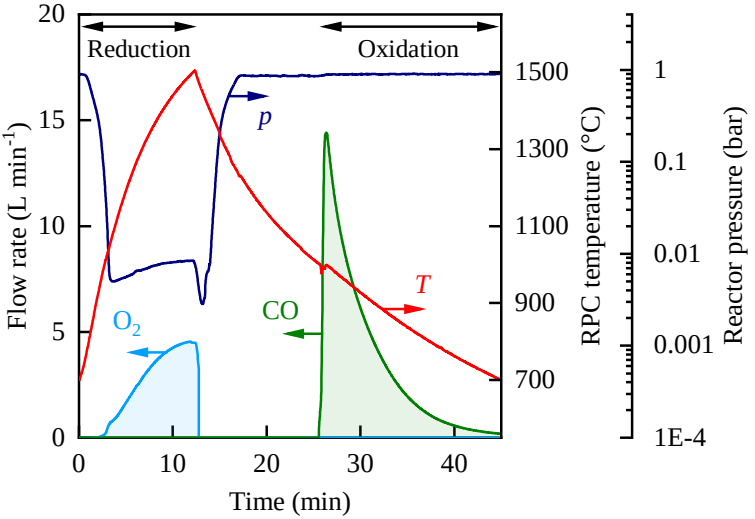

Figure 2.8. Nominal RPC temperature, reactor pressure and O_2 and CO evolution rates as a function of time during a typical CO_2 splitting cycle with the RPC cavity #1. Experimental conditions during reduction: P_{solar} = 30.5 kW, $T_{\text{red,start}}$ = 698 °C, $T_{\text{red,end}}$ = 1504 °C, $\dot{V}_{\text{Ar}}$ = 5.35 L min^{-1} at p_{reactor} < 9 mbar. Experimental conditions during oxidation: P_{solar} = 0 kW, $T_{\text{ox,start}}$ = 1000 °C, $T_{\text{ox,end}}$ = 696 °C, $\dot{V}_{CO_2}$ = 68.0 L min^{-1} at atmospheric pressure.

Table 2.2. Experimental conditions and results of a typical CO_2 splitting cycle with the ceria RPC cavity #1.

Variable	Symbol	Value	Unit
Solar radiative power input during reduction	P_{solar}	30.5	kW
Reduction start temperature	$T_{red,start}$	698	°C
Reduction end temperature	$T_{red,end}$	1504	°C
Oxidation start temperature	$T_{ox,start}$	1000	°C
Oxidation end temperature	$T_{ox,end}$	696	°C
Ar flow rate during reduction	$\dot{V}_{Ar}$	5.35	L min^{-1}
CO_2 flow rate during oxidation	$\dot{V}_{CO_2}$	68.0	L min^{-1}
Reactor pressure at end of reduction	p_{red}	8.4±1.2	mbar
Reduction duration	t_{red}	12.4	min
Oxidation duration	t_{ox}	19.7	min
Cycle duration		45.3	min
Mean heating rate		65	°C min^{-1}
Peak O_2 evolution rate		4.5±0.1	L min^{-1}
Total amount of O_2 released		30.1±0.6	L
Average nonstoichiometry of ceria	δ	0.025±0.001	
Peak CO evolution rate		14.4±0.3	L min^{-1}
Total amount of CO produced		66.4±6.3	L
Average conversion of CO_2 to CO		5.4±0.5	%
Molar ratio CO/O_2		2.21±0.26	
Vacuum pumping energy	Q_{pump}	512	kJ
Inert gas Ar separation energy	Q_{inert}	147	kJ
Solar-to-fuel energy conversion efficiency	$\eta_{solar\text{-}to\text{-}fuel}$	3.26±0.07	%

2.2.1 Variation of the solar radiative power input

To experimentally assess the influence of different solar radiative power inputs on the performance of the solar reactor, we conducted CO_2 splitting cycles with the RPC cavity #2 at three levels of P_{solar} ranging from 26.9 kW to 31.0 kW. Lower levels of P_{solar} are unfeasible because a certain amount of power is needed to reach the reduction end temperature in a reasonable amount of time, while the upper limit was set by the power limit of the high-flux solar simulator. The nominal RPC temperature as well as the O_2 and CO evolution rates are shown as a function of time in **Figure 2.9 (a)** for P_{solar} = 26.9, 29.2, and 31.0 kW. Reduction and oxidation temperatures were kept constant at $T_{red,end}$ = 1461–1464 °C, $T_{ox,start}$ = 1000 °C, and a sufficiently low oxidation end temperature of $T_{ox,end}$ = 795 °C to assure complete re-oxidation with CO_2.

Figure 2.9 (b) shows the volume of produced O_2 and CO, the reduction time and $\eta_{solar\text{-}to\text{-}fuel}$ as a function of P_{solar} for these three cycles. The amount of fuel produced per cycle is relatively stable with no visible trend, due to the identical reduction end temperatures. The reduction time though decreases significantly from 30.7 min at P_{solar} = 26.9 kW to 22.0 min at P_{solar} = 31.0 kW. As a result, $\eta_{solar\text{-}to\text{-}fuel}$ increases from 2.03±0.03% at P_{solar} = 26.9 kW to 2.34±0.06% at P_{solar} = 31.0 kW. The positive trend of increasing $\eta_{solar\text{-}to\text{-}fuel}$ with increasing P_{solar} is mainly attributed to lower heat losses by reradiation through the aperture and conduction through the reactor insulation during the shorter reduction times, and highlights the great potential for performance increase when the reactor is operated at higher P_{solar}.

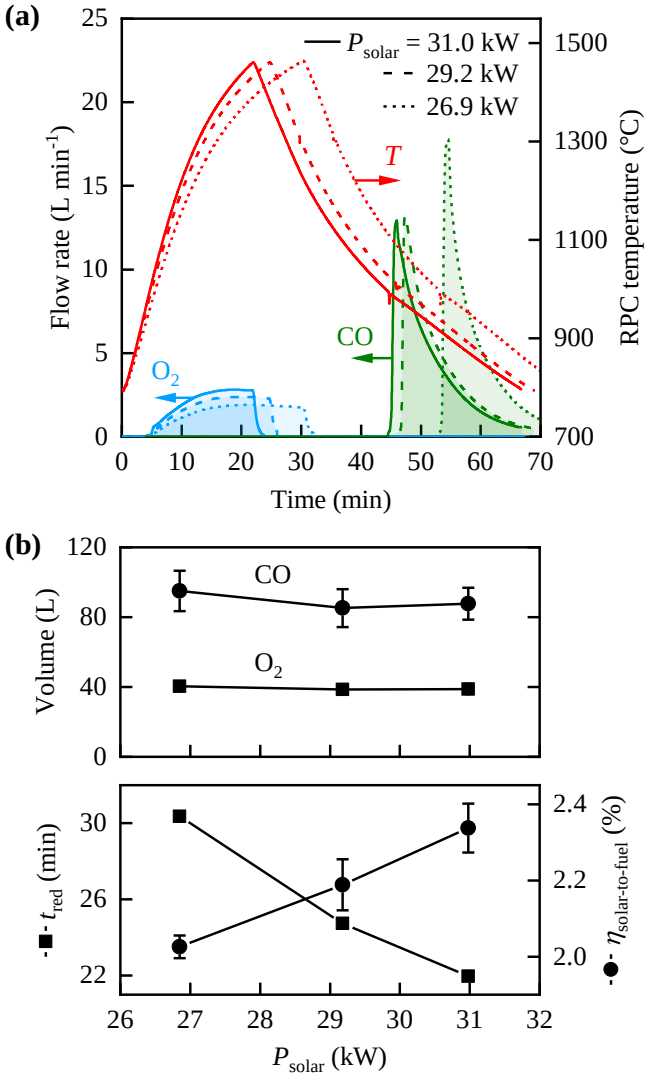

Figure 2.9. (a) Nominal RPC temperature and O_2 and CO evolution rates as a function of time for three CO_2 splitting cycles at different solar radiative power input P_{solar} during the reduction step, conducted with the RPC cavity #2. **(b)** Volume of produced O_2 and CO, reduction time t_{red} and efficiency $\eta_{solar\text{-}to\text{-}fuel}$ of the same cycles as a function of P_{solar}.

2.2.2 Comparison of different RPC cavities

The performance of the three different ceria RPC cavities during similar CO_2 splitting cycles is directly compared in **Figure 2.10**. As specified in **Table 2.1**, cavities #1 and #2 had the same geometric shape, but different dual-scale porosities of the RPC and resulting ceria RPC mass loadings (ϕ_{dual} = 0.78 and m_{RPC} = 18.3 kg for cavity #1, and ϕ_{dual} = 0.72 and m_{RPC} = 23.3 kg for cavity #2, respectively). The main difference of cavity #3 was the doubled thickness of the RPC structures (50 mm instead of 25 mm), resulting in a much higher mass loading of m_{RPC} = 42.9 kg. **Figure 2.10 (a)** shows the nominal RPC temperature as well as the O_2 and CO evolution rates as a function of time for the three cases. P_{solar} was equal to 31 kW in all three cases. The temperature gradient throughout the thickness of the RPC during the reduction step, with the highest temperature at the directly irradiated front surface and the lowest temperature at the back surface where the temperature is measured, increases both with decreasing RPC porosity and with increasing RPC thickness [107, 108]. Therefore, the reduction end temperature was set to 1512 °C for cavity #1, 1461 °C for cavity #2 and 1440 °C for cavity #3 in an attempt to reach similar maximum temperatures of the RPC structures, $T_{RPC,max}$, for all cases. These temperatures were chosen without knowing the actual values of $T_{RPC,max}$, resulting in cycles that are not perfectly comparable, but still serve as a good indicator for performance. The oxidation start temperature was 1000 °C for all cases. The flow rate of CO_2 during oxidation and the oxidation end temperature were varied, because with increasing mass loading, the solar reactor was cooling slower during oxidation, and complete re-oxidation was already achieved at higher temperatures.

In **Figure 2.10 (b)**, the volume of produced O_2 and CO, the reduction time and $\eta_{solar\text{-}to\text{-}fuel}$ is shown as a function of m_{RPC} for the three RPC cavities. Compared to RPC cavity #1, the reduction time of cavity #2 increased by 71% from 12.9 min to 22.0 min, although the mass only increased by 27% from 18.3 kg to 23.3 kg. Apart from the higher thermal mass, we attribute the longer reduction time of cavity #2 to the lower porosity that leads to a smaller penetration depth of incident radiation and less uniform heating of the RPC. The amount of fuel produced increased by 24% from 70.5±6.7 L for cavity #1 to 87.7±9.1 L for

cavity #2. As a consequence, a lower efficiency was achieved with cavity #2 ($\eta_{\text{solar-to-fuel}}$ = 2.34±0.06% compared to $\eta_{\text{solar-to-fuel}}$ = 3.34±0.06% for cavity #1).

The reduction time of the RPC cavity #3 was again significantly higher. Compared to cavity #1 it nearly tripled from 12.9 min to 35.5 min, while the mass increase was 134%. The amount of CO produced also increased from 70.5±6.7 L to 161.6±19.0 L, but this increase was not enough to compensate for the much longer reduction time. As a consequence, $\eta_{\text{solar-to-fuel}}$ was 2.36±0.06% for cavity #3, compared to $\eta_{\text{solar-to-fuel}}$ = 3.34±0.06% for cavity #1.

These results indicate that without effective volumetric absorption of the solar radiation inside the RPC structure to ensure uniform heating, increasing the ceria mass loading does not result in increased reactor performance due to slower heating. It is important to note though that the presented results could change when the reactor is operated differently, for example at higher P_{solar}. Most importantly, when designing a RPC cavity for the solar reactor, not only the performance of a single cycle should be considered, but also the stability over many consecutive cycles. This is discussed in more detail in the next section.

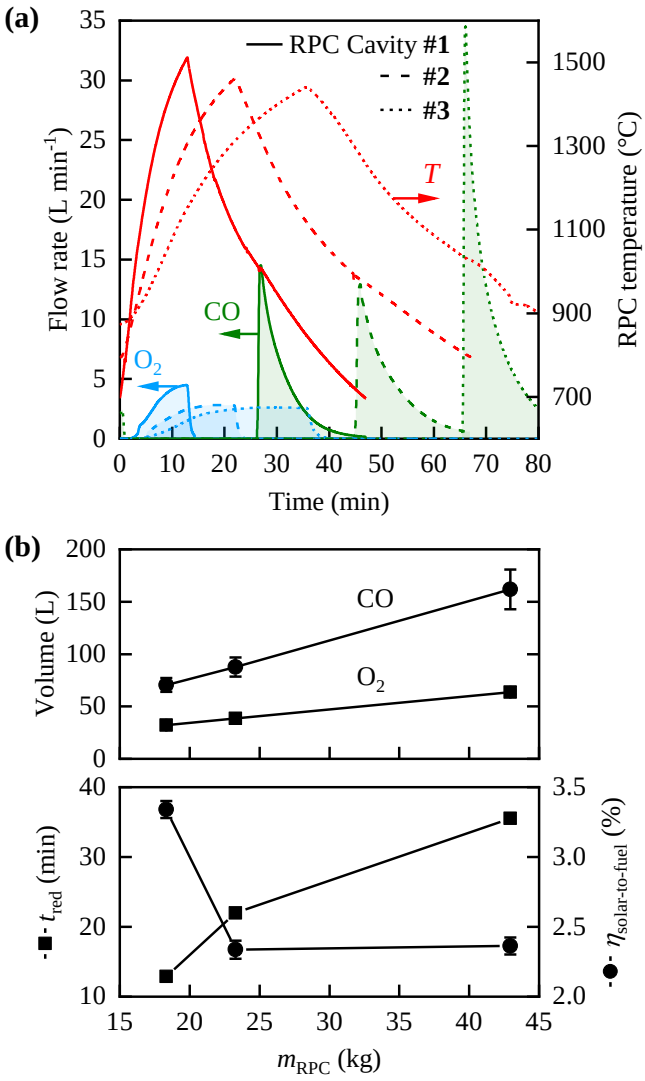

Figure 2.10. (a) Nominal RPC temperature and O_2 and CO evolution rates as a function of time for a CO_2 splitting cycle each with three different RPC cavities (see **Table 2.1** for specifications). **(b)** Volume of produced O_2 and CO, reduction time t_{red} and efficiency $\eta_{solar\text{-}to\text{-}fuel}$ of the same cycles as a function of the ceria RPC mass m_{RPC} (RPC cavity #1: 18.3 kg; #2: 23.3 kg; #3: 42.9 kg).

2.2.3 Stability observations

Consecutive cycling **–** To assess the stability of the reactor, five consecutive cycles were performed with the RPC cavity #1 with almost equal operational conditions during the different cycles. The nominal RPC temperature, reactor pressure and O_2 and CO evolution rates of these cycles are shown in **Figure 2.11**. P_{solar} was slightly increased from 30.5 kW in the first cycle to 32.2 kW in the fifth cycle. Reduction and oxidation temperatures and inlet flow rates were: $T_{red,start}$ = 696–700 °C, $T_{red,end}$ = 1504–1513 °C, $T_{ox,start}$ = 1000 °C, $T_{ox,end}$ = 696–700 °C, $\dot{V}_{Ar}$ = 5.35 L min^{-1}, $\dot{V}_{CO_2}$ = 68.0 L min^{-1}.

The reactor showed stable performance without observable degradation. The amount of produced CO varied between 66.4±6.3 L and 70.7±6.8 L per cycle. A slight increase of $\eta_{solar\text{-}to\text{-}fuel}$ was observed with increasing cycle number, with $\eta_{solar\text{-}to\text{-}fuel}$ = 3.26±0.07 for the first cycle and $\eta_{solar\text{-}to\text{-}fuel}$ = 3.48±0.08 for the last cycle, which is attributed to the slightly increased power input P_{solar}.

For the long-term operation of the solar reactor in the solar tower in Spain or a future commercial application, stable performance over a much larger number of cycles is crucial. Long-term stability of a ceria RPC with dual-scale porosity was demonstrated by Marxer et al. [53] in 500 consecutive redox cycles using an IR furnace. The O_2 yield was constant throughout the cycling, and scanning micrographs before and after cycling revealed that the micrometer-sized pores within the struts of the RPC were preserved. Apart from chemical and mechanical stability on the small scale, mechanical stability on the scale of a RPC brick is equally important. Due to the self-supporting design of the solar reactors' RPC cavity consisting of multiple separate RPC bricks, the failure of a single brick could lead to a collapse of the entire cavity and needs to be avoided.

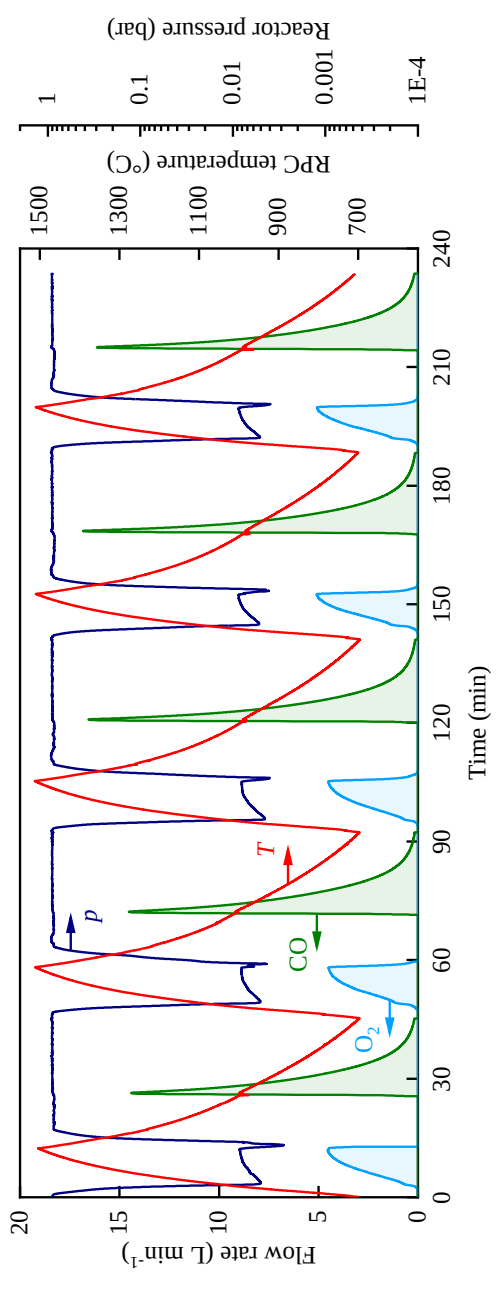

Figure 2.11. Nominal RPC temperature, reactor pressure and O_2 and CO evolution rates as a function of time for five consecutive CO_2 splitting cycles with RPC cavity #1. Experimental conditions during reduction: P_{solar} = 30.5–32.2 kW, $T_{red,start}$ = 696–700 °C, $T_{red,end}$ = 1504–1513 °C, $\dot{V}_{Ar}$ = 5.35 L min^{-1} at $p_{reactor}$ < 9 mbar. Experimental conditions during oxidation: P_{solar} = 0 kW, $T_{ox,start}$ = 1000 °C, $T_{ox,end}$ = 696–700 °C, $\dot{V}_{CO_2}$ = 68.0 L min^{-1} at atmospheric pressure.

Three-point bend testing – The mechanical strength of RPCs with different porosities and thicknesses was assessed with three-point bend testing. The methodology is described in section 2.1.2. **Figure 2.12** shows the force at failure of different RPC bricks as a function of the dual-scale porosity ϕ_{dual} for the two different RPC thicknesses of t_{RPC} = 25 mm and 50 mm. A clear trend of increasing force at failure and consequently increasing mechanical strength of the RPCs is visible with decreasing porosity ϕ_{dual}, as indicated by the dashed power function fit of the measurements with t_{RPC} = 25 mm. Doubling t_{RPC} to 50 mm also resulted in a drastic increase of the force at failure compared to RPCs with similar porosities at t_{RPC} = 25 mm.

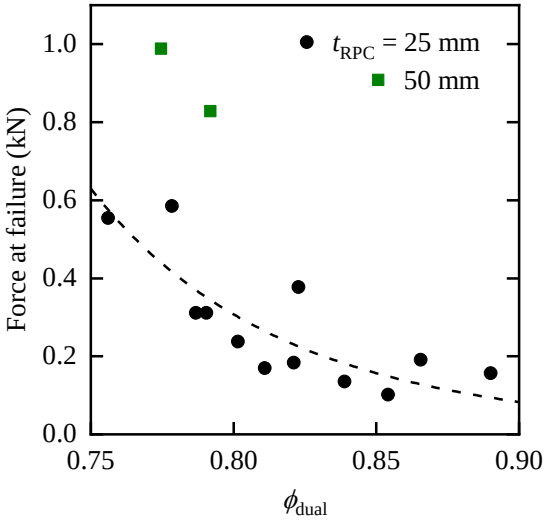

Figure 2.12. Force at failure measured with three-point bend testing as a function of the dual-scale porosity ϕ_{dual} of various RPC bricks with thickness t_{RPC} of 25 mm and 50 mm. The dashed line is a power function fit of the measurements with t_{RPC} = 25 mm, showing a clear trend of increasing force at failure with decreasing porosity.

Visual observations – Photographs of RPC bricks after testing in the solar reactor are shown in **Figure 2.13**. **(a)** and **(b)** are photographs of a brick from RPC cavity #2. Within the indication bars is a crack that formed due to mechanical stresses during cycling. The formation of such cracks was found to be inevitable to some extent, but can be minimized by using stronger RPC bricks. Most importantly,

the self-supporting structure of an RPC cavity needs to be optimized such that it can withstand the formation of such cracks without collapsing.

Figure 2.13 (c) shows a brick from cavity #3 that delaminated into two separate parts at the interface originating from the layering of two polyurethane foams during the manufacturing process. Although such delamination did not lead to a collapse of the cavity, it is detrimental to its structural integrity and represents a drawback of the fabrication method of thicker, double-layered RPCs. No indication of decreased stability due to the third-scale porosity partially incorporated into cavity #3 was found.

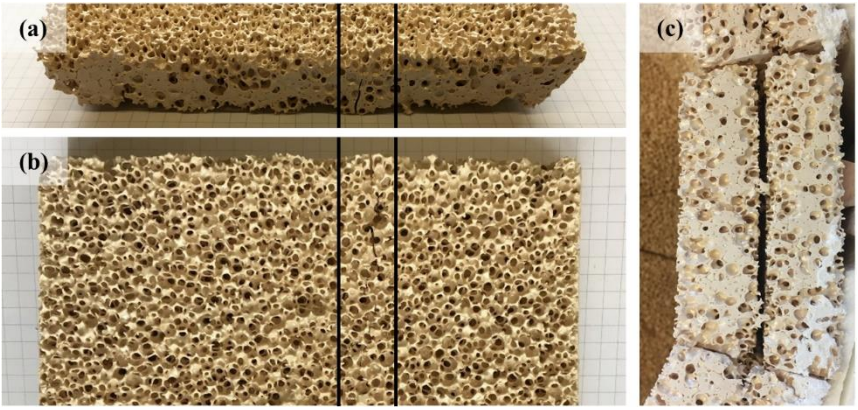

Figure 2.13. Photographs of RPC bricks after testing in the solar reactor. **(a)** and **(b)** show the side and tow view of a brick from RPC cavity #2 with a crack that formed within the indication bars. **(c)** shows the side view of a brick from cavity #3 which delaminated into two parts.

From comparing the two different cavity geometries tested, it was concluded that assembling the side of the cavity out of thirteen bricks as in RPC cavity #3 is beneficial compared to the octagonal design of cavities #1 and #2. A low number of side parts results in a sharp contact angle and decreases the likelihood of a part to slip out of its position, but increases the width of a single part and the load due to bending. Conversely, using many side parts reduces the risk of failure in bending, but the number of parts is limited to ensure a sufficient contact angle, and an optimum was found to be somewhere in the low two-digit range.

Based on the results from the present chapter, the following conclusions were drawn on the design of RPC cavities:

- There is a trade-off between mechanical strength and cycling performance of a ceria RPC cavity. A general trend between low porosity and high thickness of the RPC, both resulting in higher mass loading, and increasing mechanical strength was observed. On the other hand, after exceeding a certain limit, adding more mass without ensuring effective volumetric absorption of the solar radiation and uniform heating of the ceria does not result in an improved reactor performance.
- Adding a third scale of porosity to the RPC was shown to be possible and could help to ensure more uniform heating of the ceria, but it complicates the fabrication process and a performance increase can only be expected if the structure is thoroughly optimized, for example with a numerical model.
- Manufacturing thicker RPC bricks by stacking two polyurethane foams on top of each other was shown to be feasible, but should be avoided due to possible delamination of the two layers during cycling in the solar reactor.
- Assembling the side rings of the cavity out of more than eight single bricks is beneficial for stability, with an optimum somewhere in the low two-digit number of bricks.

2.3 Summary and conclusions

The design of a scaled-up ceria RPC solar reactor for pressure and temperature swing thermochemical redox cycling was presented. The performance of the solar reactor for CO_2 splitting was experimentally assessed in a high-flux solar simulator. Three different ceria cavities made of an interlocking structure of RPC bricks with different porosities, thicknesses, and geometries were designed and tested. The results indicate that lower porosity and higher thickness, both resulting in a higher ceria mass loading, are generally beneficial for the mechanical integrity of the RPC cavity, but the addition of mass without ensuring effective volumetric absorption of the solar radiation and uniform heating of the ceria does not increase the reactor performance. A maximum solar-to-fuel energy conversion efficiency of $\eta_{\text{solar-to-fuel}} = 3.48 \pm 0.08\%$ was measured at the limited maximum power of $P_{\text{solar}} = 32.2$ kW, but the direct comparison of cycles at different power levels revealed a trend of increasing efficiency with increasing P_{solar}. This trend highlights the great potential for performance increase when the solar reactor is operated at its design point of $P_{\text{solar}} = 50$ kW in the solar tower in Spain. An extended experiment with five consecutive CO_2 splitting cycles revealed stable operation over multiple cycles without observable degradation.

3 Heat transfer modelling of the solar reactor[1]

To analyze the performance of the previously presented solar reactor and to gain insight into improved design and operational conditions, a transient heat transfer model of the solar reactor was developed and implemented in ANSYS CFX, which is presented in this chapter. The numerical model couples the incoming concentrated solar radiation using Monte Carlo ray tracing, incorporates the reduction chemistry by assuming thermodynamic equilibrium, and accounts for internal radiation heat transfer inside the porous ceria by applying effective heat transfer properties. The model was experimentally validated using data acquired in a high-flux solar simulator, where temperature evolution and oxygen production results from model and experiment agreed well. The numerical results indicate the prominent influence of solar radiative input power, where increasing it substantially reduces reduction time of the ceria structure. Consequently, the model predicts a solar-to-fuel energy conversion efficiency of >6% at a solar radiative power input of 50 kW; efficiency >10% can be obtained provided the RPC macroporosity is substantially increased and better volumetric absorption and uniform heating is achieved. Managing the ceria surface temperature during reduction to avoid sublimation remains a critical challenge for direct absorption solar receiver-reactors.

[1] Material in this chapter has been published in S. Zoller, E. Koepf, P. Roos, and A. Steinfeld, "Heat transfer model of a 50 kW solar receiver-reactor for thermochemical redox cycling using cerium dioxide," *Journal of Solar Energy Engineering*, 2019, 141 (2), 021014-021014-11.

3.1 Solar reactor configuration and experimental setup

The solar reactor was introduced in section 2.1 of the previous chapter. The reactor parts relevant for modelling are schematically shown in **Figure 3.1** and are briefly summarized here.

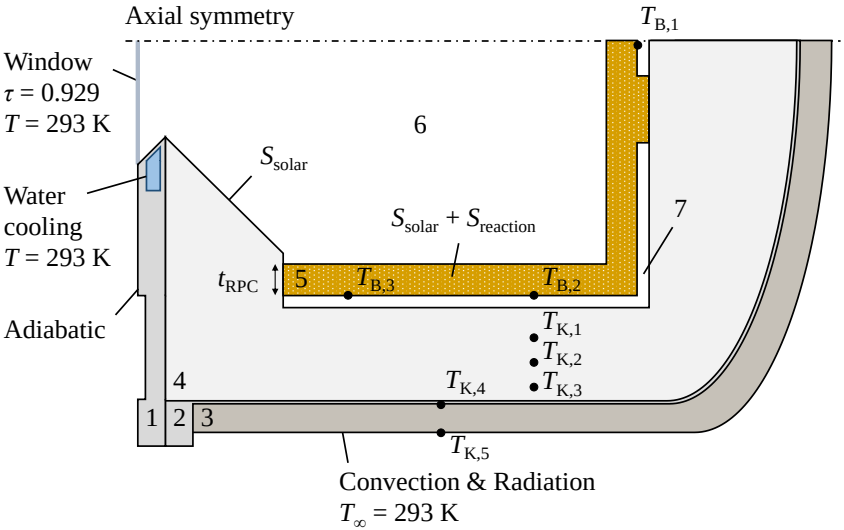

Figure 3.1. Schematic of the solar reactor configuration relevant to the modelling domains: (1) aluminum front, (2) steel shell, (3) insulating jacket, (4) Al_2O_3–SiO_2 insulation, (5) ceria RPC with thickness t_{RPC}, (6) receiver cavity, (7) fluid region behind RPC. Also indicated are the boundary conditions and source terms for the heat transfer model, and the transmissivity τ of the quartz window. The measurement locations of the type-B and type-K thermocouples are indicated: $T_{B,1}$–$T_{B,3}$ are located at the outer surface of the ceria RPC; $T_{K,1}$–$T_{K,3}$ are located at different depths within the insulation; $T_{K,4}$ and $T_{K,5}$ are located at the outer surfaces of the reactor shell and the insulating jacket, respectively.

The solar reactor has a water-cooled aluminum front (region 1) with a circular aperture of 16 cm diameter through which concentrated solar radiation enters. The aperture is sealed with a 12 mm thick circular quartz window that has a diameter of 300 mm. The aluminum front is attached to the reactor shell (region 2), which is made out of stainless steel (316L). The outside of the shell is insulated with a jacket (region 3) made from woven glass fibers and filled with

ceramic mat board. The inside of the reactor is insulated with KVS184/400 (Rath, Inc.), which is primarily comprised of 80% Al_2O_3 and 20% SiO_2 (region 4). The reaction cavity (region 6) is assembled with an interlocking structure of ceria RPC bricks (region 5). The ceria bricks have a thickness denoted t_{RPC}. Between the RPC and the Al_2O_3−SiO_2 insulation, there is a 10 mm gap (region 7) which facilitates gas flow through the reaction cavity.

The experimental setup (**Figure 2.6**) and procedure was described in detail in section 2.1.3 of the previous chapter. The positions of the temperature measurements are indicated in **Figure 3.1**. $T_{B,1}$−$T_{B,3}$ denote the measurement positions of B-type thermocouples at the back surface of the RPC. The nominal RPC temperature $T_{RPC,nom}$ is defined as the average of these three temperature measurements. The temperature of the lateral Al_2O_3−SiO_2 insulation ($T_{K,1}$−$T_{K,3}$) as well as the outer lateral surfaces of the reactor shell ($T_{K,4}$) and the insulating jacket ($T_{K,4}$) were measured with K-type thermocouples.

3.2 Heat transfer analysis

The solar receiver-reactor, which features inherent axial symmetry, was simulated using a two-dimensional axisymmetric heat transfer model implemented in the commercial CFD software ANSYS CFX (release 17.0). The aluminum front, steel shell, insulating jacket and Al_2O_3−SiO_2 insulation are modelled as solid domains. The cavity and the open region behind the RPC are modelled as fluid domains that are non-participating in radiation. During the reduction step the fluid is assumed to be stationary, as previous modelling results have shown that the contribution of convection to heat transfer is negligible, especially while operating under vacuum [88]. The ceria RPC is modelled as a homogeneous and radiatively participating porous media.

3.2.1 Governing equations

As the fluid domains are assumed to be stationary, the system governing equations are reduced to only the energy conservation equation. For the fluid and the solid domains, the energy conservation equation is

$$\frac{\partial}{\partial t}(\rho h) = \nabla \cdot (k \nabla T) \tag{3.1}$$

where ρ is the density, h is the enthalpy, and k is the thermal conductivity. The energy conservation equation for the solid phase of the porous RPC domain is

$$\frac{\partial}{\partial t}((1-\phi_{\text{dual}})\rho h) = \nabla \cdot \left(k_{\text{eff}} \nabla T\right) + S_{\text{solar}} + S_{\text{reaction}} + Q_{\text{sf}} \tag{3.2}$$

where ϕ_{dual} is the dual-scale porosity of the RPC, k_{eff} is its effective thermal conductivity, S_{solar} is the source term accounting for the absorbed incoming solar radiation from the HFSS, and S_{reaction} is the energy sink accounting for the endothermic reduction of ceria. The conservation equations for solid and fluid phases are coupled by the source term $Q_{\text{sf}} = -Q_{\text{fs}} = h_{\text{fs}} \cdot A_{\text{fs}}(T_{\text{f}} - T_{\text{s}})$, where h_{fs} is the interfacial heat transfer coefficient, A_{fs} is the fluid-solid area density, and T_{s} and T_{f} are the temperatures of the solid and the fluid, respectively. An artificially high h_{fs} of 10'000 W m^{-1} K^{-1} enforces thermal equilibrium between the two phases ($T_{\text{s}} = T_{\text{f}}$). This is reasonable due to the assumption of the fluid being stationary. According to the correlation described in reference [107], A_{fs} is set to 951.8 m^{-1}.

For the fluid phase of the RPC domain, the energy conservation equation is given by

$$\frac{\partial}{\partial t}(\phi_{\text{dual}} \rho h) = \nabla \cdot (k \nabla T) + S_{\text{radiation}} + Q_{\text{fs}} \tag{3.3}$$

where $S_{\text{radiation}}$ is the source term accounting for radiation exchange. Due to a constraint in ANSYS CFX that only allows radiative heat transfer in the fluid and not in the solid phase of porous domains, the radiative properties of the fluid are set to the effective radiative properties of the RPC; local thermal equilibrium between the fluid and the solid phase is enforced. The radiative transfer equation for the RPC, modelled as an isotropic, gray, absorbing-emitting-scattering participating media, is

$$\frac{dI(\bar{r},\bar{s})}{ds} = -\beta I(\bar{r},\bar{s}) + \alpha I_{\text{b}}(\bar{r}) + \frac{\sigma}{4\pi}\int_{4\pi} I(\bar{r},\bar{s}')d\omega' \tag{3.4}$$

where $\bar{r}$ is the position vector, $\bar{s}$ is the direction vector, s is the path length, β, α and σ are the extinction, absorption and scattering coefficients, respectively, I is the radiation intensity, I_{b} is the blackbody radiation intensity depending on the

local temperature, and ω is the solid angle. For the geometric optics regime, $\alpha = \beta \cdot (1-r)$ and $\sigma = \beta \cdot r$, where r is the reflectivity of CeO_2. The radiation exchange source term in equation (3.3) is calculated as

$$S_{\text{radiation}} = \alpha \left(4\pi I_{\text{b}} - \int_{4\pi} I d\omega \right) \tag{3.5}$$

which accounts for emission and absorption inside the porous RPC structure.

3.2.2 Boundary conditions and source terms

The boundary conditions and source terms are schematically indicated in **Figure 3.1**. At the outer surface of the insulating jacket, the exposed surface of the reactor shell not covered by the jacket, and the lateral surface of the aluminum front, energy is lost by radiative and convective heat transfer. The convective heat transfer coefficient is conservatively assumed to be 15 W m^{-1} K^{-1}. Due to moderate surface temperatures, the temperature distribution within the solar reactor is insensitive to the value of heat transfer coefficient taken on these surfaces. The ambient air temperature, water cooling channel temperature, and the quartz window temperature are all assumed to be at 293 K. The front surface of the aluminum front of the reactor is assumed to be adiabatic. The mean transmissivity of the 12 mm thick quartz window was experimentally measured to be τ = 0.929. Flux maps were acquired by a calibrated CCD camera viewing a Lambertian target while it was irradiated with the HFSS. The 300 mm diameter quartz window was placed in front of the target such that it could intercept the entire light cone produced by the HFSS. By comparing flux maps taken with and without the window intercepting the radiation, the mean transmissivity, thereby averaged over all incident angles of the radiation, could be extracted. The volumetric and surface heat sources S_{solar} within the RPC and on the front insulation surface were derived using a decoupled Monte Carlo (MC) ray tracing model. This model yields the absorbed radiative power delivered by the HFSS. For the calculation of the nonstoichiometry δ of ceria, thermodynamic equilibrium is assumed, as previous experimental work with similar ceria RPCs has shown that the reduction step is heat transfer limited [50]. The oxygen partial pressure is assumed to be constant at p_{O_2} = 5 mbar due to operation under

vacuum. The energy sink S_{reaction}, accounting for the endothermic reduction reaction, is calculated using the two expressions for equilibrium δ [63] and reaction enthalpy ΔH_{O_2} [88], listed in **Table 3.1**.

3.2.3 Material properties

Material properties of the ceria RPC with dual-scale porosity are listed in **Table 3.1**. The dual-scale porosity of the RPC was calculated by measuring its mass and volume. The strut porosity was assessed with a combination of mercury intrusion porosimetry (Quantachrome Poremaster 60-GT) and geometric approximations to calculate the size of the hollow struts. The value for the number of pores per inch was provided by the manufacturer of the polyurethane foams used to manufacture the RPCs. The effective heat and mass transfer properties of the RPC structure were taken from literature. The correlation for the total hemispherical reflectance of CeO_2 was evaluated for an average reduction state of $\delta = 0.035$ and depends on the local temperature in the heat transfer model. To calculate the heat source S_{solar} using the MC ray tracing model, a correlation weighted according to Planck's law for blackbody temperatures of 5780 K, which is a good approximation of solar radiation, was used, resulting in $r = 0.2905$ [109]. For the calculation of the effective thermal conductivity of the RPC, thermal conductivity of the fluid was set to zero, due to operation under vacuum.

The heat transfer properties of the solid domains are listed in **Table 3.2**. They were either taken from literature, or values from the manufacturers were used. For the specific heat capacity of the Al_2O_3–SiO_2 insulation, a mass-weighted average of alumina and silica heat capacities was calculated according to the chemical composition, as suggested in reference [110]. Fluid domain properties were taken as a modified inert gas for simplicity, as the domain has negligible contribution to heat transfer.

Table 3.1. Morphological and effective heat transfer properties of the ceria RPC.

Variable	Correlation	Unit	Ref.
Dual-scale porosity	$\phi_{\text{dual}} = 0.78$		
Strut porosity	$\phi_{\text{strut}} = 0.3561$		
Single-scale porosity	$\phi_{\text{single}} = \frac{\phi_{\text{dual}} - \phi_{\text{strut}}}{1 - \phi_{\text{strut}}} = 0.6583$		
Number of pores per inch	$n_{\text{ppi}} = 10$		
Mean pore diameter	$d_{\text{m}} = \left(5.302 \cdot 10^{-5} \cdot \phi_{\text{single}} + 2.155 \cdot 10^{-5}\right) \cdot \frac{357}{n_{\text{ppi}}} = 2.015 \cdot 10^{-3}$	m	[107]
Extinction coefficient	$\beta = \frac{-630.674 \cdot \phi_{\text{single}}^2 - 120.06 \cdot \phi_{\text{single}} + 1229.36}{1000 \cdot d_{\text{m}}} = 435.15$	m^{-1}	[107]
Total hemispherical reflectance (at δ = 0.035)	$r = 0.41184 - 2.419 \cdot 10^{-5} \cdot T$		[109]
Density CeO_2	$\rho_{\text{CeO}_2} = 7220$	kg m^{-3}	[65]
Molar mass	$M_{\text{CeO}_2} = 0.1721$	kg mol^{-1}	[111]
Specific heat capacity	$c_{\text{p,CeO}_2} = \frac{67.95 - 9.9 \cdot 10^5 \cdot T^{-2} + 0.0125 \cdot T}{M_{\text{CeO}_2}}$	$\text{J kg}^{-1}\ \text{K}^{-1}$	[112]
Thermal conductivity CeO_2	$k_{\text{CeO}_2} = -1.723 \cdot 10^{-9} \cdot T^3 + 1.12 \cdot 10^{-5} \cdot T^2 - 0.024 \cdot T + 17.8$	$\text{W m}^{-1}\ \text{K}^{-1}$	[113]
Effective thermal conductivity	$k_{\text{eff}} = k_{\text{CeO}_2} \cdot (1 - 0.6223 \cdot \phi_{\text{dual}}) \cdot (1 - 1.055 \cdot \phi_{\text{dual}})$	$\text{W m}^{-1}\ \text{K}^{-1}$	[114]
Equilibrium thermodynamics (T in °C)	$\delta = 10^{-(2.15 \cdot 10^{-6} \cdot T^2 - 9.88 \cdot 10^{-3} \cdot T + 12.2)} \cdot \left(\frac{p_{\text{O}_2}}{p_0}\right)^{1.25 \cdot 10^{-7} \cdot T^2 - 3.1 \cdot 10^{-4} \cdot T - 1.83 \cdot 10^{-2}}$		[107]
Reaction enthalpy	$\Delta H_{\text{O}_2} = 969.409 - 503.739 \cdot \delta^{0.5}$	kJ mol^{-1}	[88]

Table 3.2. Material properties of the reactor components.

Variable	Correlation	Unit	Ref.
Al_2O_3-SiO_2 insulation (Rath, Inc. KVS184/400)			
Density	$\rho_{ins} = 400$	kg m^{-3}	[115]
Specific heat capacity	$c_{p,ins} = -3.09 \cdot 10^{-10} \cdot T^4 + 1.71 \cdot 10^{-6} \cdot T^3 - 3.48 \cdot 10^{-3} \cdot T^2 + 3.18 \cdot T + 101$	J kg^{-1} K^{-1}	[116, 117]
Thermal conductivity	$k_{ins} = -2.09 \cdot 10^{-11} \cdot T^3 + 1.06 \cdot 10^{-7} \cdot T^2 + 3.69 \cdot 10^{-5} \cdot T + 7.07 \cdot 10^{-2}$	W m^{-1} K^{-1}	[115]
Hemispherical total emittance	$\varepsilon_{ins} = 0.28$		[118]
Stainless steel 316L shell			
Density	$\rho_{shell} = 8000$	kg m^{-3}	[119]
Specific heat capacity	$c_{p,shell} = 412 + 0.2 \cdot T - 2 \cdot 10^{-5} \cdot T^2$	J kg^{-1} K^{-1}	[120]
Thermal conductivity	$k_{shell} = 0.013 \cdot T + 11.45$	W m^{-1} K^{-1}	[119]
Hemispherical total emittance	$\varepsilon_{shell} = 0.57$		[121]
Insulating jacket			
Density	$\rho_{jacket} = 80$	kg m^{-3}	[122]
Specific heat capacity	$c_{p,jacket} = 840$	J kg^{-1} K^{-1}	[122]
Thermal conductivity	$k_{jacket} = 5.319 \cdot 10^{-7} \cdot T^2 - 2.487 \cdot 10^{-4} \cdot T + 6.433 \cdot 10^{-2}$	W m^{-1} K^{-1}	[122]
Hemispherical total emittance	$\varepsilon_{jacket} = 0.89$		[123]
Aluminum front			
Density	$\rho_{Al} = 2700$	kg m^{-3}	[124]
Specific heat capacity	$c_{p,Al} = 706.7 + 0.6 \cdot T - 1 \cdot 10^{-4} \cdot T^2$	J kg^{-1} K^{-1}	[120, 125]
Thermal conductivity	$k_{Al} = -4.01 \cdot 10^{-10} \cdot T^4 + 1.14 \cdot 10^{-6} \cdot T^3 - 1.22 \cdot 10^{-3} \cdot T^2 + 0.53 \cdot T + 162$	W m^{-1} K^{-1}	[110, 126]
Hemispherical total emittance	$\varepsilon_{Al} = 0.09$		[121]

3.2.4 Initial condition

To establish the initial condition, the solar reactor was heated from room temperature for one hour with a radiative power input, evaluated at the reactor window, of P_{solar} = 10 kW. Subsequently, P_{solar} was set to zero, and the reactor was allowed to cool naturally to the desired start temperature. The temperature field established with the preheating simulation was then applied as an initial condition for the transient reduction simulation and all subsequent analysis. It was confirmed experimentally that the initial condition is accurate, and further established that small variations in the initial condition (temperature field) do not have a significant influence on the final temperature field after reduction.

3.2.5 Numerical solution

The heat sources S_{solar} were calculated by applying an in-house MC ray tracing code [127] with 10^9 rays. The heat transfer simulations were performed with ANSYS CFX (version 17.0). To discretize the governing equations in space, between 35’115 and 54’980 hexahedral cell elements were used. Due to a limitation in ANSYS CFX, a single cell had to be extruded in the third direction around the symmetry axis. For the discretization in time, a constant time step of 1 s was used. The finite volume method was applied with a second-order backward Euler scheme. To solve the radiative transfer equation (equation (3.4)), the discrete transfer model was used, transforming the equation into a set of transport equations for I and solving for discrete solid angles along s. The simulations were performed using the high-performance cluster Euler of ETH Zurich.

3.3 Experimental validation

The heat transfer model was validated by comparing the calculated temperature and oxygen evolution to the experimentally determined values measured during testing of the solar reactor in the HFSS. RPC cavity #1 (see **Table 2.1** for specifications) was simulated at a radiative solar power input of P_{solar} = 30.5 kW. The corresponding experimental values are summarized in **Table 2.2** in section 2.2 of the previous chapter[1]. **Figure 3.2 (a)** shows the numerically calculated (solid lines) and the experimentally measured (dashed lines) temperatures at the different thermocouple positions as indicated in **Figure 3.1**. The agreement between simulation and experiment is reasonably good for all thermocouple positions, most importantly the B-type thermocouples in contact with the back of the RPC (standard deviation between experimental and numerical $T_{RPC,nom}$ during reduction was 9.4 °C). For both the simulation and the experiment, the RPC temperature at the front position ($T_{B,3}$) is significantly lower than the temperatures towards the back of the RPC ($T_{B,1}$ and $T_{B,2}$). The temperature of the Al_2O_3−SiO_2 insulation at the innermost position ($T_{K,1}$) is slightly overestimated in the simulation. This is because the thermal conductivity of the porous insulation is assumed constant, whereas in reality it changes between the reduction step, which is operated under vacuum, and the oxidation step, which is operated at atmospheric pressure. Temperatures of the reactor shell ($T_{K,4}$) and the insulating jacket ($T_{K,5}$) are slightly underestimated in the simulation, due to a lower initial condition for the external surfaces, however, the curvature still matches experimental results. In **Figure 3.2 (b)**, $T_{RPC,nom}$ and the O_2 release rate are shown for the simulation (solid lines) and the experiment (dashed lines). The two curves for $T_{RPC,nom}$ match well, with the maximum temperature being 1470 °C for the simulation and 1489 °C for the experiment. The O_2 release at low temperatures is slightly overestimated in the simulation, however, the integrated value of 31.1 L matches well with the experimentally measured integrated amount of 30.1±0.6 L (4% difference).

[1] Due to the two-dimensional axisymmetric solar reactor model, the nominal RPC temperature $T_{RPC,nom}$ is defined in this chapter as the average of three measurement points, compared to four measurement points in chapter 2. As a result, the values reported here for $T_{RPC,nom}$ differ slightly from the corresponding values reported in the previous chapter.

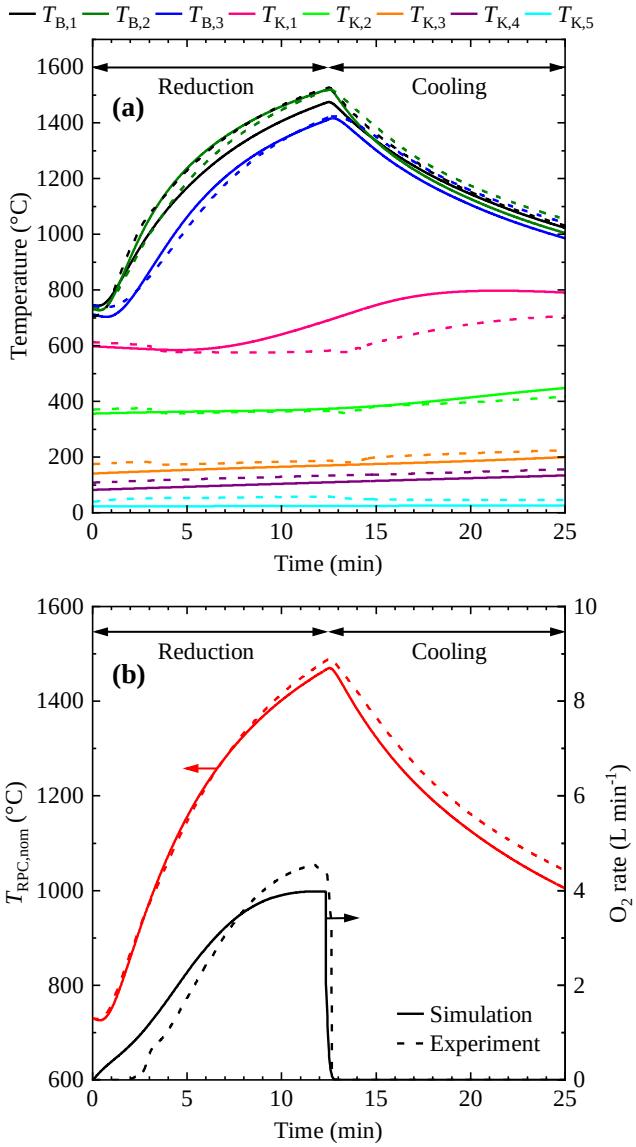

Figure 3.2. (a) Numerically calculated (solid lines) and experimentally measured (dashed lines) temperatures at the locations indicated in **Figure 3.1**, during the reduction step and the subsequent natural cooling phase. **(b)** Average of the three thermocouple locations measuring the temperature of the RPC at the back surface ($T_{RPC,nom}$) and O_2 evolution as a function of time.

The solar-to-fuel energy conversion efficiency is defined as

$$\eta_{\text{solar-to-fuel}} = \frac{Q_{\text{fuel}}}{Q_{\text{solar}} + Q_{\text{pump}} + Q_{\text{inert}}} \tag{3.6}$$

Because the oxidation reaction is not included in the solar reactor model, but complete re-oxidation using CO_2 is assumed, the energy content of the fuel (CO) produced is calculated as $Q_{\text{fuel}} = \Delta H_{\text{fuel}} \cdot 2\int r_{O_2}\, dt$, where ΔH_{fuel} is the heating value of CO (ΔH_{CO} = 283 kJ mol^{-1}) and $\int r_{O_2}\, dt$ is the rate of released O_2 integrated over the reduction step. Q_{solar} is the total solar energy input integrated over the reduction step. Q_{pump} and Q_{inert} are the energy penalties associated with vacuum pumping and the consumption of the inert gas Ar during the reduction step, respectively, and are calculated as suggested in reference [53] and described in section 2.1.4 of the previous chapter. An efficiency of $\eta_{\text{solar-to-fuel}}$ = 3.38% was predicted by the simulation, which is comparable to the experimentally determined efficiency $\eta_{\text{solar-to-fuel}}$ = 3.26±0.07%. Heat recovery was not applied. The slight overestimation is correlated directly to the slight overestimation in total O_2 yield from the simulation.

3.4 Modelling results and discussion

The validated numerical model is a useful tool not only to better understand the performance of the current solar reactor, but also to assess the influence of various design and operational changes on the performance of the reactor. In the subsequent analysis, a base case simulation representing the experimental validation case (as described in section 3.3) is used to perform a parametric study of several crucial design variables of the ceria RPC. The critical parameters of the base case simulation are summarized in **Table 3.3**.

3.4.1 Incident solar radiation and temperature distribution

A contour plot of absorbed incoming solar radiation from the HFSS, S_{solar}, is shown in **Figure 3.3 (a)**. S_{solar} is constant during the reduction step. Due to the relatively large optical thickness of the RPC ($\tau_{\text{RPC}} = \beta \cdot t_{\text{RPC}} = 10.9$), more than 90% of the incoming radiation is absorbed within the first five millimeters of the RPC structure, which can clearly be seen in the figure. Due to the uneven

distribution of the incoming solar radiation, caused by the discrete nature of the HFSS radiation source, S_{solar} is high towards the back corner of the RPC structure and relatively low at the center of the back. **Figure 3.3 (b)** shows the temperature distribution within the solid and the RPC domain of the reactor at the end of the reduction step, and of the RPC domain only (enlarged). The hottest regions in the temperature profile within the RPC correspond to the areas of highest S_{solar}; the front, directly irradiated surface of the RPC reaches the highest temperatures, while the back of the RPC and areas which are less directly irradiated remain at lower temperatures. This non-uniformity of temperature within the RPC limits the efficiency that can be achieved with the solar reactor, as the nonstoichiometry δ (a measure of oxygen released during reduction) is directly correlated to the ceria temperature which is achieved. To achieve a more uniform temperature distribution using highly concentrated sunlight, and do so quickly enough to reach a high solar-to-fuel energy conversion efficiency, the macroporosity (millimeter-scale) of the absorber material (in this case an RPC) must be substantially increased.

Table 3.3. RPC and operational parameters of the base case simulation. These values correspond to the parameters of the validation experiment.

Variable	Value	Unit
RPC morphology		
Dual-scale porosity	$\phi_{dual} = 0.78$	
Number of pores per inch	$n_{ppi} = 10$	
Extinction coefficient	$\beta = 435.15$	m^{-1}
Thickness of RPC	$t_{RPC} = 25$	mm
Ceria mass loading	$m_{RPC} = 18.38$	kg
Operational parameters		
Solar radiative power input	$P_{solar} = 30.5$	kW
Partial pressure of oxygen	$p_{O_2} = 5$	mbar
Reduction start temperature	$T_{red,start} = 730$	°C
Reduction end temperature	$T_{red,end} = 1466$	°C

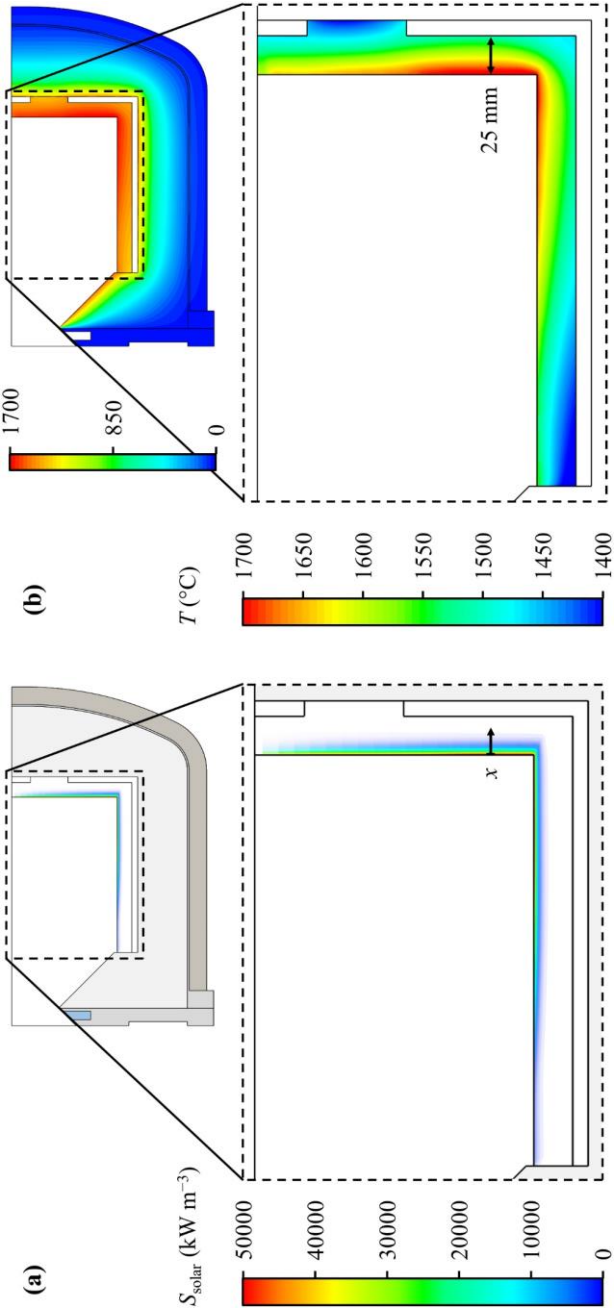

Figure 3.3. (a) Distribution of S_{solar} within the ceria RPC during the reduction step. **(b)** Temperature distribution of the solid domains, and of the RPC domain (also enlarged) at the end of the reduction step. Also indicated is the variable *x*, which defines the cross-section position through the RPC for the evaluation of absorbed solar radiation and temperature (analyzed in **Figure 3.8**).

3.4.2 Energy flows

The instantaneous energy balance for the reduction step is illustrated as a function of time in **Figure 3.4** for the base case at P_{solar} = 30.5 kW. Note that heat recovery was not applied. Losses by reradiation from the hot cavity, the change in sensible heat content of the RPC, the remaining reactor components (Al_2O_3–SiO_2 insulation, aluminum front, reactor shell, and insulating jacket), the energy consumed by the endothermic reduction reaction, the conductive heat loss to the water-cooled reactor front, and other heat losses are indicated. Other heat losses include reflection of incoming solar radiation inside the reactor cavity and at the quartz window, absorption of incoming radiation at the window, and convection and radiation at the outer reactor surfaces. Initially, sensible heating of the RPC dominates energy consumption, consuming 87% of P_{solar}, while on average it consumes 33%. By the end of the reduction step, reradiation dominates heat loss, accounting for 31% of P_{solar} on average and 45% at the peak. Reradiation losses could be lowered by decreasing the size of the aperture, provided that solar radiation can be delivered with higher concentration. A selective coating with high transmissivity in the visible region of the solar spectrum, but high reflectivity in the IR region of the radiation emitted by the hot cavity, could be considered for the quartz window, provided that the coating can withstand very high temperatures (>500 °C). Reradiation losses also decrease with increasing power input P_{solar} because the ceria remains at high temperatures for less time when the reduction duration shortens. Sensible heating of the bulk materials consumes 21% of P_{solar} on average, but levels off early in the reduction cycle, with the Al_2O_3–SiO_2 insulation being the dominant consumer, while the aluminum front, reactor shell, and insulating jacket consume 1.2% or less each. Energy loss through sensible heating of the bulk materials could be lowered if insulation materials with lower specific heat capacity were used. The energy fraction driving the endothermic reduction reaction of ceria quickly increases with time, and on average accounts for 5.6% of P_{solar}. The conduction heat losses to the water-cooled reactor front are significant, with an average consumption of 2.7% of P_{solar}. The losses by convection and radiation at the outer reactor surfaces, as well as the energy lost by reflection of the incoming solar radiation inside the reactor cavity, account for less than 0.3% of P_{solar} each. The remaining

7.1% of P_{solar} is lost by absorption and reflection at the quartz window ($\tau = 0.929$). Although not considered in the simulation, convective losses associated with gasses exiting the solar reactor during the reduction step are also negligible (less than 0.3% of the input power). The share of energy used to drive the reduction reaction, and therefore also representative of the solar-to-fuel energy conversion efficiency, could potentially be increased by using doped ceria to increase the reduction extent [55, 56], or by minimizing the temperature swing with near isothermal operation [79, 128, 129], although this does not necessarily increase the efficiency due to other limitations introduced with a lower temperature swing.

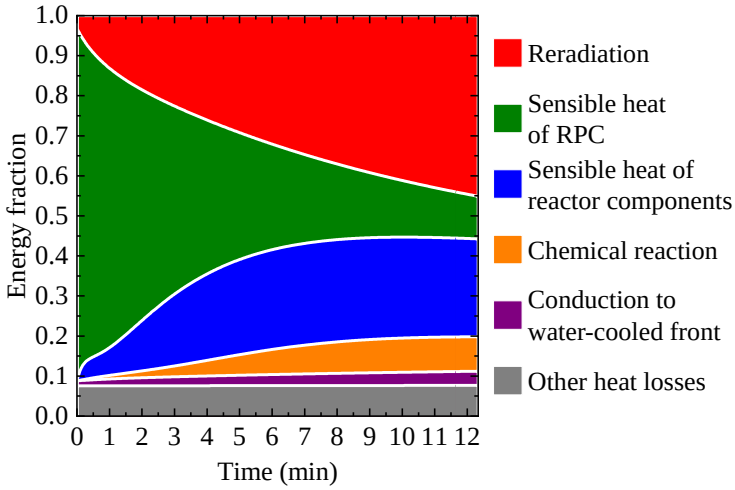

Figure 3.4. Instantaneous energy balance for the duration of a reduction step. Other heat losses include convection and radiation at the outer reactor surfaces, reflection of incoming solar radiation inside the reactor cavity, and absorption and reflection at the quartz window.

3.4.3 Parameter study

Operational and design parameters of the solar reactor can be optimized using the numerical model. The most critical parameters are the level of input power and the structure of the ceria RPC. These two parameters are coupled, as higher power is only beneficial if it can be more uniformly absorbed within the RPC

structure. If solar radiation is only absorbed within the first small fraction of RPC depth, performance becomes limited by the maximum sustainable surface temperature of the ceria RPC. A parametric study was conducted using the parameters listed in **Table 3.3** as the base case. The following parameters were varied in the study: RPC thickness t_{RPC}, RPC dual-scale porosity ϕ_{dual}, and the radiative power input P_{solar}. All of the simulations were initialized with $T_{RPC,nom}$ = 730 °C, and the duration of the reduction step t_{red} was controlled by setting P_{solar} to zero once $T_{RPC,nom}$ = 1466 °C was reached. The results of the parameter study are shown in **Figure 3.5**−**Figure 3.7**. For each case, the nominal RPC temperature $T_{RPC,nom}$ and the oxygen release rate are plotted as a function of time in **(a)**. In **(b)**, the variable parameters are plotted versus $\eta_{solar\text{-}to\text{-}fuel}$, t_{red}, the reduction time required to reach $T_{RPC,nom}$ = 1466 °C, and $T_{RPC,max}$, the maximum temperature of the RPC reached at the end of the reduction step, which is a critical value for the mechanical stability of the RPCs.

RPC thickness t_{RPC} – The effect of changing RPC thickness t_{RPC} is shown in **Figure 3.5**. The inner, directly irradiated surface area of the RPC as well as the thickness of the separating gap between the RPC and the Al_2O_3–SiO_2 insulation were kept constant, while the thickness of the insulation was adapted slightly (and with negligible effect). For both higher and lower t_{RPC} values compared to the base case, $\eta_{solar\text{-}to\text{-}fuel}$ slightly decreases, while t_{red} increases with increasing RPC thickness. This is due to the increasing ceria mass loading of the reactor, and consequently longer duration of the reduction step, which yields a higher total amount of O_2 released. This can be seen in **Figure 3.5 (a)**. Due to the increased thickness of the RPC, $T_{RPC,max}$ increases as the end of the reduction step is controlled by the temperature at the back surface of the RPC. It is important to note the scale of the efficiency metric, which shows that large variation in the RPC thickness parameter, while yielding a trend, only impacts the efficiency by a fraction of a percent.

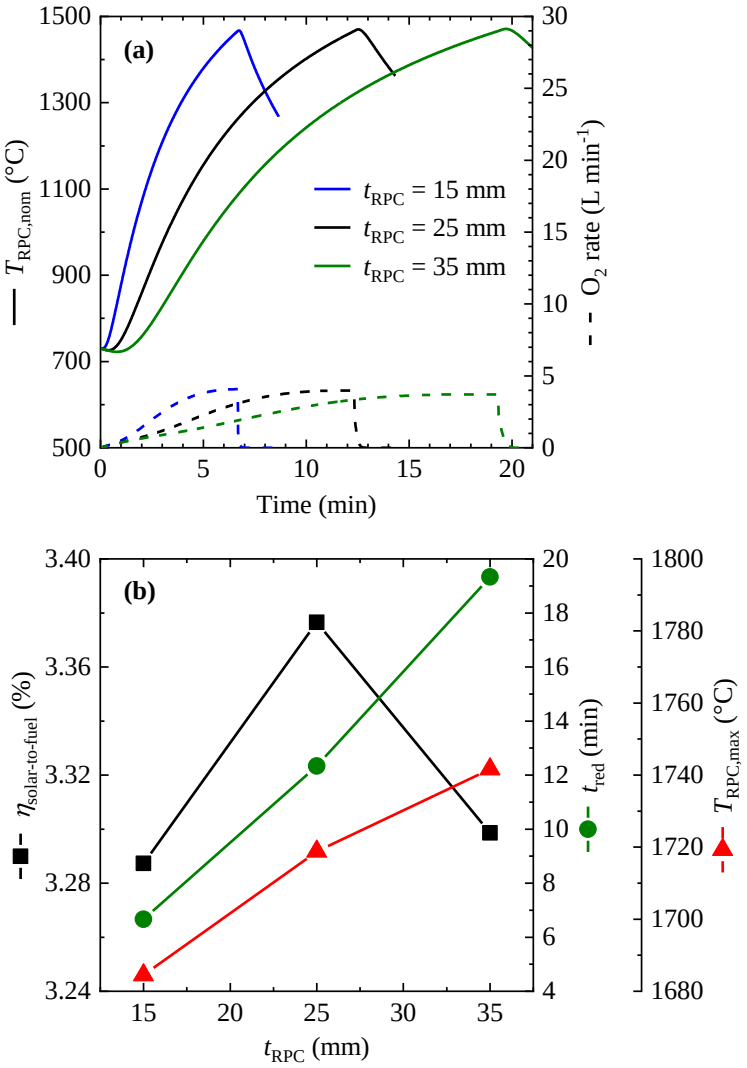

Figure 3.5. (a) Nominal RPC temperature $T_{RPC,nom}$ and O_2 release rate as a function of time for varying RPC thickness t_{RPC}. **(b)** Efficiency $\eta_{solar\text{-}to\text{-}fuel}$, reduction time t_{red} and maximum RPC temperature $T_{RPC,max}$ of these cycles as a function of t_{RPC}.

RPC porosity ϕ_{dual} – The effect of changing RPC porosity ϕ_{dual} is illustrated in **Figure 3.6**. The only variable adjusted is ϕ_{dual}, while ϕ_{single} and n_{ppi} are kept constant. The chosen values of ϕ_{dual} correspond to a change in ceria mass loading of ±25% compared to the base case. $\eta_{solar\text{-}to\text{-}fuel}$ decreases slightly from 3.54% at ϕ_{dual} = 0.725 to 3.14% at ϕ_{dual} = 0.835. The influence on t_{red} is higher, with a decrease from 16.1 min (ϕ_{dual} = 0.725) to 9.15 min (ϕ_{dual} = 0.835), mainly caused by the significant difference in ceria mass loading. Similar to the impact of changing RPC thickness, the effect of decreasing reduction time is counteracted by a decrease in total O_2 released, and therefore the efficiency only changes slightly. With increasing ϕ_{dual}, the optical thickness of the RPC decreases, leading to a slightly lower $T_{RPC,max}$.

Solar radiative power input P_{solar} – The most influential variable is the solar radiative power input, as can be seen in **Figure 3.7**. Increasing P_{solar} drastically decreases t_{red} and increases the efficiency $\eta_{solar\text{-}to\text{-}fuel}$. Roughly doubling P_{solar} from 30.5 kW to 60 kW cuts t_{red} by more than half (12.3 min to 5.0 min) and more than doubles $\eta_{solar\text{-}to\text{-}fuel}$ (from 3.38% to 7.34%). This is attributed primarily to two phenomena: first, heat losses, especially by reradiation, decrease due to a shorter reduction time, and second, higher RPC temperatures towards the irradiated front surface directly lead to higher oxygen nonstoichiometry δ. $T_{RPC,max}$ increases from 1719 °C at P_{solar} = 30.5 kW to 1914 °C at P_{solar} = 60 kW.

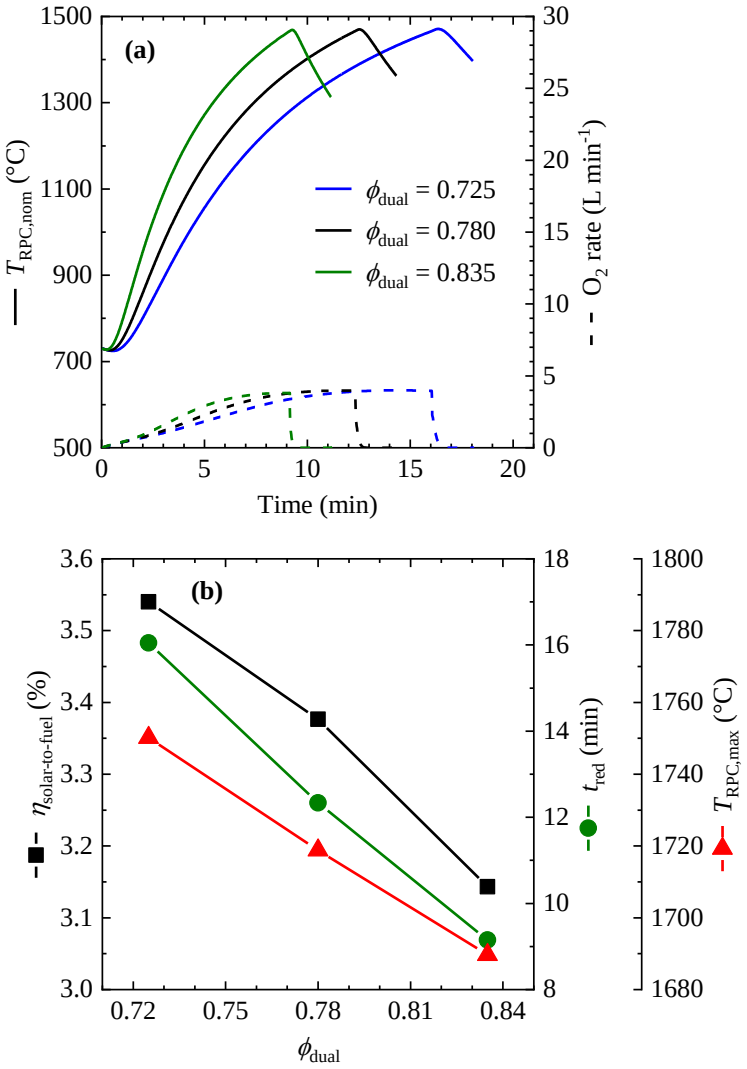

Figure 3.6. (a) Nominal RPC temperature $T_{RPC,nom}$ and O_2 release rate as a function of time for varying RPC porosity ϕ_{dual}. **(b)** Efficiency $\eta_{solar\text{-}to\text{-}fuel}$, reduction time t_{red} and maximum RPC temperature $T_{RPC,max}$ of these cycles as a function of ϕ_{dual}.

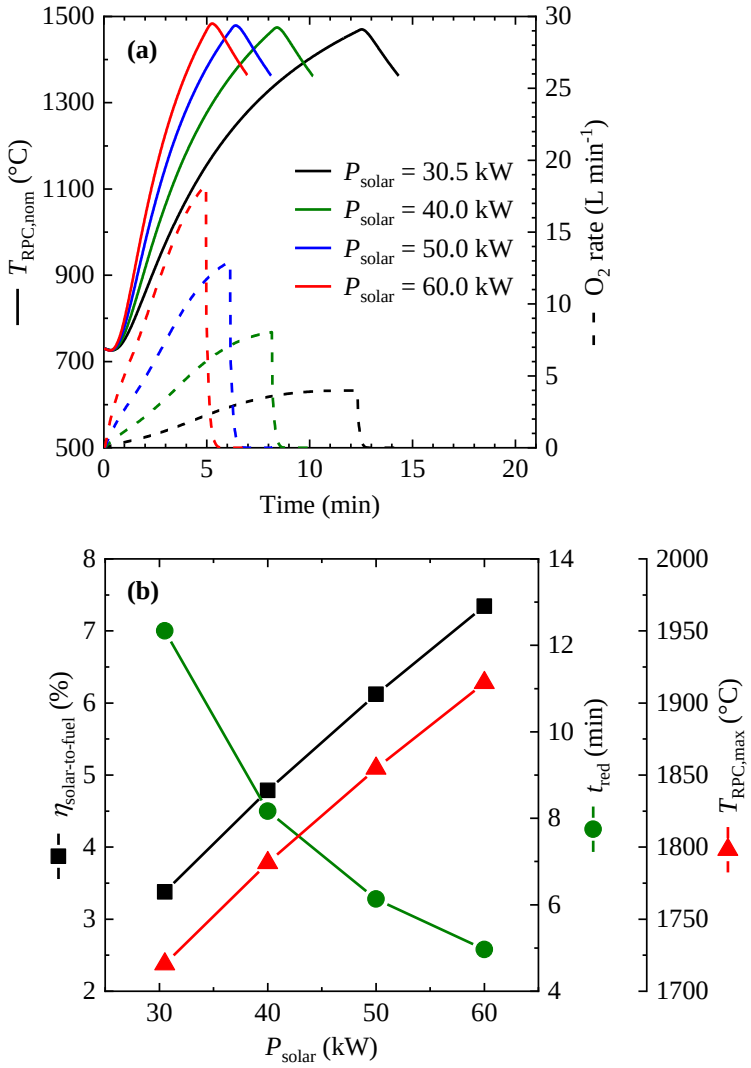

Figure 3.7. (a) Nominal RPC temperature $T_{RPC,nom}$ and O_2 release rate as a function of time for varying input power P_{solar}. **(b)** Efficiency $\eta_{solar\text{-}to\text{-}fuel}$, reduction time t_{red} and maximum RPC temperature $T_{RPC,max}$ of these cycles as a function of P_{solar}.

3.4.4 Advanced reactor design

An additional case was considered to assess the possibility of designing a solar receiver-reactor with parameters optimized beyond the current means of production. This advanced reactor design features much larger pores (n_{ppi} = 3; average macropore diameter ≅ 7 mm) to dramatically enhance volumetric absorption, but the same porosity and thereby mass loading as in the base case. In **Figure 3.8 (a)**, the absorbed solar radiation S_{solar} as well as the local RPC temperature are shown as a function of the penetration depth for the advanced RPC design. The location of extraction of these variables is indicated in **Figure 3.3**. For comparison, the results for the case with n_{ppi} = 10 (average macropore diameter ≅ 2 mm) are also shown. In both cases, P_{solar} was set to 60 kW and the values correspond to a simulation time of 298 s, which is the time when the reduction step ends in the case of n_{ppi} = 10. In the case of n_{ppi} = 3, S_{solar} is more uniformly distributed, leading to a more uniform distribution of temperature within the RPC. The temperature difference between the front and the back of the RPC equals 113 °C, compared to 377 °C for n_{ppi} = 10. The more uniform distribution of temperature within the RPC directly results in higher performance of the solar reactor when it is properly operated. Due to the lower temperature difference between the front and the back of the RPC, t_{red} can be extended without exceeding the critical value for the maximum RPC temperature. This is illustrated in **Figure 3.8 (b)**, which shows the nominal RPC temperature and the rate of released oxygen as a function of time for n_{ppi} = 3 (solid lines) and for n_{ppi} = 10 (dashed lines). For n_{ppi} = 3, t_{red} is extended to 423 s. Due to the more uniform temperature distribution, this results in the same critical value of $T_{RPC,max}$ = 1914 °C at the end of the reduction step as in the case of n_{ppi} = 10. As a consequence, the total amount of O_2 released drastically increases from 53.55 L (n_{ppi} = 10) to 106.5 L (n_{ppi} = 3), which ultimately results in a better performance of the solar reactor ($\eta_{solar\text{-}to\text{-}fuel}$ = 10.2% compared to $\eta_{solar\text{-}to\text{-}fuel}$ = 7.34% for n_{ppi} = 10). However, the path to realizing a ceria structure with the physical parameters required to obtain this level of performance is ongoing research and development [95, 96]. Note that this analysis does not consider heat recovery.

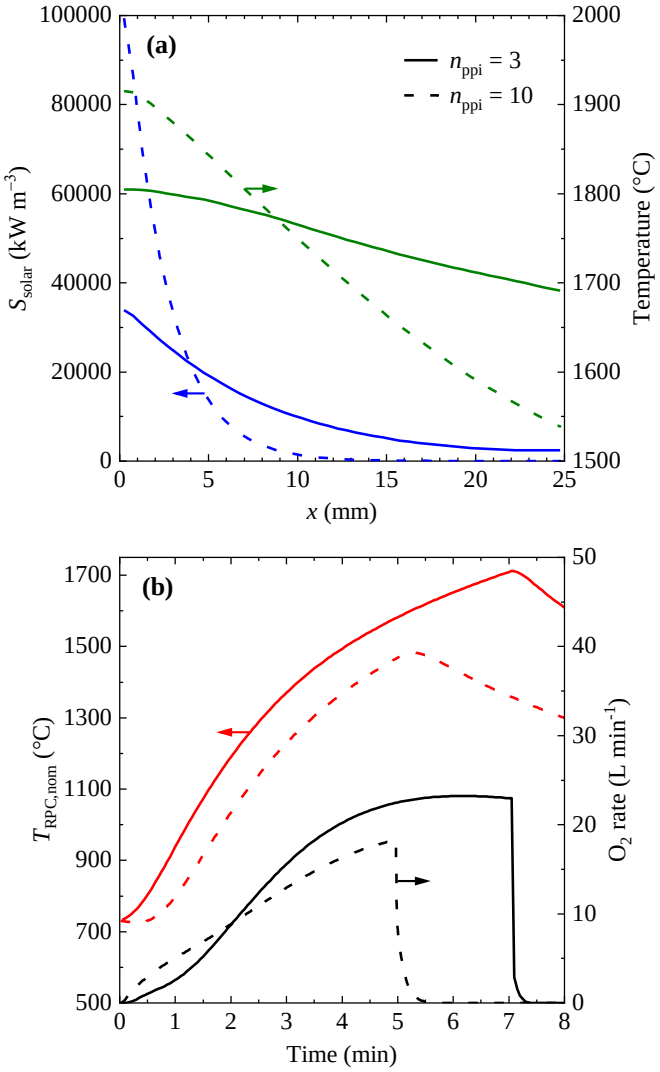

Figure 3.8. (a) Absorbed solar radiation S_{solar} and RPC temperature as a function of x, the depth within the RPC, where zero indicates the front, directly irradiated surface. The position of evaluation within the RPC is indicated in **Figure 3.3**. Values are extracted for a simulation time of 298 s, corresponding to t_{red} of the case with n_{ppi} = 10. **(b)** Nominal RPC temperature $T_{RPC,nom}$ and rate of released O_2 as a function of time. Solid lines represent the advanced RPC design with n_{ppi} = 3 and dashed lines represent the case with n_{ppi} = 10. For both cases, P_{solar} was set to 60 kW.

It is important to consider the impact of volumetric absorption and uniform heating when analyzing and scaling solar reactors. With typical chemical reactors, for example continuously stirred thermal reactors, scaling up results in significantly increased thermal performance because of the increased ratio of active volume to external surface area [130]. For solar RPC reactor technology, however, this is not the case because the active volume is limited to the ceria RPC. The solar reactor analyzed in this study is more than 12 times larger than its precursor technology, where an efficiency of 5.25% was experimentally demonstrated [53], and yet an efficiency of only 6.12% is predicted here for the nominal 50 kW case and otherwise similar operating conditions. This is directly due to a decreasing active volume fraction which results from scaling an RPC solar reactor; at the 4 kW scale, the ceria RPC represented 60% of the chemical reactor volume, while at the 50 kW scale it is only 30%. Assuming a constant apparent mass density inside the ceria RPC, the total mass loading of the reactor is limited in the same way. In 2012 Furler et al. [50] determined that ceria RPCs outperformed ceria blocks and felts because of the structure's relatively enhanced radiation heat transfer properties, although direct absorption of solar radiation was still limited. In the present study, it became clear that for solar reactors of this type to operate efficiently, increased utilization of the cavity volume by achieving higher volumetric absorption of the incoming solar radiation, and thus volumetric heating, is necessary.

The impact that sensible heat recovery could have on the performance of a solar reactor is evident from the energy balance presented in **Figure 3.4**. Previous studies have considered various forms of heat recovery and the implication on both reactor and system level efficiency [83, 89, 100, 128]. For the reactor technology discussed here, consisting of stationary redox ceramics which are directly irradiated in temperature and pressure swing operation, heat recovery options are limited. The possibility to actively recover heat during the cooling step after reduction exists, but its impact is limited by the need to utilize an inert gas heat transfer fluid for multiple stages of solid-gas heat exchange [91].

A simple energy balance analysis can be performed to determine the impact of extracting heat from the stationary ceria mass between the reduction and

oxidation steps and providing it back to the solar reactor. Considering the case of 50 kW of solar input power for the base RPC parameters listed in **Table 3.3** (total ceria mass of 18.4 kg covering 30% of the reactor volume), a solar-to-fuel energy conversion efficiency of 6.12% was determined. 7,813 kJ of energy is contained as sensible heat in the ceria solid (42% of the solar energy input during the reduction step). For the purpose of discussing the potential of minimizing this irreversibility, 100% of this sensible heat is considered to be recoverable. Accounting for this recoverable heat as a subtraction from the denominator of equation (3.6), presumably representing the fact that less solar energy would be required to heat the solid, and further accounting for less energy lost by reradiation because of the resulting shorter reduction time (212 s versus 368 s), an efficiency of $\eta_{\text{solar-to-fuel}} = 12.75\%$ is determined. It is important to note that removing and reusing even 50% of the sensible heat contained in the ceria RPC represents a major engineering challenge.

3.5 Summary and conclusions

The development and use of an experimentally validated transient heat transfer model of the ceria RPC solar reactor designed for pressure and temperature swing thermochemical redox cycling has been reported. The performance of the solar reactor was analyzed using the model by considering, among other metrics, the solar-to-fuel energy conversion efficiency. The numerical results indicate the prominent influence of solar radiative input power, and therefore the solar concentration ratio at the aperture, where increasing power substantially reduces reduction time. For P_{solar} = 50 kW, the model predicts $\eta_{solar\text{-}to\text{-}fuel}$ = 6.12%. For this case, if 100% of the sensible heat is recovered from the ceria RPC mass between reduction and oxidation steps, the cycle efficiency can be increased to 12.75%. Further measures to boost $\eta_{solar\text{-}to\text{-}fuel}$ include increasing the millimeter-scale porosity of the RPC structure to allow for more volumetric absorption of incoming solar radiation, resulting in a more uniform temperature distribution within the RPC, which ultimately improves the performance of the solar reactor. For example, an increase in macropore diameter from roughly 2 mm to 7 mm (n_{ppi} 10 to 3) resulted in an increase of $\eta_{solar\text{-}to\text{-}fuel}$ from 7.34% to 10.2%. If volumetric absorption and uniform heating is achieved inside the ceria RPC, mass loading could also be increased to obtain higher efficiencies, provided the latter criteria of uniform heating is not compromised in the process. While the numerical model indicates the potential of this solar receiver-reactor technology to achieve high efficiency, critical issues remain: (i) stable ceria structures with optimized volumetric absorption characteristics (i.e., ordered structures) must be fabricated and demonstrated to survive in the solar reactor environment, and (ii) with increased power, the directly irradiated surface area of the redox active material will always be at risk of sublimation; the search for new redox active materials which can be reduced at lower temperatures while maintaining favorable oxidation properties is critically important [56, 57, 131].

4 On-sun demonstration of CO_2 and H_2O splitting[1]

In this chapter, the experimental facility for on-sun testing of the solar reactor is described and experimental results for CO_2 and H_2O splitting are presented. The experimental facility features three main subsystems: a high-flux solar concentrating heliostat field and tower, the solar thermochemical reactor system including a dedicated power measurement system, and a gas-to-liquid conversion plant to process the syngas produced in the solar reactor to liquid hydrocarbon fuels on-site via Fischer-Tropsch synthesis. The solar reactor contains a ceria RPC cavity that is optimized for the operation in the solar tower. It features an adapted geometry designed to prevent structural failure when the reactor is in operation in the solar tower, tilted by 40 degrees towards the heliostat field, and adjusted RPC properties for maximum performance.

With the adapted solar reactor, a maximum solar-to-fuel energy conversion efficiency of 5.6±1.0% is experimentally demonstrated for CO_2 splitting. For the co-splitting of H_2O and CO_2, different possibilities to control the composition of the produced syngas are presented. With operating conditions that result in a syngas composition suitable for Fischer-Tropsch processing, 62 consecutive redox cycles are performed with the same ceria RPC cavity. The produced syngas is collected and stored to further process it on-site to liquid hydrocarbon fuels.

[1] Material in this chapter has partially been extracted from D. Nizamian, "On-sun commissioning of a 50 kW solar reactor for thermochemical H_2O & CO_2 splitting," Master Thesis, ETH Zurich, 2019, and from M. Stephan, "Experimental assessment of a 50 kW solar reactor for thermochemical splitting of H_2O and CO_2," Master Thesis, ETH Zurich, 2019, both supervised by S. Zoller.

4.1 Experimental setup and methods

4.1.1 Solar reactor design

The solar reactor design was described in detail in section 2.1.1. For the operation in the solar tower in Spain, a few specifications had to be adjusted. The reactor configuration installed in the solar tower is schematically shown in **Figure 4.1**. Adjustments include integrated air nozzles for convective cooling of the quartz window, an optimized design of the reactor front and a radiation shield for enhanced cooling, and an optimized design of the ceria RPC cavity.

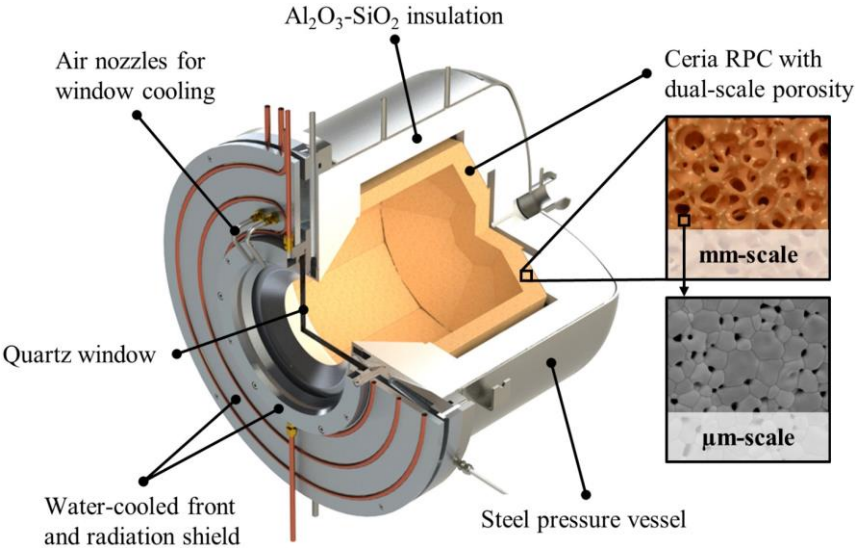

Figure 4.1. Schematic of the solar reactor installed in the solar tower in Spain. It is a directly irradiated cavity receiver-reactor containing a ceria RPC structure with dual-scale porosity. The detachable insulating jacket covering the outside of the steel shell is not shown here.

The four nozzles that guide compressed air onto the outer surface of the quartz window had to be integrated into the radiation shield of the solar reactor due to the limited space available in the solar tower, especially because of the movable flux measurement target that can be positioned directly in front of the reactor as described in section 4.1.3. A mounting structure for the quartz window with enhanced water cooling and an additional water-cooled radiation shield had to

be installed because the amount of spilled radiation that hits the reactor front but does not enter through the reactor's aperture is much higher in the solar tower compared to the solar simulator.

Ceria RPC cavity – Two main conclusions about the design of a ceria RPC cavity were drawn from the experimental testing of the solar reactor in the high-flux solar simulator (chapter 2) and the numerical heat transfer model of the reactor (chapter 3):

- Increasing the mass loading of ceria in the reactor by means of increasing thickness or decreasing porosity of the RPC, both increasing its optical thickness, generally increases the mechanical strength and durability of the RPC, but does not result in increased reactor performance without effective volumetric absorption of the solar radiation and uniform heating of the ceria.
- More volumetric absorption of solar radiation can be accomplished by increasing the size of the millimeter-scale pores of the RPC. If at the same time the thickness of the struts of the RPC is increased to keep the porosity constant, the same mass of ceria can be heated more uniformly, resulting in a performance increase.

Based on these findings, a new RPC cavity was designed with larger millimeter-scale pores (n_{ppi} = 7 compared to the previously used n_{ppi} = 10) and a thickness t_{RPC} = 35 mm. Even larger pores are supposed to be beneficial, but cannot be fabricated with the current manufacturing method because this is the limit of porosity of the polyurethane foams used in the manufacturing process. A thickness of 35 mm was chosen as a tradeoff between cycling performance and mechanical stability. The manufacturing process for the RPCs was described in detail in section 2.1.2. It was slightly adapted by increasing the sintering duration and temperature to eight hours at 1700 °C (from one hour at 1600 °C), which was shown to increase the mechanical strength of the RPCs significantly [132].

Compared to the operation with the high-flux solar simulator where the solar reactor was horizontally facing the radiation source, in the solar tower the reactor is tilted downwards to the heliostat field with an inclination angle of around

40 degrees. To prevent structural failure in this orientation, a new design for the back of the ceria RPC cavity was developed. The dome-shaped back design, shown in **Figure 4.2 (a)**, consists of eight wedge-shaped pieces that are inclined by 30 degrees compared to a flat back plane, and one central octagonal piece with chamfered edges. At the down-facing operating angle, this design keeps all the back pieces in compression against each other, just as the interlocking rings of side bricks hold each other in compression. The side of the RPC cavity consists of two rings of 16 RPC bricks each. **Figure 4.2 (b)** is a photograph of the back RPC pieces during installation when the reactor was positioned upright, showing the inclination of the wedge-shaped back pieces and the contact angle between a wedge-shaped piece and the central back piece. The channels cut into the back Al_2O_3−SiO_2 insulation to minimize contact between RPC and insulation and to facilitate gas flow exiting the reactor are also visible. The total ceria mass of all RPC bricks forming the cavity varied between 17.8 and 21.3 kg because RPCs were replaced during the course of experiments.

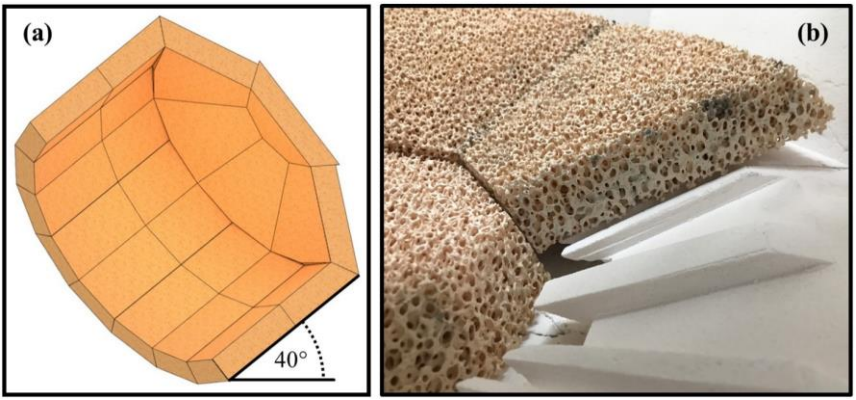

Figure 4.2. Detail view of the ceria RPC cavity with the dome-shaped back designed to prevent structural failure when the reactor is in operation in the solar tower, tilted by 40 degrees towards the heliostat field. **(a)** is a section view of the RPC cavity in its operational position as designed with CAD, while **(b)** is a photograph showing two wedge-shaped back pieces and the central octagonal back piece during installation in upright position.

4.1.2 Solar concentrating facility

An overview of the entire experimental facility located in Móstoles, Spain, is shown in **Figure 4.3** [133]. The heliostat field was designed by IMDEA Energy Institute [134]. It consists of 169 heliostats with an area of 3 m^2 each, resulting in around 500 m^2 of total reflective area. All heliostats are curved with a focal length of 25 m for the first eight rows of heliostats closest to the solar tower and 30 m for the remaining six rows of heliostats. While conventional heliostats for electricity generation via concentrated solar power (CSP) usually are flat, curved heliostats are necessary to reach the higher concentration ratio needed to efficiently drive the solar thermochemical ceria cycle. This modular, high-flux heliostat field is able to meet the nominal operating condition of the solar reactor of 50 kW delivered into the 16 cm diameter reactor aperture, corresponding to a concentration of around 2500 kW m^{-2}.

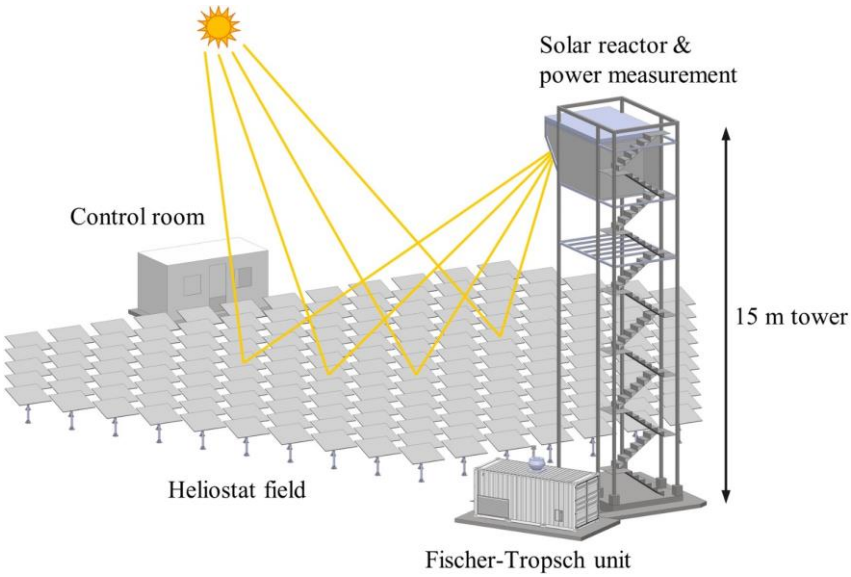

Figure 4.3. Schematic of the experimental facility installed in Móstoles, Spain. Up to 169 heliostats with an area of 3 m^2 each concentrate sunlight onto a solar tower with an optical height of 15 m. Installed in the experimental level of the tower are the solar reactor and the power measurement system. The syngas produced in the solar reactor can be stored and processed to liquid hydrocarbon fuels on-site using the Fischer-Tropsch unit. All systems are centrally operated from the control room.

The solar reactor is placed on top of the solar tower with an optical height of 15 m, together with a power measurement system and peripheral components, described in detail in the following sections 4.1.3 and 4.1.4, respectively. The solar reactor is facing north and is tilted downwards by around 40 degrees in the direction of the heliostat field's optical axis. On the ground next to the solar tower sits the Fischer-Tropsch unit, developed by HyGear in the Netherlands. It includes a buffer tank to store the syngas produced in the solar reactor, and can be used to produce liquid hydrocarbon fuels on-site. The experimental components, including the heliostat field, the solar reactor and the power measurement setup, are centrally operated from the control room located behind the heliostat field.

4.1.3 Power measurement system and methodology

In contrast to a solar simulator, the power delivered by the heliostat field cannot be held perfectly constant and varies in connection with many factors such as the direct normal irradiance (DNI) of the sun, the time of the year and the time of the day. Therefore, a more sophisticated power measurement system is necessary to estimate the power entering the solar reactor during the course of an experiment. **Figure 4.4 (a)** shows the arrangement of the solar reactor and the power measurement system in the solar tower [133]. Two different devices to measure power were installed: a water calorimeter and an optical flux measurement acquisition system (FMAS). The water calorimeter, developed by ETH Zurich, is mounted inside the same type of steel vessel as the solar reactor. The two vessels are placed 1.6 m apart, with the solar reactor installed west of the water calorimeter. Outside the circular, water-cooled fronts of reactor and calorimeter, porous Al_2O_3 insulation material is installed as a passive thermal shield to block radiation from entering into the experimental level of the solar tower during operation. The FMAS was developed by DLR in Germany [135]. It consists of a water-cooled, Al_2O_3 plasma-coated Lambertian target mounted on a linear belt which allows alignment with either receiver vessel for measurement, and a CCD camera with a telephoto lens mounted in the control room. In either of the two measurement positions, the center of the FMAS target is aligned with the optical axis of the heliostat field and the center of the respective receiver aperture, at a

distance of approximately 20 cm from the aperture plane. Before taking a measurement with the FMAS, it is automatically calibrated with a Gardon-type flux gauge embedded in the center left edge of the target. The power is calculated by integrating the compiled flux map over a circular area with a diameter of 16 cm, corresponding to the area of the apertures. If not in use for a measurement, the target is in standby position between the two receivers.

The details of the water calorimeter are shown in **Figure 4.4 (b)**. It is designed to closely approximate the specifications of the solar reactor. The outer shell and the front section, including the cooling shield and the cavity aperture, are identical to the ones used for the solar reactor. The cavity of the calorimeter consists of aluminum front and back plates, and approximately 20 meters of coiled copper tubing, all coated with a black high-emissivity enamel. The cavity is thermally separated from the front, and the volume between the inner cavity and the outer shell is filled with rock wool insulation to minimize heat losses. Cold water enters to the hollow front plate and flows through the cooper tubing and internal channeling of the back plate, where it exits the calorimeter. The water flow rate is measured with a highly accurate electromagnetic flow meter (Endress+Hauser, Promag 33), and inlet and outlet temperatures of the water are recorded with four-wire Pt100 resistance thermometers. Using the measured temperature difference between inlet and outlet and the flow rate of water, the solar power entering the aperture can be calculated directly. Losses by reflection, emission, conduction and convection together were estimated to account for less than 1% of the incoming solar radiation at a power input of 50 kW, and the accuracy of a calorimeter measurement was specified as ±2%. Due to the calorimeter's high accuracy and the additional error of an FMAS measurement imposed by the location of the Lambertian target slightly off the aperture plane, calorimeter measurements were directly used to assess the power entering the solar reactor. However, FMAS measurements were used to estimate the additional error introduced by the different locations of the calorimeter and the solar reactor.

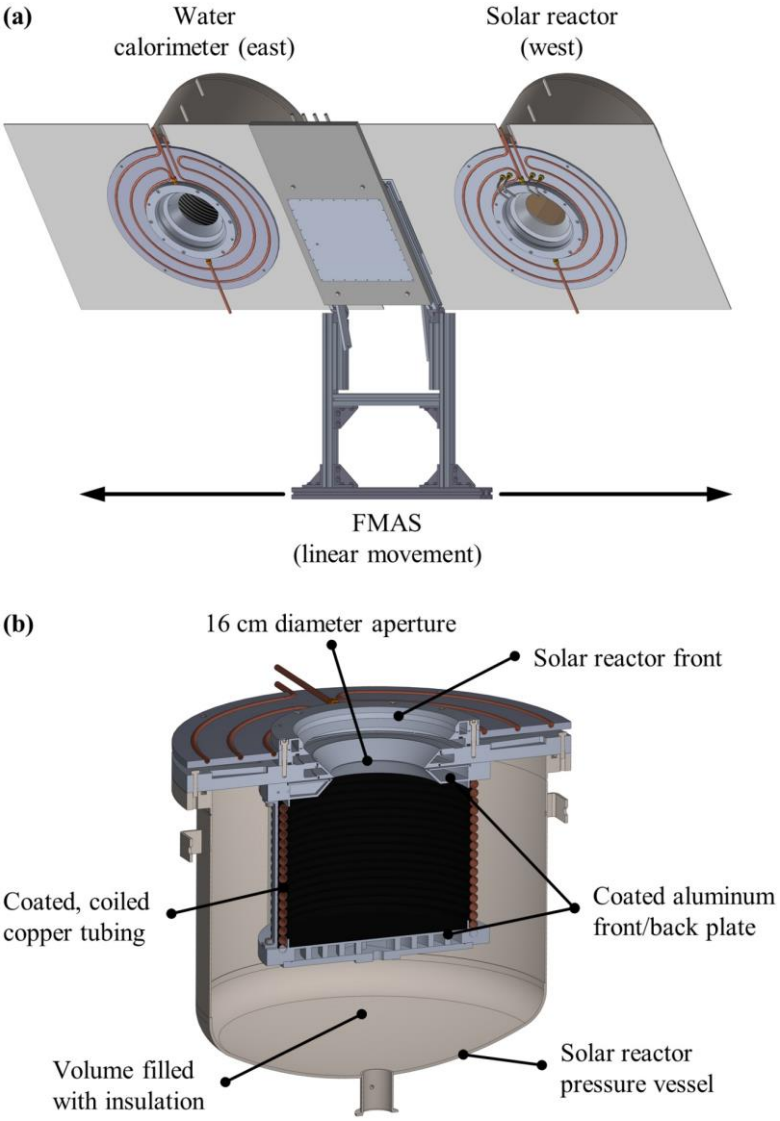

Figure 4.4. (a) Detail view of the solar reactor and power measurement installation in the solar tower. The Lambertian target of the flux measurement acquisition system (FMAS) moves on a linear system, which allows alignment with either receiver vessel for measurement. The vessel at the east position contains a water calorimeter, and the west position receiver contains the solar reactor. **(b)** Cross section of the water calorimeter installed in the east receiver vessel, with indication of its main components.

The procedure to calculate the solar radiative power entering the reactor, P_{solar}, during a typical reduction cycle is shown in **Figure 4.5**. It shows the nominal RPC temperature in the solar reactor in red and the power measurements in black for both the water calorimeter and the FMAS positioned in front of the calorimeter and the reactor. Before a reduction step starts, the heliostats track from a nearby standby position to the calorimeter aperture position with the FMAS target positioned in front. Within less than 30 s, all heliostats move to the new aim position, and a first FMAS measurement is taken. The FMAS target then moves to its standby position, and the solar radiation enters the calorimeter. The calorimeter takes less than 180 s to approach a thermal steady state due to its low thermal mass, high thermal conductivity, and thin metallic walls between the cavity surface and the water channels. Once a steady measurement reading is recorded, the FMAS target is positioned in front of the solar reactor and the heliostat's aim point is changed to the reactor aperture. Another FMAS measurement is taken, and when the target moves back to the standby position, full power enters the reactor's aperture. When the reduction end temperature is reached, the measurement process is reversed. The FMAS target moves in front of the reactor, thereby interrupting power delivery to the solar reactor. An FMAS measurement is taken, followed by a calorimeter measurement and a second FMAS measurement at the calorimeter position. The steady calorimeter readings before and after the reduction step, 39.9 and 41.3 kW in the present case, are assumed to be equal to P_{solar} at the beginning and the end of the reduction. The variation of delivered power mainly originates from tracking errors changing with time, and the DNI is assumed constant during the short reduction period of typically less than 15 min. This is justified because experiments were usually stopped when clouds appeared. Therefore, a linear change of P_{solar} was assumed during reduction, and the grey area in **Figure 4.5** corresponds to the total solar energy input to the reactor integrated over the reduction step, Q_{solar}. The difference between calorimeter and FMAS readings has two main reasons. First, the measurement plane of the FMAS is approximately 20 cm in front of the aperture plane, and second, additional power enters the reactor and the calorimeter by means of rays reflected on the conical aperture surface. However, because only the relative difference between FMAS measurements at the reactor

and the calorimeter positions are used to evaluate the inaccuracy imposed by measuring the power entering the reactor at the position of the calorimeter, these errors cancel out.

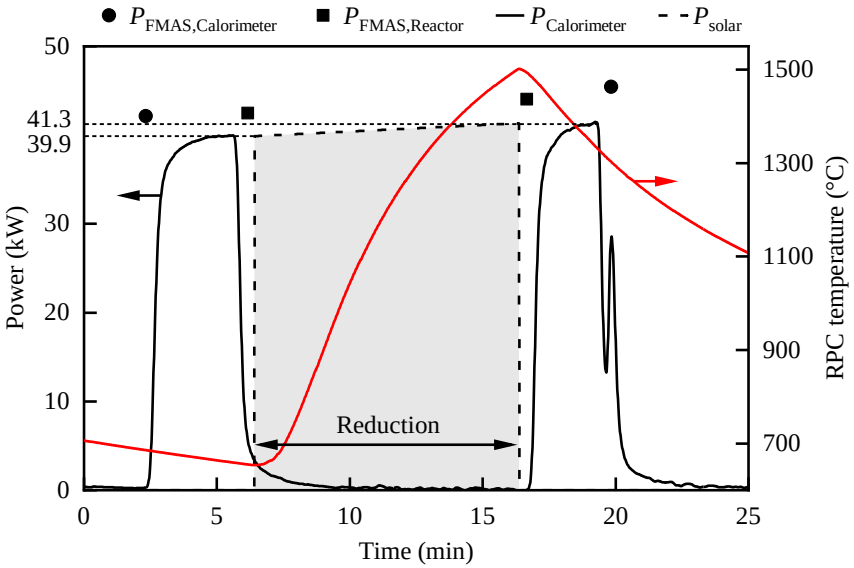

Figure 4.5. Representative measurement cycle to deduce the solar radiative power at the aperture of the solar reactor, P_{solar}. The nominal RPC temperature in the solar reactor is shown in red, along with power measurements with the water calorimeter and the FMAS in front of the calorimeter and the solar reactor in black. P_{solar} is assumed to change linearly between steady calorimeter readings recorded before and after reduction, while the relative difference between FMAS measurements at the two positions is used to assess the inaccuracy imposed by measuring the power entering the reactor at the position of the calorimeter.

4.1.4 Reactor periphery and experimental procedure

The experimental setup installed in the solar tower is similar to the setup described in chapter 2.1.3 for experiments with the high-flux solar simulator. However, some adjustments were necessary, especially for the handling of water. The setup installed in the tower is schematically illustrated in **Figure 4.6** and shown in **Figure 4.7**, which is a photograph of the experimental level of the tower with indication of the major subsystems. Gas flow rates of Ar and CO_2 were

regulated using electronic mass flow controllers (Bronkhorst, EL-FLOW Select) and entered the reactor through tangential inlet ports behind the quartz window to form a vortex flow that protects the window from the deposition of particles. Liquid water was fed with a stepper motor driven positive displacement pump into an electrically heated steam generator (Adrop Feuchtemesstechnik GmbH, aTHMOS-RS-4). The steam was superheated to around 260 °C and fed through a separate port into the reactor cavity via an electrically heated, insulated Teflon pipe at 180 °C, therefore entering the solar reactor at roughly 200 °C. The temperature of the reacting ceria was monitored at four positions distributed over the back surface of the RPC using B-type thermocouples. The average of these temperature measurements was defined as the nominal RPC temperature $T_{RPC,nom}$. The pressure inside the reactor was measured at the gas outlet and through a lateral port using Pirani gauge sensors combined with a capacitance diaphragm vacuum gauge (Leybold, THERMOVAC TTR 101 N). Up to four dry, multi-stage roots vacuum pumps (Pfeiffer Vacuum, ACP 40) were attached in parallel to the outlet port of the solar reactor via two parallel valves. A solenoid control valve (Bürkert Schweiz AG, valve type 2875, controller type 8605) was used to slowly evacuate the reactor at the beginning of the reduction step (path shown by the red arrows in **Figure 4.6**), and an electro-pneumatic valve with bigger nominal diameter (SMC Corporation, XLAV-50) was opened once the pressure was sufficiently low (< 200 mbar). During the oxidation step (path shown by the blue arrows in **Figure 4.6**), the vacuum pumps were bypassed by use of a smaller diameter electro-pneumatic valve (SMC Corporation, EVNB211B). Residual water was removed with a water-cooled glass condenser. Product gas composition was continuously (frequency 1 Hz) analyzed downstream using an electrochemical sensor for O_2 (Siemens, Ultramat 23), IR detectors for CO and CO_2 (Siemens, Ultramat 23), and a thermal conductivity based detector for H_2 (Siemens, Calomat 6). The gas composition was verified by gas chromatography (Agilent, 490 Micro GC). The produced syngas was either vented or collected and compressed in a 50 L gas cylinder to further process it with the on-site Fischer-Tropsch unit.

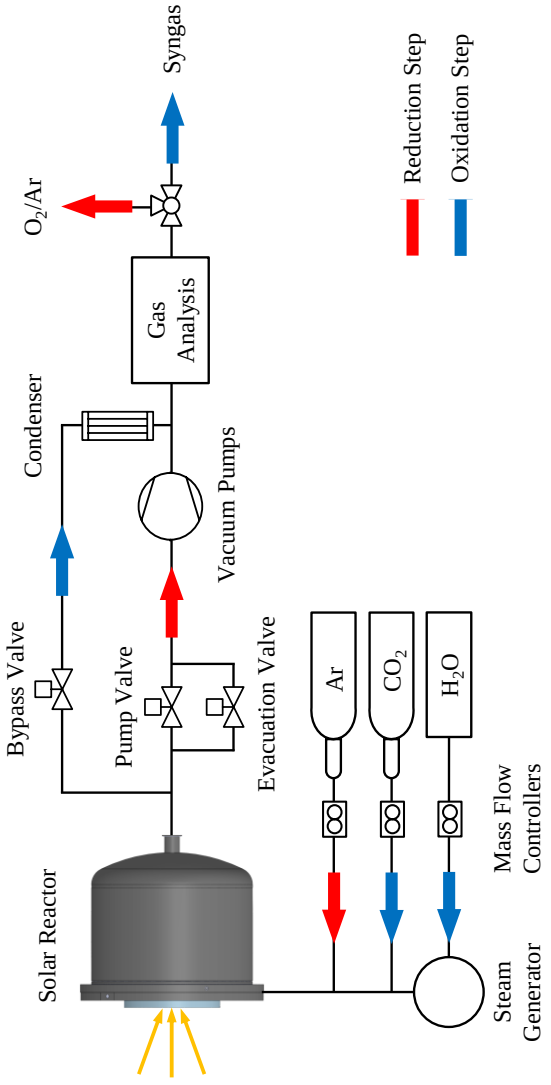

Figure 4.6. Simplified schematic of the experimental setup in the solar tower. During the endothermic reduction step, Ar flow is used to protect the quartz window and is pumped out together with the released O_2, while the reactor is under vacuum and irradiated with concentrated solar radiation. During the exothermic oxidation step, the ceria is re-oxidized with CO_2 and/or H_2O, therefore producing CO and/or H_2.

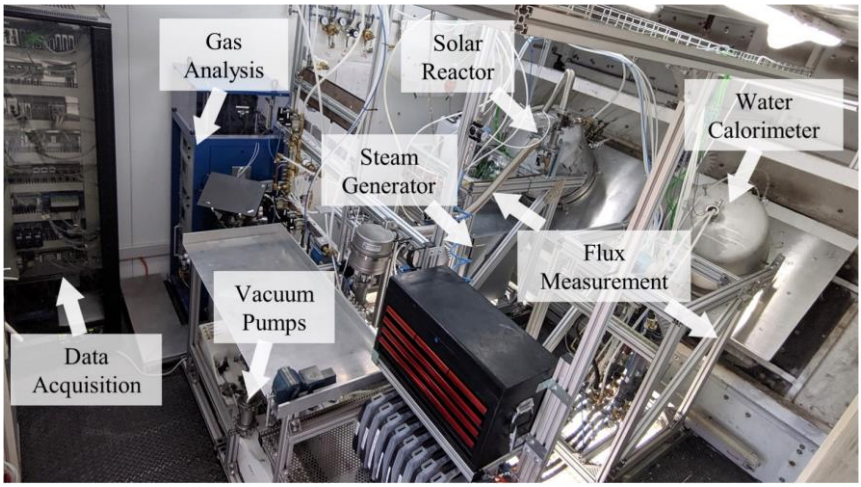

Figure 4.7. Overview of the experimental level in the solar tower with the major subsystems indicated.

The operation procedure for the solar reactor during a representative experiment is shown in **Figure 4.8**. The reactor was first slowly preheated with a radiative power input P_{solar} ramping up to around 10 kW for up to one hour, followed by a pre-cycle. During a pre-cycle, the reactor was heated with P_{solar} approaching full power when the nominal reduction end temperature was reached. Reduction was terminated by placing the FMAS target in front of the reactor (thereby effecting P_{solar} = 0 kW) and a series of power measurements as described in section 4.1.3, simultaneously letting the reactor cool down to the nominal oxidation start temperature. The ceria was re-oxidized using CO_2 and/or H_2O. The primary cycle was initiated by evacuating the reactor using the vacuum pumps and focusing a defined number of heliostats onto the reactor's aperture. The number of heliostats in operation was not changed during a single reduction step. To protect the quartz window from deposition of sublimated ceria and to govern the fluid flow when operating under vacuum conditions, an argon flow rate of 5 L min^{-1} was introduced to the reactor directly behind the window. When the variable reduction end temperature was reached, re-oxidation was initiated by removing input power and repressurizing the reactor with CO_2 and/or H_2O. After the nominal RPC temperature decreased to the defined oxidation start temperature

by natural cooling, CO_2 and/or H_2O was flown through the reactor at constant rates but variable ratio and ranges, producing a mixed flow in the outlet comprised of H_2, CO and unreacted CO_2, after the removal of excess water. The ceria was either fully re-oxidized or oxidation was stopped when a predefined criteria was met. After the oxidation of the last cycle was terminated, the solar reactor naturally cooled down, typically approaching ambient temperature the next morning. Experiments were usually terminated if clouds appeared. Up to eight consecutive cycles were performed per day with an average cycle time of around 50 minutes. An interesting characteristic of the solar concentrating facility can be seen in **Figure 4.8**: because tracking and optical errors increase the further away from solar noon, P_{solar} steadily increases during every cycle in the morning and decreases during cycles after solar noon, even though the number of focused heliostats was constant for single cycles. The experimental facility is shown in operation in **Figure 4.9**.

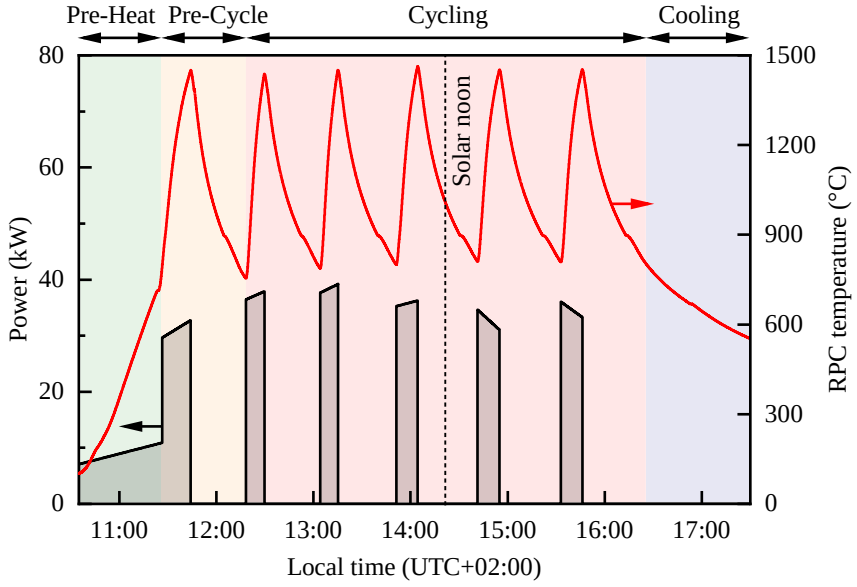

Figure 4.8. Operation strategy for the solar reactor during a representative experiment, including a pre-heating phase, a pre-cycle, consecutive cycling, and a natural cooling phase. Indicated are the solar radiative power input to the reactor, P_{solar}, in black and the nominal RPC temperature in red.

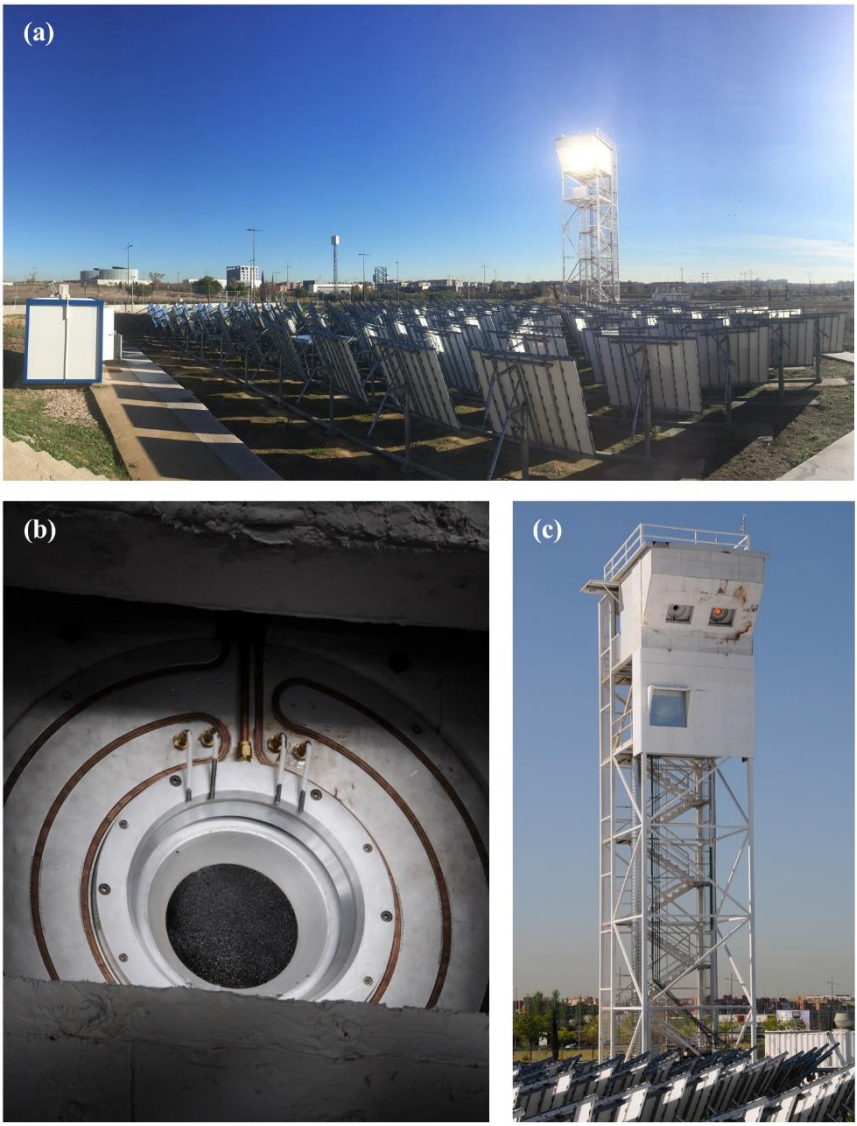

Figure 4.9. Photographs of the experimental facility in operation: **(a)** the field of heliostats heating up the solar reactor in the tower during the reduction step; **(b)** the irradiated front of the solar reactor photographed with a neutral-density filter, showing the dark color of the ceria RPC cavity in the partially reduced state, **(c)** the solar tower with the glowing ceria RPC cavity while cooling down shortly after the end of the reduction step.

4.2 Results and discussion

4.2.1 Cyclic performance

The thermochemical performance of the solar reactor is assessed with the solar-to-fuel energy conversion efficiency, which is defined as

$$\eta_{\text{solar-to-fuel}} = \frac{Q_{\text{fuel}}}{Q_{\text{solar}} + Q_{\text{pump}} + Q_{\text{inert}}} \tag{4.1}$$

Q_{fuel} is calculated as the amount of produced fuel integrated over an entire cycle multiplied with the higher heating value of the fuel (ΔH_{CO} = 283 kJ mol^{-1} and ΔH_{H_2} = 286 kJ mol^{-1}). Assuming complete re-oxidation, the energy content of the fuel produced in a cycle can also be calculated as $Q_{\text{fuel}} = \Delta H_{\text{fuel}} \cdot 2\int r_{\text{O}_2}\, dt$, where r_{O_2} is the rate of released oxygen during the reduction step. Q_{solar} is the total solar energy input integrated over the reduction step. Q_{pump} and Q_{inert} are the energy penalties associated with vacuum pumping and the consumption of the inert gas Ar during the reduction step, respectively, and are calculated as described in section 2.1.4.

For the operation of the solar reactor, pure CO_2 splitting offers some advantages compared to the co-splitting of H_2O and CO_2 or the oxidation with pure H_2O. The main technical challenge when utilizing H_2O as oxidant is to make sure that no water condenses inside the solar reactor. At the same time, any unreacted water needs to be condensed and removed from the product gas mixture exiting the reactor to avoid damaging any instruments or processes located downstream. Even though the co-production of H_2 and CO (syngas) with the solar reactor offers economic advantages for the subsequent production of liquid hydrocarbon fuels, syngas could also be produced from pure CO by adding the water-gas shift reaction as an additional process step [98].

Figure 4.10 shows the nominal RPC temperature, the reactor pressure as well as the O_2 and CO evolution rates for three consecutive CO_2 splitting cycles. The solar radiative power input P_{solar}, averaged over each reduction step, was increased from 45.7±6.7 kW in the first cycle to 55.8±8.2 kW in the third cycle. In this experiment, the reactor was heated with variable P_{solar} from $T_{\text{red,start}}$ = 700 °C to $T_{\text{red,end}}$ = 1500 °C while continuously pumping vacuum and flowing Ar

at $\dot{V}_{Ar}$ = 5.0 L min^{-1}. Afterwards, the reactor was filled with CO_2 to atmospheric pressure while cooling down at P_{solar} = 0 kW. Starting at $T_{ox,start}$ = 900 °C, the ceria was fully re-oxidized with $\dot{V}_{CO2}$ = 50 L min^{-1} until $T_{ox,end}$ = 700 °C, corresponding to $T_{red,start}$ of the following cycle. The molar ratio of CO produced to O_2 released was in the range of 2.03–2.06±0.21 for the three cycles, implying that the oxygen nonstoichiometry was fully exploited for fuel production. **Figure 4.10 (b)** shows the effect of varying P_{solar} on three selected performance indicators, namely the volume of produced O_2 and CO, the reduction time t_{red} and the solar-to-fuel energy conversion efficiency $\eta_{solar\text{-}to\text{-}fuel}$. Note that the error margin of P_{solar} is not shown for simplicity. The experimental conditions and measured results of the third cycle with highest power input and efficiency are also summarized in **Table 4.1**.

The reduction time significantly decreased from 6.7 min at P_{solar} = 45.7±6.7 kW to 5.8 min at P_{solar} = 52.8±7.8 kW. Interestingly, it slightly increased for a further power increase to P_{solar} = 55.8±8.2 kW. This is attributed to a slight increase in actual reduction end temperature, even though the nominal end temperature was hold constant at $T_{red,end}$ = 1500 °C. The nominal RPC temperature is defined as the average of four measurement points distributed over the back, non-irradiated surface of the RPC, and it was observed that the RPC generally heats up more uniformly with increasing cycle number. Because of the slightly higher reduction time at maximum power input, the amounts of produced O_2 and CO also increased to 45.8±0.9 L and 92.9±7.4 L, respectively. These trends of reduction time and fuel amount lead to a general trend of increasing efficiency with increasing power input, reaching a maximum of $\eta_{solar\text{-}to\text{-}fuel}$ = 5.6±1.0% at P_{solar} = 55.8±8.2 kW, while the average efficiency of the three consecutive cycles was $\eta_{solar\text{-}to\text{-}fuel}$ = 5.2±1.0%. This trend, in correspondence to the results of the heat transfer model presented in chapter 3, suggest that even higher efficiencies could be reached by further increasing P_{solar}. However, this would require a more precise and costly solar concentrating facility and might detrimentally affect the mechanical stability of the ceria RPCs over a large number of cycles.

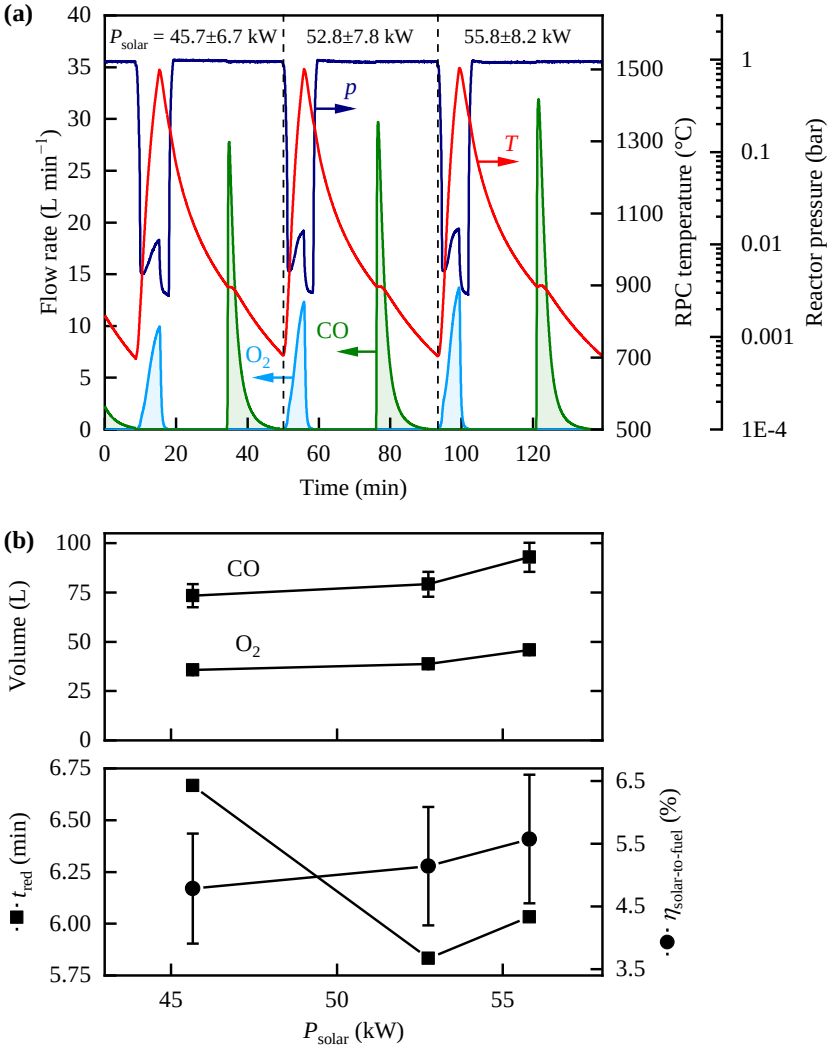

Figure 4.10. (a) Nominal RPC temperature, reactor pressure and O_2 and CO evolution rates as a function of time for three consecutive CO_2 splitting cycles with increasing average solar radiative power input P_{solar} during reduction. **(b)** Volume of produced O_2 and CO, reduction time t_{red} and efficiency $\eta_{solar\text{-}to\text{-}fuel}$ of the same cycles as a function of P_{solar}. The error margin of P_{solar} is not shown for simplicity. Experimental conditions during reduction: $T_{red,start}$ = 700 °C, $T_{red,end}$ = 1500 °C, $\dot{V}_{Ar}$ = 5.0 L min^{-1} at $p_{reactor} \leq$ 15 mbar. Experimental conditions during oxidation: $T_{ox,start}$ = 900 °C, $T_{ox,end}$ = 700 °C, $\dot{V}_{CO_2}$ = 50 L min^{-1} at atmospheric pressure. Ceria RPC mass m_{RPC} = 17.8 kg.

Table 4.1. Experimental conditions and results of the CO_2 splitting cycle with the highest average solar radiative power input during reduction, P_{solar}, and resulting maximum solar-to-fuel energy conversion efficiency $\eta_{solar\text{-}to\text{-}fuel}$.

Variable	Symbol	Value	Unit
Ceria RPC mass	m_{RPC}	17.8	kg
Average solar power input during reduction	P_{solar}	55.8±8.2	kW
Reduction start temperature	$T_{red,start}$	700	°C
Reduction end temperature	$T_{red,end}$	1500	°C
Oxidation start temperature	$T_{ox,start}$	900	°C
Oxidation end temperature	$T_{ox,end}$	700	°C
Ar flow rate during reduction	$\dot{V}_{Ar}$	5.0	L min^{-1}
CO_2 flow rate during oxidation	$\dot{V}_{CO2}$	50	L min^{-1}
Reactor pressure at end of reduction	p_{red}	15.0±2.3	mbar
Reduction duration	t_{red}	6.0	min
Oxidation duration	t_{ox}	18.7	min
Cycle duration		46.2	min
Mean heating rate		133	°C min^{-1}
Peak O_2 evolution rate		13.7±0.3	L min^{-1}
Total amount of O_2 released		45.8±0.9	L
Average nonstoichiometry of ceria	δ	0.039±0.001	
Peak CO evolution rate		31.9±2.6	L min^{-1}
Total amount of CO produced		92.9±7.4	L
Average conversion of CO_2 to CO		9.5±0.8	%
Molar ratio CO/O_2		2.03±0.21	
Vacuum pumping energy	Q_{pump}	468	kJ
Inert gas Ar separation energy	Q_{inert}	96	kJ
Solar-to-fuel energy conversion efficiency	$\eta_{solar\text{-}to\text{-}fuel}$	5.6±1.0	%

The effect of changing the reduction end temperature on the performance of the solar reactor can be assessed with the instantaneous solar-to-fuel energy conversion efficiency. **Figure 4.11** shows the instantaneous $\eta_{\text{solar-to-fuel}}$ and the O_2 yield as a function of the nominal RPC temperature for the CO_2 splitting experiment summarized in **Table 4.1**. The corresponding reduction times are indicated on the upper horizontal axis. Note that for this calculation, the O_2 measured after the end of the reduction step is neglected, which is why the maximum instantaneous $\eta_{\text{solar-to-fuel}}$ is slightly lower than the efficiency reported in **Table 4.1**. The tail of measured O_2 once P_{solar} is set to zero at the end of reduction has two causes: temperature equilibration within the ceria RPC and diffusion and flow mixing effects of the mixture of O_2 and Ar in the reactor and the piping between the reactor and the gas analysis.

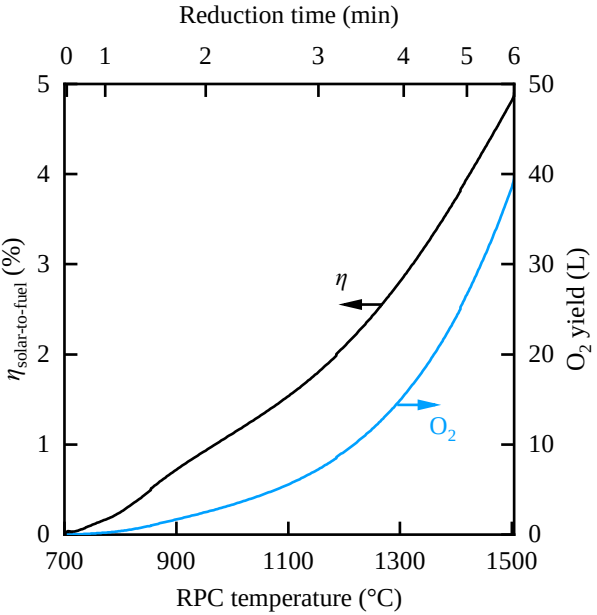

Figure 4.11. Instantaneous solar-to-fuel energy conversion efficiency $\eta_{\text{solar-to-fuel}}$ and O_2 yield as a function of the nominal RPC temperature for the CO_2 splitting cycle summarized in **Table 4.1**. Also indicated on the upper horizontal axis are the corresponding reduction times.

The O_2 yield increases exponentially with increasing RPC temperature due to the exponential correlation between oxygen nonstoichiometry δ and temperature for ceria [63]. The efficiency $\eta_{\text{solar-to-fuel}}$ also increases with increasing RPC temperature, but the slope decreases with temperature due to increasing heat losses and the energy consumed by the endothermic reduction reaction. This trend indicates that even higher $\eta_{\text{solar-to-fuel}}$ could be reached by increasing the reduction end temperature. However, care must be taken to avoid local sublimation of ceria on the directly irradiated RPC surface, and further increasing the reduction end temperature might also detrimentally affect the structural integrity of the ceria RPC cavity over a larger number of redox cycles.

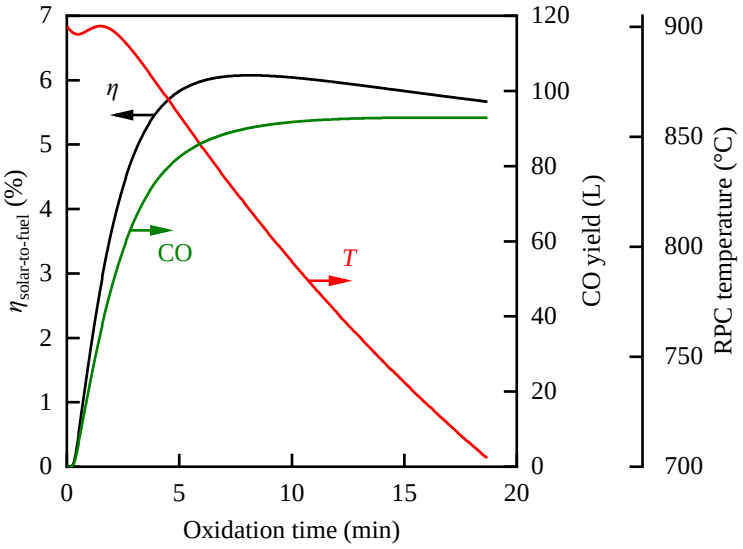

Figure 4.12. Instantaneous solar-to-fuel energy conversion efficiency $\eta_{\text{solar-to-fuel}}$, CO yield and nominal RPC temperature as a function of the oxidation time for the CO_2 splitting cycle summarized in **Table 4.1**.

During oxidation, prolonging the oxidation time until the ceria is completely re-oxidized maximizes the fuel yield per cycle, but also increases the temperature swing between start and end of reduction because the reactor cools down during oxidation. **Figure 4.12** shows the instantaneous $\eta_{\text{solar-to-fuel}}$, the CO yield and the nominal RPC temperature versus the oxidation time for the same CO_2 splitting

cycle (summarized in **Table 4.1**). To calculate the instantaneous $\eta_{\text{solar-to-fuel}}$, the energy savings due to two effects were approximated: higher reduction start temperatures and less energy consumed by the endothermic reduction reaction if the oxidation time is shortened and the ceria is not fully re-oxidized. The efficiency peaks at $\eta_{\text{solar-to-fuel}}$ = 6.1% after 8.0 min of oxidation and a fuel yield of 90.0 L of CO, which is 97% of the fuel produced at the end of the oxidation step. Therefore, $\eta_{\text{solar-to-fuel}}$ could be slightly increased by stopping the oxidation step before the ceria is fully re-oxidized. Furthermore, the share of unreacted CO_2 in the product gas increases with increasing oxidation time, which can have a detrimental effect on the efficiency of the downstream syngas processing. This is discussed in more detail in section 4.2.3.

4.2.2 Comparison to heat transfer model and energy balance

To get a further insight into the thermal performance of the solar reactor at its nominal operating condition, the heat transfer model of the solar reactor, described in detail in chapter 3, was used to simulate the CO_2 splitting cycle with maximum efficiency, summarized in **Table 4.1**. The geometry of the porous RPC domain was adapted to the design described in section 4.1.1 that is optimized for the operation in the solar tower. The solar concentrating facility was modelled as a set of rays uniformly distributed over the aperture area with a directional distribution that is also uniformly distributed and confined with a rim angle of 40 degrees, which closely approximates the specifications of the heliostat field.

In **Figure 4.13**, the nominal RPC temperature and the O_2 release rate are shown for the experiment (solid lines) and the simulation (dashed lines). The RPC temperature is slightly overestimated in the simulation, reaching 1557 °C at the end of the reduction step compared to 1500 °C for the experiment. When considering the uncertainty in the measurement of P_{solar}, the experimentally measured temperature profile lies well within the set of possible simulation results. The red shaded area indicates the possible nominal RPC temperatures when accounting for the uncertainty of P_{solar} in the simulation, calculated by running the simulation with both the minimum and the maximum values for P_{solar}. The same trend can be seen for the rate of O_2 released. The experimentally

measured rates are smaller than the numerically calculated rates for P_{solar} = 55.8 kW at all times during the reduction step, due to the overestimation of the RPC temperature in the simulation. When accounting for the uncertainty of P_{solar} though (grey shaded area in **Figure 4.13**), the experimental curve lies within the set of possible simulation results. The only significant difference between experiment and simulation occurs at the end of the reduction step. While the O_2 release stops within 30 seconds according to the simulation when the radiative power input is turned off at the end of the reduction, the experimentally measured O_2 rate decreases more slowly. The slower decrease is attributed to diffusion and flow mixing effects of the mixture of O_2 and Ar in the reactor and the piping between the reactor and the gas analysis.

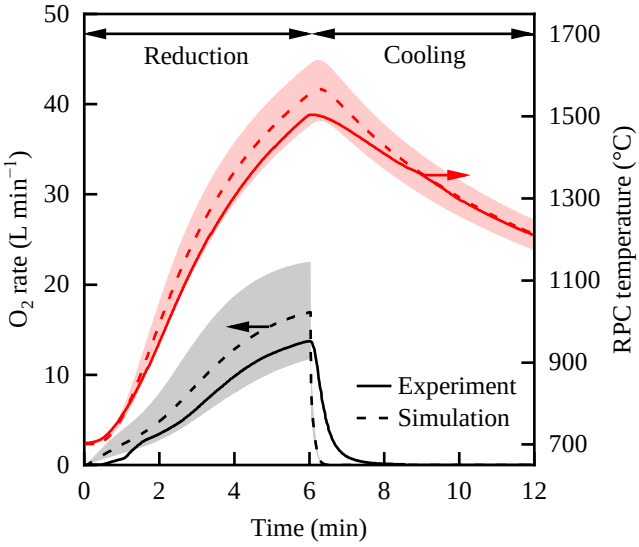

Figure 4.13. Experimentally measured (solid lines) and numerically calculated (dashed lines) nominal RPC temperature as well as O_2 evolution as a function of time, during the reduction step and the subsequent natural cooling phase. While the dashed lines correspond to the simulation result with P_{solar} set to the experimentally determined value of 55.8 kW, the shaded regions indicate the set of results when accounting for the measurement uncertainty of P_{solar} in the simulation.

For P_{solar} = 55.8 kW, the heat transfer model predicts an average temperature difference between the directly irradiated front and the back of the RPC of 229 °C at the end of the reduction step, and a maximum temperature within the entire RPC domain of $T_{RPC,max}$ = 1850 °C, locally occurring at the directly irradiated inner RPC surface. This means that towards the back RPC surface, lots of energy is needed to heat the RPC, but the ceria does not contribute that much to the reaction due to the exponential decrease of reduction extent with decreasing temperature. Correspondingly, the ratio between the actually released O_2 and the amount of O_2 that could theoretically be released if all ceria mass would reach the maximum temperature within the RPC domain at the end of the reduction step is estimated to be 36%. The actually released amount of O_2 was measured during the corresponding experiment and is 45.8 L (see **Table 4.1**). The theoretical O_2 release at a uniform RPC temperature of $T_{RPC,max}$ = 1850 °C, as predicted by the model, was calculated using the correlation for the oxygen nonstoichiometry δ that was also implemented in the model (see **Table 3.1**). An oxygen partial pressure of p_{O_2} = 12 mbar was assumed, which corresponds to the measured partial pressure at the end of the reduction step of the respective experiment. The correlation for δ, developed by Ackermann [136], is based on an oxygen defect model that was fitted to experimental data available for temperatures up to 1500 °C and extrapolated to higher temperatures. It predicts a reduction extent of $\delta(T = 1850\ °C, p_{O_2} = 12\ mbar) = 0.109$, which corresponds to an oxygen volume of 127 L for the experimental ceria mass loading of m_{RPC} = 17.8 kg. The calculated ratio of 36% highlights that the performance of the solar reactor could be further increased if the ceria RPC could be heated more uniformly. As shown in the previous chapter 3, more volumetric absorption of the incoming solar radiation is needed for more uniform heating of the ceria structure, which could be achieved for example by increasing the RPC macropore size or with advanced ceria structures that feature a gradient in porosity.

The energy balance according to the numerical heat transfer model is visualized in **Figure 4.14** for the cycle at P_{solar} = 55.8 kW. The entire pie corresponds to Q_{solar}, the solar radiative energy input integrated over the reduction step. Indicated are losses by reradiation from the hot cavity, the change in sensible

heat content of the RPC, the remaining reactor components (Al_2O_3–SiO_2 insulation, aluminum front, reactor shell and insulating jacket), the energy consumed by the endothermic reduction reaction, losses by reflection and absorption of solar radiation at the quartz window, the conductive heat loss to the water-cooled reactor front, and other heat losses, together with their shares in Q_{solar}. Other heat losses include convection and radiation at the outer reactor surfaces and reflection of incoming solar radiation inside the reactor cavity.

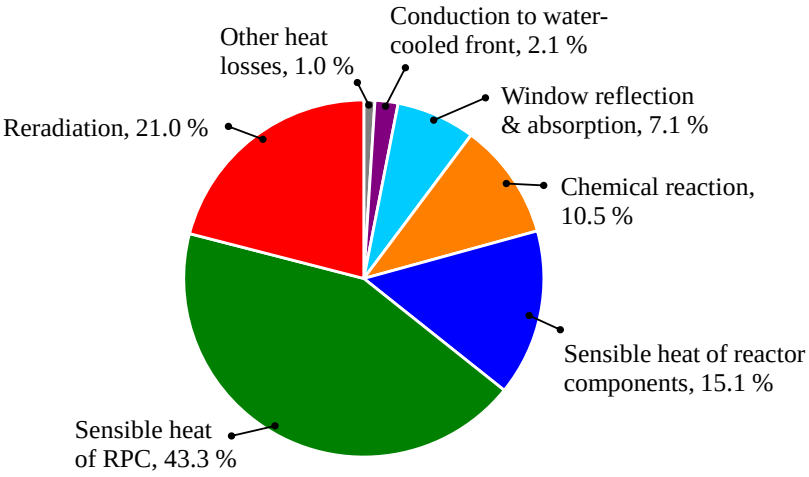

Figure 4.14. Energy balance of the CO_2 splitting cycle at a solar radiative power input of P_{solar} = 55.8 kW, which resulted in the highest demonstrated solar-to-fuel energy conversion efficiency (corresponding experimental values are summarized in **Table 4.1**). Other heat losses include convection and radiation at the outer reactor surfaces and reflection of incoming solar radiation inside the reactor cavity. The entire pie corresponds to Q_{solar}, the solar radiative energy input integrated over the reduction step.

Losses by reradiation from the hot cavity account for 21.0% of the energy input. By far the most significant share is the energy needed for sensible heating of the reactor components, which highlights again the importance of implementing heat recovery in order to further boost the efficiency of such reactor technology in the future. 43.3% of Q_{solar} is used for sensible heating of the RPC and 15.1% for sensible heating of the remaining reactor components. The energy consumed by the endothermic reduction reaction of ceria accounts for 10.5% of the solar energy input, and 7.1% is lost by reflection and absorption at the quartz window.

2.1% of Q_{solar} is lost by conduction to the water-cooled aluminum front, while the remaining heat losses by convection and radiation at the outer reactor surfaces and reflection of incoming solar radiation inside the reactor cavity account for 0.5% or less each.

Apart from the solar radiative energy entering the reactor through the aperture (Q_{solar}), for the operation of the solar reactor energy is also needed to drive the vacuum pumps (Q_{pump}) and to provide the inert gas Ar that is consumed during the reduction step (Q_{inert}), which is accounted for in the definition of the solar-to-fuel energy conversion efficiency (equation (4.1)). Compared to the solar radiative energy input, both energy penalties are relatively small, with Q_{pump} and Q_{inert} amounting to 2.6% and 0.5% of Q_{solar}, respectively.

4.2.3 Optimization of syngas composition

Different operational modes for the solar reactor are conceivable in order to produce syngas with a composition that is suitable for Fischer-Tropsch synthesis. H_2 and CO can either be produced separately with pure splitting of H_2O and CO_2 in different redox cycles or simultaneously by co-feeding H_2O and CO_2 during the oxidation step. **Figure 4.15** summarizes an exemplary cycle for the simultaneous production of H_2 and CO. It shows the nominal RPC temperature, the reactor pressure and the flow rates of produced O_2, CO and H_2. The solar radiative power input P_{solar}, averaged over the reduction step, was 42.0±6.2 kW. In contrast to pure CO_2 splitting, where the reactor pressure increased with increasing amount of O_2 released during the reduction step, the reactor pressure slowly decreased from around 70 mbar to 25.2±3.8 mbar at the end of the reduction step. This is attributed to the removal of liquid water that accumulated inside the solar reactor during the previous oxidation step. Because the reactor front and the aperture are water-cooled, local spots of the solar reactor retain temperatures below the boiling point of water. Therefore, a small amount of the water that enters the reactor as steam during the oxidation step condenses and remains in the reactor until the next reduction step. When the reactor pressure is decreased at the beginning of the next cycle, the liquid water evaporates again because of the lower boiling temperature under vacuum, but the pressure only

slowly decreases until all residual water is removed from the solar reactor. The extent of water condensation during oxidation was decreased considerably by controlling the cooling water flow rate but could not be avoided completely. After the target reduction end temperature of 1500 °C was reached, the reactor was repressurized with a mixed flow of 0.033 mol s^{-1} of H_2O and 10 L min^{-1} of CO_2, corresponding to a molar feeding ratio of 4.5. Starting at a nominal RPC temperature of 900 °C, the same amount of steam and CO_2 was fed to the reactor to produce a mixed flow of H_2 and CO together with unreacted H_2O and CO_2.

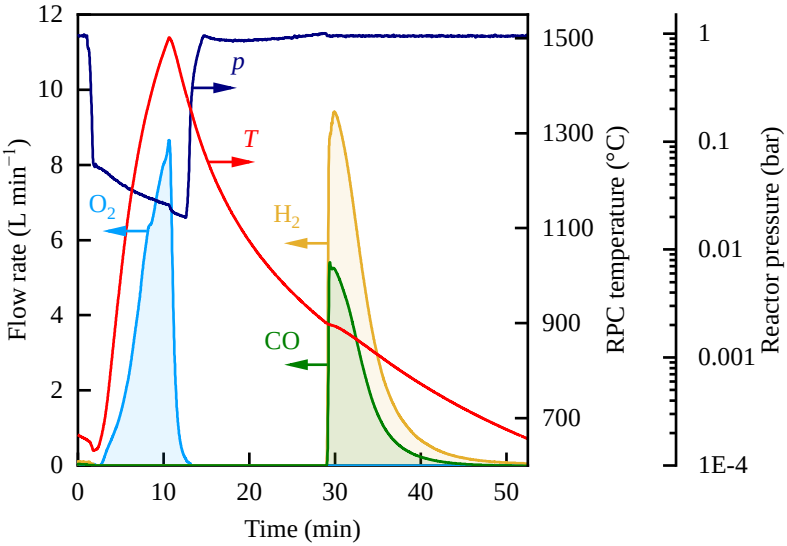

Figure 4.15. Nominal RPC temperature, reactor pressure as well as O_2, CO and H_2 evolution rates of an exemplary cycle for the simultaneous splitting of CO_2 and H_2O. Experimental conditions during reduction: P_{solar} = 42.0±6.2 kW, $T_{red,start}$ = 632 °C, $T_{red,end}$ = 1502 °C, $\dot{V}_{Ar}$ = 5.0 L min^{-1} at $p_{reactor} \leq$ 70 mbar. Experimental conditions during oxidation: $T_{ox,start}$ = 900 °C, $T_{ox,end}$ = 654 °C, $\dot{n}_{H_2O}$ = 0.033 mol s^{-1}, $\dot{V}_{CO_2}$ = 10 L min^{-1} at atmospheric pressure. Ceria RPC mass m_{RPC} = 18.1 kg.

Both H_2 and CO production peaked shortly after oxidation started at rates of 9.4±0.8 L min^{-1} for H_2 and 5.4±0.4 L min^{-1} for CO and decreased slowly until the ceria was fully re-oxidized after 24.0 min of oxidation at a nominal RPC temperature of 654 °C. Integrated over the entire cycle, a total amount of 36.2±0.7 L O_2, 48.9±3.9 L H_2 and 24.4±2.0 L CO was produced. This

corresponds to a molar ratio of H_2 and CO to O_2 of 2.03±0.21, indicating that the oxygen nonstoichiometry was fully exploited for fuel production, and a ratio of H_2 to CO of 2.01±0.35. The corresponding solar-to-fuel energy conversion efficiency was 4.1±0.8%. Note that the operating conditions were not optimized for maximum efficiency. The efficiency could be further increased especially when operating at a higher solar radiative power input P_{solar}, as demonstrated in section 4.2.1 for pure CO_2 splitting.

By adjusting different operational parameters of the solar reactor, the composition of the produced syngas can be controlled. **Figure 4.16** shows the ratio of H_2 and CO in the produced syngas as a function of the molar ratio between H_2O and CO_2 fed to the reactor during oxidation for different feeding ratios at oxidation start temperatures of $T_{ox,start}$ = 900 °C and 800 °C. The remaining operating conditions of the solar reactor were kept as constant as possible: the solar radiative power input P_{solar}, averaged over the reduction step, was in the range of 36.0–42.0±6.2 kW while the reactor was under vacuum pressure of less than 80 mbar, the reduction end temperature was $T_{red,end}$ = 1500±2 °C, and complete re-oxidation was performed with a total flow rate of $\dot{V}_{H2O} + \dot{V}_{CO2}$ = 70 L min^{-1} (volume flow rate calculated at 373.15 K and 101’325 Pa for H_2O and at 273.15 K and 101’325 Pa for CO_2) at atmospheric pressure.

The dashed line is a linear fit of the results with an oxidation start temperature of 900 °C, showing a clear trend of increasing ratio of H_2 to CO in the product gas with increasing molar feeding ratio of H_2O to CO_2. According to these results, if the oxidation start temperature is set to 900 °C, H_2O and CO_2 has to be fed to the reactor at a molar ratio between 4.43 and 5.25 in order to produce syngas with a ratio of H_2 to CO in the range of 2−2.5 that is suitable for Fischer-Tropsch synthesis. Alternatively, the syngas composition can also be modified by changing the oxidation start temperature. Decreasing the oxidation start temperature to 800 °C resulted in a ratio of H_2 to CO of 2.94±0.51 compared to 2.01±0.35 at $T_{ox,start}$ = 900 °C with the same molar H_2O/CO_2 feeding ratio of 4.46±0.23. This effect can be explained at least in part because H_2O dissociation is thermodynamically favored at lower temperatures compared to the dissociation of CO_2 [87].

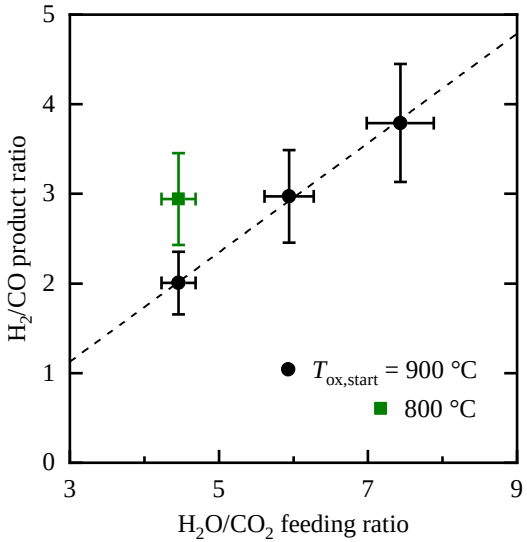

Figure 4.16. Ratio of H_2 and CO in the produced syngas as a function of the ratio between H_2O and CO_2 in the reactant gas mixture for oxidation start temperatures of 900 °C and 800 °C and otherwise similar experimental conditions. The dashed line is a linear fit of the results with $T_{ox,start}$ = 900 °C.

In section 4.2.1, the effect of stopping the oxidation step before the ceria is fully re-oxidized on the solar reactor efficiency was discussed. The extent of oxidation also has an effect on the composition of the produced syngas, and complete re-oxidation is only possible if the oxidant is provided in excess. Unreacted H_2O can easily be separated from the gas mixture exiting the solar reactor via condensation, but the removal of excess CO_2 is more complex. For the Fischer-Tropsch process, the removal of unreacted CO_2 from the syngas is not always necessary, but the efficiency of the process usually decreases with increasing CO_2 content [15].

Figure 4.17 shows the yield of H_2 and CO as well as the cumulative concentrations of H_2, CO and CO_2 in the accumulated syngas as a function of the oxidation time for the experiment that was presented in **Figure 4.15**. The cumulative concentration is defined as the concentration of the respective component in the gas that accumulated since the beginning of the oxidation step (oxidation time = 0 min), after the removal of excess water through condensation.

After 2.0 min of oxidation time, the cumulative concentration of fuel in the accumulated syngas reached a maximum with 46.0% H_2 and 25.2% CO, the remaining 28.8% being unreacted CO_2. However, only 16.1 L of H_2 and 8.9 L of CO is produced after 2.0 min of oxidation, corresponding to 34.1% of the total fuel yield for complete re-oxidation. If the oxidation is stopped after 7.0 min for example, already 86.0% of the potential fuel is produced (41.2 L H_2 and 21.8 L CO), and the cumulative concentrations of H_2 and CO in the syngas are still relatively high with 37.3% H_2 and 19.7% CO. If oxidation is further carried on, the additional amount of fuel that can be produced is relatively small, but the accumulated syngas is diluted with unreacted CO_2, which eventually reaches a cumulative concentration exceeding 70% for oxidation times of 20 min and more. The molar ratio between H_2 and CO in the produced syngas increased slightly from a minimum of 1.81 at an oxidation time of 1.2 min to a ratio of 2.0 at the end of oxidation.

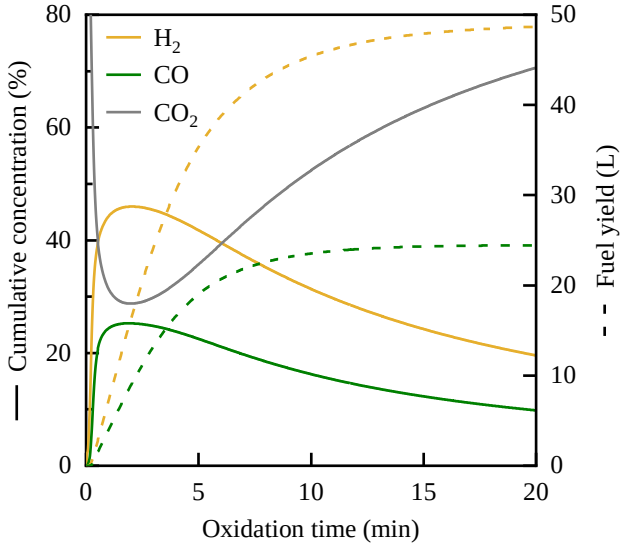

Figure 4.17. Fuel yield of H_2 and CO and cumulative concentrations of H_2, CO and CO_2 in the accumulated syngas as a function of the oxidation time for the experiment presented in **Figure 4.15**.

4.2.4 Long-term operation

Stable performance of the solar reactor over a large number of redox cycles is essential for any potential commercial application. The morphological stability of the same type of RPCs with dual-scale porosity that is used here was previously demonstrated with 227 consecutive redox cycles in a 4 kW solar reactor [51] and with 500 consecutive cycles in an IR furnace [53]. For the solar reactor of this study, the structural integrity of the self-supporting ceria RPC structure is equally important. In order to assess the cycling stability of the ceria RPC cavity and to produce a significant amount of syngas that can be processed to liquid hydrocarbon fuels on-site using the Fischer-Tropsch unit, multiple consecutive cycles were performed with the solar reactor. Based on the findings from the previous section 4.2.3, appropriate operating conditions for the solar reactor were chosen to produce syngas with a composition that is suitable for Fischer-Tropsch processing. An ideal composition of the syngas for processing with the cobalt-based Fischer-Tropsch reactor is a molar ratio of H_2 to CO of around 2.15 [15]. In total, 62 consecutive cycles were performed using the same RPC cavity with a ceria mass loading of m_{RPC} = 21.3 kg.

Figure 4.18 shows the nominal RPC temperature as well as the concentrations of O_2, H_2, CO and CO_2 measured in the product gas mixture leaving the solar reactor, after the removal of unreacted H_2O, for a representative cycle. For all cycles, the reactor was evacuated to vacuum pressures of less than 100 mbar before the solar power was applied to heat the ceria RPC to the target nominal temperature of 1450 °C. Shortly after the target temperature was reached, the reactor was slowly repressurized with a mixed flow of H_2O and CO_2 at a molar ratio of 5.2. Once the ceria RPC temperature naturally cooled down to the oxidation start temperature of 900 °C, a mixture of 0.039 mol s^{-1} of H_2O and 10 L min^{-1} of CO_2, corresponding to a molar feeding ratio of 5.2, was flown through the reactor. Oxidation was stopped when the measured CO_2 concentration approached 80% in order to limit the amount of residual CO_2 in the collected syngas. For the exemplary cycle shown in **Figure 4.18**, this corresponds to an oxidation time of 6.8 min during which a total amount of 29.5±2.4 L H_2 and 13.3±1.6 L CO was produced.

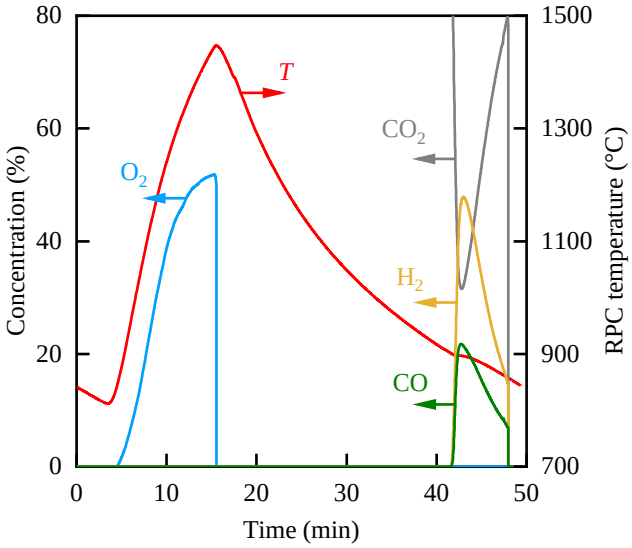

Figure 4.18. Nominal RPC temperature and concentrations of O_2, H_2, CO and CO_2 in the product gas leaving the solar reactor for a representative cycle during the long-term operation of the reactor. Experimental conditions during reduction: P_{solar} = 37.9±5.7 kW, $T_{red,start}$ = 812 °C, $T_{red,end}$ = 1447 °C, $\dot{V}_{Ar}$ = 5.0 L min^{-1} at $p_{reactor} \leq$ 100 mbar. Experimental conditions during oxidation: $T_{ox,start}$ = 900 °C, $T_{ox,end}$ = 853 °C, $\dot{n}_{H2O}$ = 0.039 mol s^{-1}, $\dot{V}_{CO2}$ = 10 L min^{-1} at atmospheric pressure. Ceria RPC mass m_{RPC} = 21.3 kg.

The nominal RPC temperature at the end of the reduction step as well as the total volume of H_2 and CO produced per cycle is shown in **Figure 4.19** for all 62 consecutive cycles. These cycles were conducted during nine experimental days between the 5th and the 29th of July 2019 with a total experimental time of more than 55 hours. Except for one day when the experiment was stopped early due to clouds, between six and eight cycles were conducted every day with an average cycle duration of 53.4 minutes. During the first 45 cycles (region I in **Figure 4.19**), the target reduction end temperature of 1450 °C was reached with a maximum deviation of 18 °C for all cycles except for the 24th cycle. During this cycle, the reduction step had to be interrupted at a nominal RPC temperature of 1393 °C because not enough power was available anymore to further heat the ceria RPC due to the late hour of operation. Also indicated are linear fits of the reduction end temperature and the total yield of H_2 and CO per cycle. As a result of the approximately constant operating conditions, the total fuel yield for both

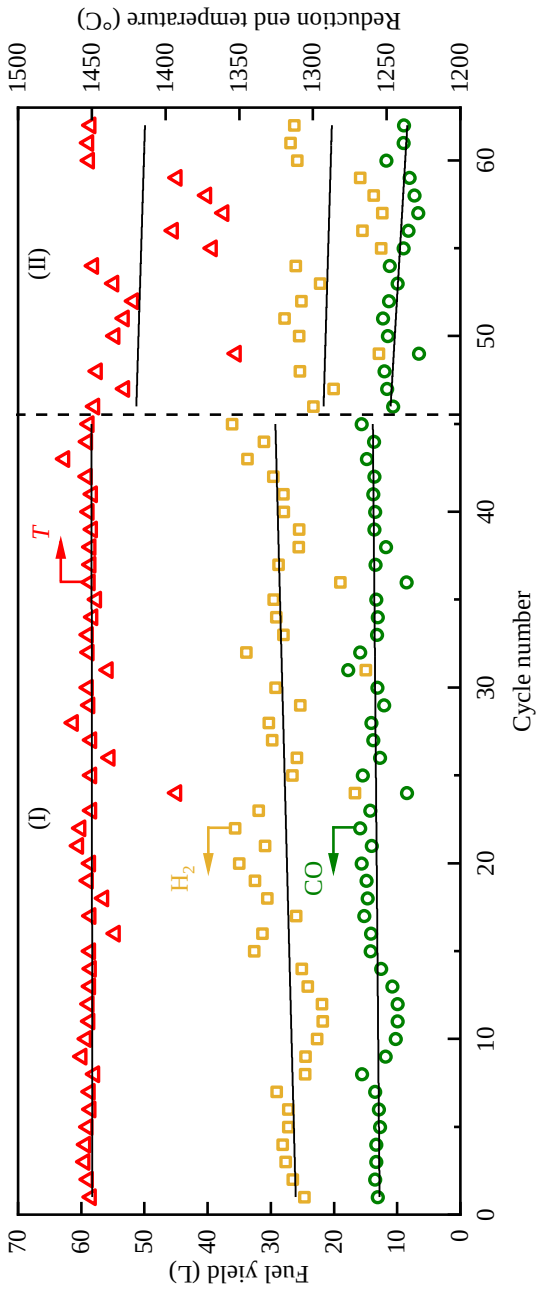

Figure 4.19. Nominal ceria RPC temperature at the end of the reduction step and total volume of produced H_2 and CO per cycle as a function of the cycle number for 62 consecutive redox cycles performed with the same RPC cavity with a ceria mass loading of m_{RPC} = 21.3 kg. Also indicated are linear fits of these temperatures and fuel yields, separately for the first 45 cycles (region I) with relatively constant or slightly increasing trends and for the last 17 cycles (region II) with generally lower levels and decreasing trends for increasing cycle number.

H_2 and CO was relatively constant. There is no visible trend of decreasing fuel yield, and the volume of H_2 produced per cycle even slightly increased with increasing cycle number.

During the last 17 cycles (region II of **Figure 4.19**), the variation in the reduction end temperature was larger, with a general trend of lower temperatures compared to region I and decreasing temperatures with increasing cycle number. The reason why the temperature stayed below the target reduction end temperature of 1450 °C during several cycles is the way the solar reactor was controlled. For safety purposes and in order to avoid local structural damage to the RPC, the reduction step was aborted whenever one of the four thermocouples distributed over the back surface of the RPC measured a temperature of 1550 °C. Due to the distribution of the incoming solar radiation over the irradiated RPC surface that was not perfectly uniform, the back of the ceria RPC cavity usually heated faster than the sides, but the temperature deviation from the nominal RPC temperature, defined as the average of the four measurement points, normally stayed below 100 °C. However, during the last two days of operation, a maximum temperature of 1550 °C was measured several times due to local structural degradation of the RPC resulting in faster heating of the back of the ceria RPC cavity. A direct link between the total fuel yield per cycle and the reduction end temperature can be observed. Lower volumes of H_2 and CO were produced during cycles with lower reduction end temperatures and there is a trend of decreasing fuel volumes with increasing cycle number and generally lower fuel yields compared to region I, in accordance with the trend for the reduction end temperature of these cycles.

The solar-to-fuel energy conversion efficiency averaged over the 62 consecutive cycles was 1.7±0.4%. Note that the operating conditions during these cycles were not optimized for maximum efficiency (as described in section 4.2.1) but for syngas yield and composition, with the aim of producing a significant amount of syngas suitable for Fischer-Tropsch processing during minimum experimental time. Summed up over all 62 consecutive cycles, 5191±364 L of syngas were produced with a composition of 31.8±3.2% H_2, 15.2±2.4% CO and 53.0±3.6% CO_2. Unreacted H_2O was separated with a water-cooled glass condenser located behind the gas outlet of the solar reactor. The syngas composition corresponds

to a molar ratio between H_2 and CO of 2.1, which fits the targeted syngas quality for Fischer-Tropsch synthesis. Most of the produced syngas was collected and stored on-site in a pressurized gas cylinder to further process it to liquid hydrocarbon fuels. However, especially during the first two days of operation, some of the produced syngas had to be vented because of a malfunction of the gas compressor and technical difficulties with the interface between the solar reactor and the gas compression system. Overall, around 91% of the produced syngas was collected and stored and subsequently processed with the on-site Fischer-Tropsch reactor. The analysis of the quantity and the composition of the product mixture was ongoing by the time of completion of this thesis.

With this experimental campaign, the technical feasibility of solar thermochemical H_2O and CO_2 splitting via ceria redox cycling was demonstrated under real-world conditions and at a relevant scale. Despite considerable progress, the ceria RPC is still the most delicate component of the solar reactor. Stable reactor performance was shown over 45 consecutive redox cycles without any visible degradation, but for the remaining 17 cycles, the performance slightly decreased, presumably due to the deterioration of the ceria RPC caused by the formation of cracks. These cracks mainly result from stresses induced by thermal and chemical expansion of ceria during reduction [65]. For any commercial application, a ceria RPC would probably have to withstand thousands of cycles before it could be repaired or replaced. Therefore, further progress with the manufacturing of mechanically strong ceria structures is essential. Adaptions of the manufacturing process or changes of the design specifications could further increase the mechanical strength of the RPCs. With lower maximum temperatures or smaller heating rates and temperature gradients, the formation of cracks could be alleviated but at the expense of lower reactor performance in terms of energy conversion efficiency. Even if the formation of cracks cannot be avoided, adjustments of the design of the solar reactor could help to prevent structural failure of the ceria RPC cavity. For example, a self-supporting design hold in place by gravity could be implemented more easily if the solar reactor's aperture is facing upwards when operated with a solar concentrating facility in beam-down operation.

4.3 Summary and conclusions

Solar thermochemical splitting of CO_2 and H_2O has been demonstrated with the 50 kW solar reactor using a solar concentrating facility located in Móstoles, Spain. The experimental facility consisted of three different subsystems: a high-flux solar concentrating heliostat field and tower, the solar reactor system including a dedicated power measurement setup, and a gas-to-liquid conversion plant to process the produced syngas to liquid hydrocarbon fuels on-site via Fischer-Tropsch synthesis. The solar reactor, installed on top of the solar tower, featured an adapted ceria RPC cavity for structural integrity in its operation position facing down onto the heliostat field and for maximum performance. For CO_2 splitting, a maximum solar-to-fuel energy conversion efficiency of 5.6±1.0% was experimentally demonstrated at a solar radiative power input of 55.8±8.2 kW. Simulating the same experiment with a transient heat transfer model revealed that 58.4% of the solar energy input was used for sensible heating of the ceria and the bulk reactor components, which highlights the need to implement solid heat recovery in order to further increase the efficiency of similar reactor technology in the future. For the co-splitting of H_2O and CO_2, different possibilities to control the composition of the produced syngas were demonstrated. At optimal operating conditions, 62 consecutive redox cycles were performed with the same ceria RPC cavity. Constant fuel yields were observed for the first 45 cycles, but for the remaining 17 cycles, the reduction end temperature had to be slightly decreased due to local structural degradation of the RPC, resulting in lower fuel yields per cycle. The syngas produced during these 62 cycles was collected and stored to further process it to liquid hydrocarbon fuels on-site via Fischer-Tropsch synthesis. These results demonstrate the feasibility of solar thermochemical H_2O and CO_2 splitting via ceria redox cycling at a relevant scale for an industrial application and at realistic operating conditions. Critical issues that remain are the structural integrity of the ceria RPC cavity over a large number of consecutive redox cycles and the technically challenging implementation of solid heat recovery to further increase the solar reactor efficiency.

5 Outlook and research recommendations

The ultimate goal of research on solar thermochemical splitting of H_2O and CO_2 is to find a way to produce transportation fuels that can replace currently used fossil fuels in an economical manner. Although there has been substantial progress over the last decades, major improvements are still necessary in order to achieve this goal. For a future solar fuels production plant, the solar reactor technology is the least developed process step. Other necessary steps, such as capturing CO_2, concentration of sunlight and liquid fuel production via Fischer-Tropsch synthesis, are further developed and commercial solutions are already available. Therefore, in order to decrease cost, most of the future research needs to focus on making the process step of splitting H_2O and CO_2 into syngas more efficient.

In order to increase the performance of a solar thermochemical reactor for H_2O and CO_2 splitting, research should continue on all scales, starting from fundamental research on materials to system analyses and optimization for the optimal integration of a solar reactor technology into a fuel production plant. Material research should continue on screening and testing of potential candidates for redox cycling, such as doped ceria or perovskites. Finding a material that reaches higher reduction extents or has lower reduction temperatures compared to ceria but similar oxidation characteristics could be beneficial not only for the efficiency of the solar reactor but also for the long-term stability of the active material structure.

On the scale of redox material structures, finding a way to manufacture ceria structures with larger pores or a gradient in porosity for better volumetric absorption of radiation and more uniform heating could further increase the reactor efficiency while decreasing the mechanical load on the material caused by high maximum temperatures. While there is a limit on pore size for RPCs,

novel manufacturing techniques such as additive manufacturing even offer the possibility to fabricate ordered porous structures with a tailored porosity gradient [95]. However, especially for complicated structures with ordered porosity, the geometry needs to be carefully optimized in order to outperform currently used RPC structures, for example with the use of suitable numerical models. Furthermore, verification of the long-term stability of RPC structures should be extended to more cycles. While relatively stable fuel production rates were shown over a few dozen cycles in the present work and a few hundred cycles with different reactors [51, 53], a structure would presumably have to withstand several thousands of cycles before it could be repaired or exchanged in a competitive industrial application. The possibility to repair broken ceria structures, to recycle the ceria of used structures for the fabrication of new ones as well as the automation of the fabrication process of ceria structures should also be investigated.

Apart from adapting the ceria structures, there are several other ways to improve the presented cavity receiver-reactor. The potential of actively cooling the ceria RPC structure between reduction and oxidation should be investigated. Active cooling could be realized for example by flowing a large amount of an inert gas such as nitrogen or argon through the structure after the end of the reduction step. The extracted heat could be stored in a separate thermal storage unit or used directly to preheat a second solar reactor if multiple reactors are operated simultaneously with a time shift between the cycles of different reactors. Alternatively, the extracted heat could be used to drive other processes needed for the operation of the solar reactor, such as evaporating water, preheating steam and CO_2, or driving the vacuum pumps, provided the heat can be converted to electricity first. Extracted heat could also be used to drive other process steps in a fuel production plant, either directly or via conversion to electricity, such as capturing CO_2 from ambient air or compressing produced syngas. Actively cooling the solar reactor between reduction and oxidation would also decrease the cycle time, therefore increasing the amount of fuel produced per time unit. However, the influence of rapid active cooling of ceria RPCs on their long-term mechanical stability is unknown and should be assessed.

Possibilities to decrease the content of unreacted CO_2 in the product gas mixture should be investigated. Besides changing operational parameters of the solar reactor to increase the conversion of reactant gases, this could be achieved for example by refeeding the product gas mixture, which is composed of CO_2, CO and H_2 after removal of excess water, into the reactor during oxidation. A high CO_2 utilization is not only important because CO_2 is a valuable feedstock, but also because a large amount of unreacted CO_2 in the accumulated product gas mixture could increase the necessary pumping and compression work or degrade the efficiency of the subsequent liquid fuels production process. The conversion of H_2O to H_2 should also be analyzed in more detail because of the significant amount of energy needed to evaporate the water. In addition, future solar reactors should be designed such that steam condensation is completely avoided inside the reactor, for example with better thermal separation of water-cooled parts or using a different cooling liquid at higher temperatures. Steam condensation limits the performance of the solar reactor because condensed water does not directly transform to H_2 and needs to be pumped out of the reactor in the subsequent reduction step, thereby limiting the minimum achievable pressure during reduction.

Possible ways to further increase the reactor efficiency also include operating at lower pressures during the reduction step or heating the solar reactor at atmospheric pressure and only applying vacuum at the end of the reduction step. By decreasing the pressure, more oxygen could be released and consequently more fuel could be produced per cycle. However, the energy needed to reach such low pressures should be assessed carefully to ensure that it remains at a reasonable proportion to the energy content of the produced fuel. By adapting the operating mode and applying vacuum towards the end of the reduction step while the ceria is heated at atmospheric pressure, the theoretical pumping work could be decreased because the released O_2 would be pumped at the highest possible pressure. Such an operating mode was proposed for example for a particle based reactor concept with multiple reduction chambers, and is expected to significantly decrease the required pumping work [137].

For the experiments presented in this work, the oxygen released by the ceria during the reduction step was vented together with argon that was used to protect the quartz window from the deposition of particles. In a future, commercial fuel production plant, the economic value of the technology could be increased by collecting the oxygen and selling it as a valuable feedstock for other processes. However, the separation of the mixture of oxygen and argon is costly and requires additional energy. Therefore, adaptions to the solar reactor design and operation should be assessed such that the reduction step can take place without the use of an inert gas. This could include a detailed computational assessment of the flow field inside the reactor and design changes to prevent any backflow from the main cavity of the reactor to the section of the window, or switching to O_2 as protective gas. With the latter approach, the fuel production capacity per cycle would decrease slightly because of the increased oxygen partial pressure during reduction, but the oxygen leaving the reactor could be used directly without the need for purification.

Apart from the solar reactor, the remaining subsystems of the solar fuels pilot plant presented in chapter 4 could also be improved. The inaccuracy of the power assessment technique could be decreased by correcting for the error introduced when measuring the power with the water calorimeter, which is located at a different position than the solar reactor. However, in order to do so, the systematic error would need to be assessed in detail, for example by means of an accurate ray tracing model of the heliostat field that also includes the water calorimeter, the solar reactor and the FMAS. By improving the aiming and tracking algorithm of the heliostats, the optical efficiency and maximum deliverable power of the heliostat field could be increased, while decreasing the thermal load on the solar reactor system by spilled radiation and increasing the available experimental time per day.

On the scale of complete fuel production plants, system-scale modelling should be applied to optimally integrate and couple the individual technologies, such as the concentrating facility, the solar thermochemical reactor and the liquid fuels synthesis unit. While some designs might be beneficial for the efficiency of individual subsystems, they do not necessarily maximize the performance of the

overall system. An example is a beam-down orientation solar concentrating field design where the concentrated sunlight is redirected with a secondary mirror on top of the tower to the solar reactor sitting on the ground. Such a design would decrease the optical efficiency of the concentrating facility, but might be beneficial for the long-term stability of the ceria structures because a self-supporting design hold in place by gravity could be implemented more easily when the solar reactor is facing upwards. Other trade-offs include the aperture size of the solar reactor and the conversion of H_2O and CO_2. A small reactor aperture increases the reactor's efficiency, but at the same time increases the complexity and cost of the solar concentrating facility and decreases its optical efficiency because of the need for higher concentration ratios. A future commercial solar fuels production plant is typically envisioned to consist of an array of solar reactors placed next to each other on the top of a solar tower. With such a configuration and the incorporation of compound parabolic concentrators (CPC) in front of the reactor's apertures, the optical losses of the solar concentrating facility could be lowered. The exact design, orientation, and the size of the individual solar reactors could be determined with a holistic model, keeping in mind the size limitation of the solar reactor due to manufacturing and stability limitations of the currently used ceria structures. The energy efficiency of the solar reactor is generally higher at lower conversions of H_2O and CO_2, but there is an energy penalty for heating and evaporating (in the case of H_2O) excess reactant gas as well as for CO_2 removal from the product gas mixture or to compress the unreacted CO_2 together with the syngas if it is not removed. A large amount of unreacted CO_2 in the produced syngas also decreases the efficiency of the downstream Fischer-Tropsch synthesis. Furthermore, it could be beneficial for the efficiency of the entire system to separately produce H_2 and CO in different cycles, or to dedicate some solar reactors to H_2 production only while others are dedicated to CO production. To answer such questions and to generally optimize the operation of the solar reactor for an ideal integration with other subsystems, the numerical model presented in chapter 3 could be extended to also include the oxidation step. However, a more simplified reactor model, for example a transient, one-dimensional model with the Rosseland diffusion approximation for radiation modelling, would be better suited to quickly assess

a large number of different parameters because of the drastically lower computational complexity.[1]

An in-depth techno-economic evaluation of the entire process chain from ambient air and water to liquid hydrocarbon fuels could also serve to assess in detail the expected production cost and to further evaluate the potential of the technology to eventually become economically competitive.

[1] A suitable model was developed within the framework of C. Larrea, “Assessment of a 50 kW solar reactor for thermochemical splitting of CO_2,” Master Thesis, ETH Zurich, 2018, supervised by S. Zoller.

List of figures

List of tables

References

[1] International Energy Agency, *World Energy Outlook 2018*. 2018.

[2] P. Forster *et al.*, "Changes in atmospheric constituents and in radiative forcing.," in *Climate Change 2007. The Physical Science Basis.*: Cambridge University Press, Cambridge, United Kingdom and New York, NY, USA., 2007.

[3] E. Dlugokencky, B. Hall, S. Montzka, G. Dutton, J. Mühle, and J. Elkins, "Atmospheric composition [in State of the Climate in 2017]," *Bulletin of the American Meteorological Society*, vol. 99, no. 8, pp. S46-49, 2018.

[4] V. Masson-Delmotte *et al.*, "IPCC, 2018: Summary for Policymakers," in *Global Warming of 1.5°C. An IPCC Special Report on the impacts of global warming of 1.5°C above pre-industrial levels and related global greenhouse gas emission pathways, in the context of strengthening the global response to the threat of climate change, sustainable development, and efforts to eradicate poverty*.

[5] H. Kuhn, C. Falter, and A. Sizmann, "Renewable energy perspectives for aviation," in *Proceedings of the 3rd CEAS Air & Space Conference and 21st AIDAA Congress*, Venice, Italy, 2011, pp. 1249-1259.

[6] R. W. Stratton, H. M. Wong, and J. I. Hileman, "Life cycle greenhouse gas emissions from alternative jet fuels," *Partner Project*, vol. 28, p. 133, 2010.

[7] J. Villoria, R. M. Navarro Yerga, S. Al-Zahrani, and J. L. G. Fierro, "Photocatalytic Hydrogen Production on $Cd_{1-x}Zn_xS$ Solid Solutions under Visible Light: Influence of Thermal Treatment," *Industrial & Engineering Chemistry Research*, vol. 49, no. 15, pp. 6854-6861, 2010.

[8] K. Hashimoto, H. Irie, and A. Fujishima, "TiO_2 photocatalysis: a historical overview and future prospects," *Japanese journal of applied physics*, vol. 44, no. 12R, p. 8269, 2005.

[9] J.-M. Lehn and R. Ziessel, "Photochemical generation of carbon monoxide and hydrogen by reduction of carbon dioxide and water under visible light irradiation," *Proceedings of the National Academy of Sciences*, vol. 79, no. 2, pp. 701-704, 1982.

[10] I. Abe, T. Fujimaki, Y. Kajiwara, and Y. Yokoo, "Hydrogen production by high temperature, high pressure water electrolysis. I-Plant development," in *Hydrogen Energy Progress*, 1981, pp. 29-41.

[11] A. Goldmann *et al.*, "A Study on Electrofuels in Aviation," *Energies*, vol. 11, no. 2, p. 392, 2018.

[12] A. Steinfeld and R. Palumbo, "Solar thermochemical process technology," *Encyclopedia of physical science and technology*, vol. 15, no. 1, pp. 237-56, 2001.

[13] A. Steinfeld, "Solar thermochemical production of hydrogen—a review," *Solar energy*, vol. 78, no. 5, pp. 603-615, 2005.

[14] D. Mignard and C. Pritchard, "Processes for the synthesis of liquid fuels from CO_2 and marine energy," *Chemical Engineering Research and Design*, vol. 84, no. 9, pp. 828-836, 2006.

[15] M. E. Dry, "The Fischer–Tropsch process: 1950–2000," *Catalysis today*, vol. 71, no. 3-4, pp. 227-241, 2002.

[16] C. Falter, V. Batteiger, and A. Sizmann, "Climate impact and economic feasibility of solar thermochemical jet fuel production," *Environmental science & technology*, vol. 50, no. 1, pp. 470-477, 2015.

[17] J. Wurzbacher, "Capturing CO_2 from air," in *Internationaler Motorenkongress 2017*: Springer, 2017, pp. 499-511.

[18] D. W. Keith, G. Holmes, D. S. Angelo, and K. Heidel, "A Process for Capturing CO_2 from the Atmosphere," *Joule*, vol. 2, no. 8, pp. 1573-1594, 2018.

[19] M. Wild, D. Folini, C. Schär, N. Loeb, E. G. Dutton, and G. König-Langlo, "The global energy balance from a surface perspective," *Climate dynamics*, vol. 40, no. 11-12, pp. 3107-3134, 2013.

[20] S. Baykara, "Experimental solar water thermolysis," *International Journal of Hydrogen Energy*, vol. 29, no. 14, pp. 1459-1469, 2004.

[21] Q. Jiang, Z. Chen, J. Tong, M. Yang, Z. Jiang, and C. Li, "Direct thermolysis of CO_2 into CO and O_2," *Chemical Communications*, vol. 53, no. 6, pp. 1188-1191, 2017.

[22] J. Lédé, F. Lapicque, and J. Villermaux, "Production of hydrogen by direct thermal decomposition of water," *International journal of hydrogen energy*, vol. 8, no. 9, pp. 675-679, 1983.

[23] A. Kogan, "Direct solar thermal splitting of water and on-site separation of the products—II. Experimental feasibility study," *International Journal of Hydrogen Energy*, vol. 23, no. 2, pp. 89-98, 1998.

[24] M. Romero and A. Steinfeld, "Concentrating solar thermal power and thermochemical fuels," *Energy & Environmental Science*, vol. 5, no. 11, pp. 9234-9245, 2012.

[25] T. Kodama and N. Gokon, "Thermochemical cycles for high-temperature solar hydrogen production," *Chemical reviews*, vol. 107, no. 10, pp. 4048-4077, 2007.

[26] S. Abanades, P. Charvin, G. Flamant, and P. Neveu, "Screening of water-splitting thermochemical cycles potentially attractive for hydrogen production by concentrated solar energy," *Energy*, vol. 31, no. 14, pp. 2805-2822, 2006.

[27] J. R. Scheffe and A. Steinfeld, "Oxygen exchange materials for solar thermochemical splitting of H_2O and CO_2: a review," *Materials Today*, vol. 17, no. 7, pp. 341-348, 2014.

[28] P. Charvin, S. Abanades, G. Flamant, and F. Lemort, "Two-step water splitting thermochemical cycle based on iron oxide redox pair for solar hydrogen production," *Energy*, vol. 32, no. 7, pp. 1124-1133, 2007.

[29] T. Kodama, Y. Nakamuro, and T. Mizuno, "A two-step thermochemical water splitting by iron-oxide on stabilized zirconia," *Journal of solar energy engineering*, vol. 128, no. 1, pp. 3-7, 2006.

[30] N. Gokon, H. Murayama, J. Umeda, T. Hatamachi, and T. Kodama, "Monoclinic zirconia-supported Fe_3O_4 for the two-step water-splitting thermochemical cycle at high thermal reduction temperatures of 1400–1600° C," *International Journal of Hydrogen Energy*, vol. 34, no. 3, pp. 1208-1217, 2009.

[31] T. Nakamura, "Hydrogen production from water utilizing solar heat at high temperatures," *Solar energy*, vol. 19, no. 5, pp. 467-475, 1977.

[32] J. R. Scheffe, A. H. McDaniel, M. D. Allendorf, and A. W. Weimer, "Kinetics and mechanism of solar-thermochemical H_2 production by

oxidation of a cobalt ferrite–zirconia composite," *Energy & Environmental Science*, vol. 6, no. 3, pp. 963-973, 2013.

[33] M. D. Allendorf, R. B. Diver, N. P. Siegel, and J. E. Miller, "Two-step water splitting using mixed-metal ferrites: thermodynamic analysis and characterization of synthesized materials," *Energy & Fuels*, vol. 22, no. 6, pp. 4115-4124, 2008.

[34] T. Kodama, Y. Kondoh, R. Yamamoto, H. Andou, and N. Satou, "Thermochemical hydrogen production by a redox system of ZrO_2-supported Co(II)-ferrite," *Solar Energy*, vol. 78, no. 5, pp. 623-631, 2005.

[35] A. Steinfeld, "Solar hydrogen production via a two-step water-splitting thermochemical cycle based on Zn/ZnO redox reactions," *International Journal of Hydrogen Energy*, vol. 27, no. 6, pp. 611-619, 2002.

[36] C. Perkins, P. R. Lichty, and A. W. Weimer, "Thermal ZnO dissociation in a rapid aerosol reactor as part of a solar hydrogen production cycle," *International Journal of Hydrogen Energy*, vol. 33, no. 2, pp. 499-510, 2008.

[37] P. G. Loutzenhiser, A. Meier, and A. Steinfeld, "Review of the two-step H_2O/CO_2-splitting solar thermochemical cycle based on Zn/ZnO redox reactions," *Materials*, vol. 3, no. 11, pp. 4922-4938, 2010.

[38] D. Weibel, Z. R. Jovanovic, E. Galvez, and A. Steinfeld, "Mechanism of Zn Particle Oxidation by H_2O and CO_2 in the Presence of ZnO," *Chemistry of Materials*, vol. 26, no. 22, pp. 6486-6495, 2014.

[39] E. E. Koepf, S. G. Advani, A. K. Prasad, and A. Steinfeld, "Experimental investigation of the carbothermal reduction of ZnO using a beam-down, gravity-fed solar reactor," *Industrial & Engineering Chemistry Research*, vol. 54, no. 33, pp. 8319-8332, 2015.

[40] M. Brkic, E. Koepf, and A. Meier, "Continuous solar carbothermal reduction of aerosolized ZnO particles under vacuum in a directly irradiated vertical-tube reactor," *Journal of Solar Energy Engineering*, vol. 138, no. 2, p. 021010, 2016.

[41] J. R. Scheffe, D. Weibel, and A. Steinfeld, "Lanthanum–strontium–manganese perovskites as redox materials for solar thermochemical splitting of H_2O and CO_2," *Energy & Fuels*, vol. 27, no. 8, pp. 4250-4257, 2013.

[42] A. H. McDaniel *et al.*, "Sr- and Mn-doped $LaAlO_{3-\delta}$ for solar thermochemical H_2 and CO production," *Energy & Environmental Science*, vol. 6, no. 8, pp. 2424-2428, 2013.

[43] C.-K. Yang, Y. Yamazaki, A. Aydin, and S. M. Haile, "Thermodynamic and kinetic assessments of strontium-doped lanthanum manganite perovskites for two-step thermochemical water splitting," *Journal of Materials Chemistry A*, vol. 2, no. 33, pp. 13612-13623, 2014.

[44] T. Cooper, J. R. Scheffe, M. E. Galvez, R. Jacot, G. Patzke, and A. Steinfeld, "Lanthanum manganite perovskites with Ca/Sr A-site and Al B-site doping as effective oxygen exchange materials for solar thermochemical fuel production," *Energy Technology*, vol. 3, no. 11, pp. 1130-1142, 2015.

[45] M. Takacs, M. Hoes, M. Caduff, T. Cooper, J. R. Scheffe, and A. Steinfeld, "Oxygen nonstoichiometry, defect equilibria, and thermodynamic characterization of $LaMnO_3$ perovskites with Ca/Sr A-site and Al B-site doping," *Acta Materialia*, vol. 103, pp. 700-710, 2016.

[46] M. Ezbiri, M. Takacs, B. Stolz, J. Lungthok, A. Steinfeld, and R. Michalsky, "Design principles of perovskites for solar-driven thermochemical splitting of CO_2," *Journal of Materials Chemistry A*, vol. 5, no. 29, pp. 15105-15115, 2017.

[47] W. C. Chueh and S. M. Haile, "Ceria as a Thermochemical Reaction Medium for Selectively Generating Syngas or Methane from H_2O and CO_2," *ChemSusChem: Chemistry & Sustainability Energy & Materials*, vol. 2, no. 8, pp. 735-739, 2009.

[48] W. C. Chueh and S. M. Haile, "A thermochemical study of ceria: exploiting an old material for new modes of energy conversion and CO_2 mitigation," *Philosophical Transactions of the Royal Society of London A: Mathematical, Physical and Engineering Sciences*, vol. 368, no. 1923, pp. 3269-3294, 2010.

[49] W. C. Chueh *et al.*, "High-Flux Solar-Driven Thermochemical Dissociation of CO_2 and H_2O Using Nonstoichiometric Ceria," *Science*, vol. 330, no. 6012, pp. 1797-1801, 2010.

[50] P. Furler, J. Scheffe, M. Gorbar, L. Moes, U. Vogt, and A. Steinfeld, "Solar thermochemical CO_2 splitting utilizing a reticulated porous ceria redox system," *Energy & Fuels*, vol. 26, no. 11, pp. 7051-7059, 2012.

[51] D. Marxer *et al.*, "Demonstration of the Entire Production Chain to Renewable Kerosene via Solar Thermochemical Splitting of H_2O and CO_2," *Energy & Fuels*, vol. 29, no. 5, pp. 3241-3250, 2015.

[52] M. Welte, R. Barhoumi, A. Zbinden, J. R. Scheffe, and A. Steinfeld, "Experimental demonstration of the thermochemical reduction of ceria in a solar aerosol reactor," *Industrial & engineering chemistry research*, vol. 55, no. 40, pp. 10618-10625, 2016.

[53] D. Marxer, P. Furler, M. Takacs, and A. Steinfeld, "Solar thermochemical splitting of CO_2 into separate streams of CO and O_2 with high selectivity, stability, conversion, and efficiency," *Energy & Environmental Science*, vol. 10, no. 5, pp. 1142-1149, 2017.

[54] S. Abanades, A. Legal, A. Cordier, G. Peraudeau, G. Flamant, and A. Julbe, "Investigation of reactive cerium-based oxides for H_2 production by thermochemical two-step water-splitting," *Journal of Materials Science*, vol. 45, no. 15, pp. 4163-4173, 2010.

[55] J. R. Scheffe, R. Jacot, G. R. Patzke, and A. Steinfeld, "Synthesis, characterization, and thermochemical redox performance of Hf4+, Zr4+, and Sc3+ doped ceria for splitting CO_2," *The Journal of Physical Chemistry C*, vol. 117, no. 46, pp. 24104-24114, 2013.

[56] M. Takacs, J. R. Scheffe, and A. Steinfeld, "Oxygen nonstoichiometry and thermodynamic characterization of Zr doped ceria in the 1573–1773 K temperature range," *Physical Chemistry Chemical Physics*, vol. 17, no. 12, pp. 7813-7822, 2015.

[57] M. Hoes, C. L. Muhich, R. Jacot, G. R. Patzke, and A. Steinfeld, "Thermodynamics of paired charge-compensating doped ceria with superior redox performance for solar thermochemical splitting of H_2O and CO_2," *Journal of Materials Chemistry A*, vol. 5, no. 36, pp. 19476-19484, 2017.

[58] R. Jacot, J. M. Naik, R. Moré, R. Michalsky, A. Steinfeld, and G. R. Patzke, "Reactive stability of promising scalable doped ceria materials for thermochemical two-step CO_2 dissociation," *Journal of Materials Chemistry A*, vol. 6, no. 14, pp. 5807-5816, 2018.

[59] M. Galvez, P. G. Loutzenhiser, I. Hischier, and A. Steinfeld, "CO_2 splitting via two-step solar thermochemical cycles with Zn/ZnO and FeO/Fe_3O_4 redox reactions: thermodynamic analysis," *Energy & Fuels*, vol. 22, no. 5, pp. 3544-3550, 2008.

[60] E. Koepf, W. Villasmil, and A. Meier, "Pilot-scale solar reactor operation and characterization for fuel production via the Zn/ZnO thermochemical cycle," *Applied Energy,* vol. 165, pp. 1004-1023, 2016.

[61] J.-P. Säck *et al.*, "High temperature hydrogen production: Design of a 750 KW demonstration plant for a two step thermochemical cycle," *Solar Energy,* vol. 135, pp. 232-241, 2016.

[62] M. Roeb *et al.*, "Test operation of a 100 kW pilot plant for solar hydrogen production from water on a solar tower," *Solar Energy,* vol. 85, no. 4, pp. 634-644, 2011.

[63] R. J. Panlener, R. N. Blumenthal, and J. E. Garnier, "A Thermodynamic Study of Nonstoichiometric Cerium Dioxide," *Journal of Physics and Chemistry of Solids,* vol. 36, no. 11, pp. 1213-1222, 1975.

[64] J. R. Scheffe and A. Steinfeld, "Thermodynamic analysis of cerium-based oxides for solar thermochemical fuel production," *Energy & Fuels,* vol. 26, no. 3, pp. 1928-1936, 2012.

[65] M. Mogensen, N. M. Sammes, and G. A. Tompsett, "Physical, chemical and electrochemical properties of pure and doped ceria," *Solid State Ionics,* vol. 129, no. 1-4, pp. 63-94, 2000.

[66] S. Ackermann, J. R. Scheffe, and A. Steinfeld, "Diffusion of oxygen in ceria at elevated temperatures and its application to H_2O/CO_2 splitting thermochemical redox cycles," *The Journal of Physical Chemistry C,* vol. 118, no. 10, pp. 5216-5225, 2014.

[67] S. Ackermann, L. Sauvin, R. Castiglioni, J. L. Rupp, J. R. Scheffe, and A. Steinfeld, "Kinetics of CO_2 reduction over nonstoichiometric ceria," *The Journal of Physical Chemistry C,* vol. 119, no. 29, pp. 16452-16461, 2015.

[68] N. Knoblauch, L. Dörrer, P. Fielitz, M. Schmücker, and G. Borchardt, "Surface controlled reduction kinetics of nominally undoped polycrystalline CeO_2," *Physical chemistry chemical physics,* vol. 17, no. 8, pp. 5849-5860, 2015.

[69] O. T. Sørensen, "Thermodynamic studies of the phase relationships of nonstoichiometric cerium oxides at higher temperatures," *Journal of Solid State Chemistry,* vol. 18, no. 3, pp. 217-233, 1976.

[70] G. B. Haxel, J. B. Hedrick, G. J. Orris, P. H. Stauffer, and J. W. Hendley, "Rare earth elements: critical resources for high technology," Fact Sheet 087-02, 2002.

[71] S. Abanades and G. Flamant, "Thermochemical hydrogen production from a two-step solar-driven water-splitting cycle based on cerium oxides," *Solar energy,* vol. 80, no. 12, pp. 1611-1623, 2006.

[72] C. W. Bale *et al.*, "FactSage Thermochemical Software and Databases, 2010-2016," vol. 54, ed: Calphad, 2016, pp. 35-53.

[73] F. Call *et al.*, "Thermogravimetric analysis of zirconia-doped ceria for thermochemical production of solar fuel," *American Journal of Analytical Chemistry,* vol. 4, no. 10, p. 37, 2013.

[74] A. Le Gal, S. p. Abanades, N. Bion, T. Le Mercier, and V. Harlé, "Reactivity of doped ceria-based mixed oxides for solar thermochemical hydrogen generation via two-step water-splitting cycles," *Energy & Fuels,* vol. 27, no. 10, pp. 6068-6078, 2013.

[75] P. Furler *et al.*, "Thermochemical CO_2 splitting via redox cycling of ceria reticulated foam structures with dual-scale porosities," *Physical Chemistry Chemical Physics,* vol. 16, no. 22, pp. 10503-10511, 2014.

[76] H. Kaneko *et al.*, "Rotary-type solar reactor for solar hydrogen production with two-step water splitting process," *Energy & Fuels,* vol. 21, no. 4, pp. 2287-2293, 2007.

[77] J. Lapp, J. H. Davidson, and W. Lipiński, "Heat transfer analysis of a solid-solid heat recuperation system for solar-driven nonstoichiometric redox cycles," *Journal of Solar Energy Engineering,* vol. 135, no. 3, p. 031004, 2013.

[78] S. Siegrist, H. von Storch, M. Roeb, and C. Sattler, "Moving Brick Receiver–Reactor: A Solar Thermochemical Reactor and Process Design With a Solid–Solid Heat Exchanger and On-Demand Production of Hydrogen and/or Carbon Monoxide," *Journal of Solar Energy Engineering,* vol. 141, no. 2, p. 021009, 2019.

[79] R. Bader *et al.*, "Design of a solar reactor to split CO_2 via isothermal redox cycling of ceria," *Journal of Solar Energy Engineering,* vol. 137, no. 3, p. 031007, 2015.

[80] I. Ermanoski, N. P. Siegel, and E. B. Stechel, "A new reactor concept for efficient solar-thermochemical fuel production," *Journal of Solar Energy Engineering,* vol. 135, no. 3, p. 031002, 2013.

[81] A. Singh *et al.*, "Design of a pilot scale directly irradiated, high temperature, and low pressure moving particle cavity chamber for metal oxide reduction," *Solar Energy*, vol. 157, pp. 365-376, 2017.

[82] J. Felinks, S. Brendelberger, M. Roeb, C. Sattler, and R. Pitz-Paal, "Heat recovery concept for thermochemical processes using a solid heat transfer medium," *Applied Thermal Engineering*, vol. 73, no. 1, pp. 1006-1013, 2014.

[83] B. J. Hathaway, R. Bala Chandran, A. C. Gladen, T. R. Chase, and J. H. Davidson, "Demonstration of a solar reactor for carbon dioxide splitting via the isothermal ceria redox cycle and practical implications," *Energy & Fuels*, vol. 30, no. 8, pp. 6654-6661, 2016.

[84] R. B. Diver, J. E. Miller, M. D. Allendorf, N. P. Siegel, and R. E. Hogan, "Solar thermochemical water-splitting ferrite-cycle heat engines," *Journal of Solar Energy Engineering*, vol. 130, no. 4, p. 041001, 2008.

[85] R. B. Diver, J. E. Miller, N. P. Siegel, and T. A. Moss, "Testing of a CR5 solar thermochemical heat engine prototype," in *ASME 2010 4th International Conference on Energy Sustainability*, 2010, pp. 97-104: American Society of Mechanical Engineers.

[86] J. E. Miller *et al.*, "Final Report—Reimagining Liquid Transportation Fuels: Sunshine to Petrol," *Sandia National Laboratories, Albuquerque, NM, Report No. SAND2012-0307*, 2012.

[87] P. Furler, J. R. Scheffe, and A. Steinfeld, "Syngas production by simultaneous splitting of H_2O and CO_2 via ceria redox reactions in a high-temperature solar reactor," *Energy Environ. Sci.*, vol. 5, no. 3, pp. 6098-6103, 2012.

[88] P. Furler and A. Steinfeld, "Heat transfer and fluid flow analysis of a 4kW solar thermochemical reactor for ceria redox cycling," *Chemical Engineering Science*, vol. 137, pp. 373-383, 2015.

[89] J. Lapp, J. H. Davidson, and W. Lipiński, "Efficiency of two-step solar thermochemical non-stoichiometric redox cycles with heat recovery," *Energy*, vol. 37, no. 1, pp. 591-600, 2012.

[90] B. Bulfin *et al.*, "Thermodynamics of CeO_2 thermochemical fuel production," *Energy & Fuels*, vol. 29, no. 2, pp. 1001-1009, 2015.

[91] S. Brendelberger, P. Holzemer-Zerhusen, H. von Storch, and C. Sattler, "Performance Assessment of a Heat Recovery System for Monolithic

Receiver-Reactors," *Journal of Solar Energy Engineering*, vol. 141, no. 2, p. 021008, 2019.

[92] C. P. Falter, A. Sizmann, and R. Pitz-Paal, "Modular reactor model for the solar thermochemical production of syngas incorporating counter-flow solid heat exchange," *Solar Energy*, vol. 122, pp. 1296-1308, 2015.

[93] C. P. Falter and R. Pitz-Paal, "A generic solar-thermochemical reactor model with internal heat diffusion for counter-flow solid heat exchange," *Solar Energy*, vol. 144, pp. 569-579, 2017.

[94] W. T. Gibbons, L. J. Venstrom, R. M. De Smith, J. H. Davidson, and G. S. Jackson, "Ceria-based electrospun fibers for renewable fuel production via two-step thermal redox cycles for carbon dioxide splitting," *Physical Chemistry Chemical Physics*, vol. 16, no. 27, pp. 14271-14280, 2014.

[95] M. Hoes, S. Ackermann, D. Theiler, P. Furler, and A. Steinfeld, "Additive-manufactured ordered porous structures made of ceria for concentrating solar applications," *Energy Technology*, 2019.

[96] M. Hoes, E. Koepf, P. Davenport, and A. Steinfeld, "Reticulated porous ceramic ceria structures with modified surface geometry for solar thermochemical splitting of water and carbon dioxide," in *AIP Conference Proceedings*, 2019, vol. 2126, no. 1, p. 180010: AIP Publishing.

[97] C. L. Muhich, S. Blaser, M. C. Hoes, and A. Steinfeld, "Comparing the solar-to-fuel energy conversion efficiency of ceria and perovskite based thermochemical redox cycles for splitting H_2O and CO_2," *international journal of hydrogen energy*, vol. 43, no. 41, pp. 18814-18831, 2018.

[98] J. Kim, T. A. Johnson, J. E. Miller, E. B. Stechel, and C. T. Maravelias, "Fuel production from CO_2 using solar-thermal energy: system level analysis," *Energy & Environmental Science*, vol. 5, no. 9, pp. 8417-8429, 2012.

[99] C. Falter and R. Pitz-Paal, "Water Footprint and Land Requirement of Solar Thermochemical Jet-Fuel Production," *Environmental science & technology*, vol. 51, no. 21, pp. 12938-12947, 2017.

[100] N. P. Siegel, J. E. Miller, I. Ermanoski, R. B. Diver, and E. B. Stechel, "Factors affecting the efficiency of solar driven metal oxide thermochemical cycles," *Industrial & Engineering Chemistry Research*, vol. 52, no. 9, pp. 3276-3286, 2013.

[101] K. Schwartzwalder and A. V. Somers, "Method of making porous ceramic articles," U.S. Patent 3090094, 1963.

[102] P. Roos, "Design, fabrication, and testing of large scale ceria RPC structures for a cavity-based 50 kW solar reactor," Master Thesis, ETH Zurich, 2016.

[103] P. Davenport, "Fabrication and characterization of large-scale ceria RPC structures for a 50 kW solar reactor cavity," Master Thesis, ETH Zurich, 2017.

[104] J. Petrasch *et al.*, "A novel 50 kW 11,000 suns high-flux solar simulator based on an array of xenon arc lamps," *Journal of Solar Energy Engineering,* vol. 129, no. 4, pp. 405-411, 2007.

[105] S. Brendelberger and C. Sattler, "Concept analysis of an indirect particle-based redox process for solar-driven H_2O/CO_2 splitting," *Solar Energy,* vol. 113, pp. 158-170, 2015.

[106] H. Häring, "The Air Gases Nitrogen, Oxygen and Argon," in *Industrial Gases Processing*: Wiley-VCH Verlag GmbH & Co. KGaA, 2008, pp. 9-109.

[107] S. Ackermann, M. Takacs, J. Scheffe, and A. Steinfeld, "Reticulated porous ceria undergoing thermochemical reduction with high-flux irradiation," *International Journal of Heat and Mass Transfer,* vol. 107, pp. 439-449, Apr 2017.

[108] D. Marxer, "4 kW solar reactor technology for splitting of H_2O and CO_2 with a temperature - pressure swing redox cycle," PhD Thesis, ETH Zurich, 2016.

[109] S. Ackermann and A. Steinfeld, "Spectral hemispherical reflectivity of nonstoichiometric cerium dioxide," *Solar Energy Materials and Solar Cells,* vol. 159, pp. 167-171, 2017.

[110] W. Villasmil, T. Cooper, E. Koepf, A. Meier, and A. Steinfeld, "Coupled Concentrating Optics, Heat Transfer, and Thermochemical Modeling of a 100-kW(th) High-Temperature Solar Reactor for the Thermal Dissociation of ZnO," *Journal of Solar Energy Engineering,* vol. 139, no. 2, 2017.

[111] J. Meija *et al.*, "Atomic weights of the elements 2013 (IUPAC Technical Report)," *Pure and Applied Chemistry,* vol. 88, no. 3, pp. 265-291, 2016.

[112] I. Riess, M. Ricken, and J. No, "On the specific heat of nonstoichiometric ceria," *Journal of Solid State Chemistry*, vol. 57, no. 3, pp. 314-322, 1985.

[113] Y. S. Touloukian, *Thermophysical properties of high temperature solid materials. Volume 4: Oxides and their solutions and mixtures. Part 1: Simple oxygen compounds and their mixtures*. New York: Macmillan, 1967.

[114] S. Ackermann, J. R. Scheffe, J. Duss, and A. Steinfeld, "Morphological Characterization and Effective Thermal Conductivity of Dual-Scale Reticulated Porous Structures," *Materials*, vol. 7, no. 11, pp. 7173-7195, 2014.

[115] Rath USA. (March 2, 2018). *Altra KVS High Temperature Vacuum Formed Boards and Shapes*. Available: http://www.rath-usa.com/datasheets/KVS-CERAMIC-FIBER-BOARDS-AND-SHAPES-FULL-LINE.pdf

[116] D. G. Archer, "Thermodynamic Properties of Synthetic Sapphire (α-Al2O3), Standard Reference Material 720 and the Effect of Temperature-Scale Differences on Thermodynamic Properties," *Journal of physical and chemical reference data*, vol. 22, no. 6, pp. 1441-1453, 1993.

[117] L. B. Pankratz and R. V. Mrazek, *Thermodynamic properties of elements and oxides*. Washington, D.C.: U.S. Bureau of Mines Bulletin, 1982.

[118] Y. S. Touloukian and D. P. DeWitt, *Thermal radiative properties: Nonmetallic solids*. Vol. 8. IFI/Plenum, New York, Washington, 1972.

[119] A. Steels. (March 2, 2018). *Grade Data Sheet 316 316L 316H*. Available: http://atlas.strategyonline.com/documents/Atlas_Grade_datasheet_316_rev_Jan_2011.pdf

[120] J. J. Valencia and P. N. Quested, "Thermophysical Properties," *ASM Handbook*, vol. 15, no. Casting, pp. 468-481, 2008.

[121] M. F. Modest, *Radiative Heat Transfer*, 3rd ed. Oxford: Academic Press, 2013.

[122] Flumroc AG. (February 27, 2018). *Flumroc-Brandschutzmatte FMI 500*. Available: https://www.flumroc.ch/produkte/technische-daemmung/detail/product/detail/flumroc-brandschutzmatte-fmi-500/

[123] D. F. Potter, S. Karl, M. Lambert, and K. Hannemann, "Computation of radiative and convective contributions to Viking afterbody heating," in *44th AIAA Thermophysics Conference*, 2013, p. 2895.

[124] W. Martienssen and H. Warlimont, *Springer handbook of condensed matter and materials data*. Berlin, Germany: Springer, 2006.

[125] K. C. Mills, *Recommended values of thermophysical properties for selected commercial alloys*. Woodhead Publishing, 2002.

[126] J. F. Shackelford and W. Alexander, *Thermal Properties of Materials*. Boca Raton, FL: CRC Press, 2001.

[127] J. Petrasch, "A free and open source Monte Carlo ray tracing program for concentrating solar energy research," in *ASME 2010 4th International Conference on Energy Sustainability*, 2010, pp. 125-132: American Society of Mechanical Engineers.

[128] R. Bader, L. J. Venstrom, J. H. Davidson, and W. Lipiński, "Thermodynamic analysis of isothermal redox cycling of ceria for solar fuel production," *Energy & Fuels*, vol. 27, no. 9, pp. 5533-5544, 2013.

[129] Y. Hao, C.-K. Yang, and S. M. Haile, "High-temperature isothermal chemical cycling for solar-driven fuel production," *Physical Chemistry Chemical Physics*, vol. 15, no. 40, pp. 17084-17092, 2013.

[130] O. Levenspiel, *Chemical reaction engineering*. NY: John Wiley and Sons, 1999.

[131] C. Muhich and A. Steinfeld, "Principles of doping ceria for the solar thermochemical redox splitting of H_2O and CO_2," *Journal of Materials Chemistry A*, vol. 5, no. 30, pp. 15578-15590, 2017.

[132] D. Nizamian, "Fabrication of ceria RPCs with improved mechanical stability," Semester Project, ETH Zurich, 2018.

[133] E. Koepf *et al.*, "Liquid fuels from concentrated sunlight: An overview on development and integration of a 50 kW solar thermochemical reactor and high concentration solar field for the SUN-to-LIQUID project," in *AIP Conference Proceedings*, 2019, vol. 2126, no. 1, p. 180012: AIP Publishing.

[134] M. Romero, J. González-Aguilar, and S. Luque, "Ultra-modular 500m^2 heliostat field for high flux/high temperature solar-driven processes," in

AIP Conference Proceedings, 2017, vol. 1850, no. 1, p. 030044: AIP Publishing.

[135] M. Thelen, C. Raeder, C. Willsch, and G. Dibowski, "A high-resolution optical measurement system for rapid acquisition of radiation flux density maps," in *AIP Conference Proceedings*, 2017, vol. 1850, no. 1, p. 150005: AIP Publishing.

[136] S. Ackermann, "Redox kinetics and transport phenomena of reticulated porous ceria," PhD Thesis, ETH Zurich, 2016, p. 123.

[137] I. Ermanoski, "Cascading pressure thermal reduction for efficient solar fuel production," *International Journal of Hydrogen Energy*, vol. 39, no. 25, pp. 13114-13117, 2014.

List of publications

Journal articles

S. Zoller, E. Koepf, P. Roos, and A. Steinfeld, “Heat transfer model of a 50 kW solar receiver-reactor for thermochemical redox cycling using cerium dioxide,” *Journal of Solar Energy Engineering*, 2019, 141 (2), 021014-021014-11.

Conference proceedings

E. Koepf, S. Zoller, S. Luque, S. Brendelberger, J. González-Aguilar, M. Romero, and A. Steinfeld, “Liquid fuels from concentrated sunlight: An overview on development and integration of a 50 kW solar thermochemical reactor and high concentration solar field for the SUN-to-LIQUID project,” *AIP Conference Proceedings*, 2019, vol. 2126, no. 1, p. 180012.

Conference presentations (oral)

S. Zoller, E. Koepf, D. Nizamian, A. Patané, A. Steinfeld, J. González-Aguilar, and M. Romero, “A 50 kW solar receiver-reactor for thermochemical splitting of H_2O and CO_2,” *ASME 13th International Conference on Energy Sustainability*, Bellevue, USA, July 14−17, 2019.

S. Zoller, E. Koepf, and A. Steinfeld, “50 kW scale solar thermochemical reactor for the synthesis of liquid hydrocarbon fuels,” *13th SOLLAB Doctoral Colloquium*, Berlin, Germany, May 15−17, 2017.